Department of Applied Physics

Radiative divertor studies in JET high confinement mode plasmas

Aaro Järvinen

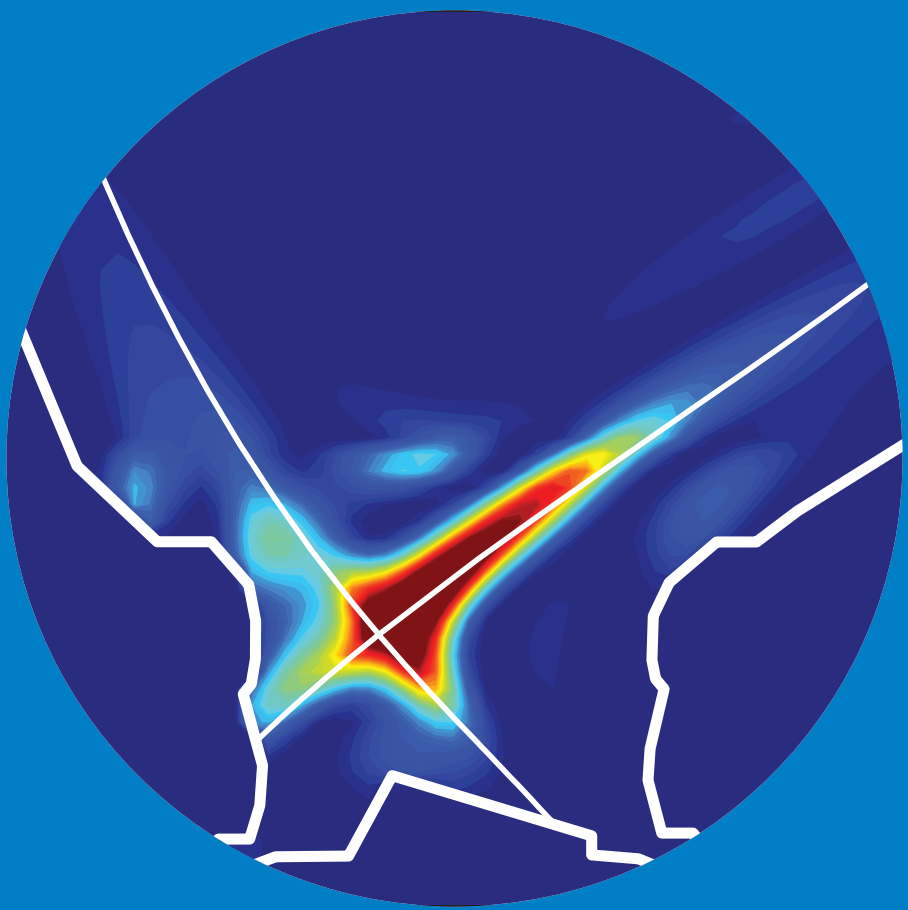

Aalto University

DOCTORAL DISSERTATIONS

Aalto University publication series
DOCTORAL DISSERTATIONS 156/2015

Radiative divertor studies in JET high confinement mode plasmas

Aaro Järvinen

A doctoral dissertation completed for the degree of Doctor of Science (Technology) to be defended, with the permission of the Aalto University School of Science, at a public examination held at the lecture hall F239a of the school on 4 December 2015 at 12.

Aalto University
School of Science
Department of Applied Physics
Fusion and Plasma Physics

Supervising professor
Mathias Groth, Aalto University, Finland

Thesis advisor
Mathias Groth, Aalto University, Finland

Preliminary examiners
Alberto Loarte, ITER Organization, France
Nobuyuki Asakura, Japan Atomic Energy Agency, Japan

Opponent
David Coster, IPP Garching, Germany

Aalto University publication series
DOCTORAL DISSERTATIONS 156/2015

ISBN 978-952-60-6475-8 (printed)
ISBN 978-952-60-6476-5 (pdf)
ISSN-L 1799-4934
ISSN 1799-4934 (printed)
ISSN 1799-4942 (pdf)
http://urn.fi/URN:ISBN:978-952-60-6476-5

Images: Aaro Järvinen

Unigrafia Oy
Helsinki 2015

Finland

Publication orders (printed book):
aaro.jarvinen@aalto.fi

441 697
Printed matter

Author
Aaro Järvinen

Name of the doctoral dissertation
Radiative divertor studies in JET high confinement mode plasmas

Publisher School of Science

Unit Department of Applied Physics

Series Aalto University publication series DOCTORAL DISSERTATIONS 156/2015

Field of research Fusion and Plasma Physics

Manuscript submitted 17 August 2015 **Date of the defence** 4 December 2015

Permission to publish granted (date) 14 October 2015 **Language** English

☐ **Monograph** ☒ **Article dissertation (summary + original articles)**

Abstract

Controlled power exhaust is one of the key challenges in reactor scale fusion devices. These devices must maintain heat loads less than 10 MW/m^2 at the plasma-facing materials (PFM), while producing gigawatts of fusion power. Furthermore, sufficiently low erosion of and fuel retention in PFMs are required to reach reactor relevant component duty cycles. The presently preferred solution to these challenges is to utilize tungsten PFMs with injection of extrinsic radiating impurities, such as nitrogen or neon. However, significant gaps do still exist in the technology and scientific understanding needed to fully rely that these devices will perform according to their design specifications. Predictive capability for these devices relies on model validation and physics interpretation studies conducted on existing fusion test reactors.

In this doctoral thesis, radiative divertor studies with nitrogen and neon injection are investigated experimentally and interpreted with the multi-fluid code package EDGE2D-EIRENE for high confinement mode plasmas in the JET tokamak. The studies include comparison of predicted and measured divertor conditions, investigations of the impact of PFMs and divertor geometry on the divertor performance, and comparison of divertor performance with nitrogen and neon injection. Furthermore, predictions for tungsten retention in the divertor chamber with the Monte-Carlo code DIVIMP were conducted.

When imposing the divertor radiation by impurities, the simulations capture the experimentally observed reduction of the low-field side (LFS) divertor peak heat load, radiated power, and their spatial distribution. However, consistent with earlier studies, the simulations underestimate the radiated power by deuterium, indicating a shortfall in the radiation from the fuel species. Due to similar radiative characteristics of nitrogen and carbon, the divertor radiation distributions observed in JET with carbon PFMs can be obtained with nitrogen seeding in JET with the ITER-like wall. Detachment is obtained at similar divertor radiation levels in both PFM configurations. Unexpectedly, divertor geometry is observed to have only a marginal impact on the reduction of the LFS heat load with increasing radiation. It is also observed that similar levels of LFS heat load reduction can be obtained at JET with either nitrogen or neon injection. However, unlike nitrogen radiation, a significant fraction of neon radiation is predicted to occur in the confined plasma, expected to reduce plasma performance. Furthermore, high density, low temperature divertor conditions are predicted to be beneficial for improving tungsten retention in the divertor of JET, and edge-localized modes (ELMs) are predicted to dominate tungsten erosion and leakage out of the divertor chamber in JET.

Keywords fusion, tokamak, impurities, power exhaust, divertor, radiation

ISBN (printed) 978-952-60-6475-8 **ISBN (pdf)** 978-952-60-6476-5

ISSN-L 1799-4934 **ISSN (printed)** 1799-4934 **ISSN (pdf)** 1799-4942

Location of publisher Helsinki **Location of printing** Helsinki **Year** 2015

Pages 248 **urn** http://urn.fi/URN:ISBN:978-952-60-6476-5

A! Aalto-yliopisto

Tiivistelmä

Aalto-yliopisto, PL 11000, 00076 Aalto www.aalto.fi

Tekijä
Aaro Järvinen

Väitöskirjan nimi
Radiative divertor studies in JET high confinement mode plasmas

Julkaisija Perustieteiden korkeakoulu

Yksikkö Teknillinen fysiikka

Sarja Aalto University publication series DOCTORAL DISSERTATIONS 156/2015

Tutkimusala Fuusio ja plasmafysiikka

Käsikirjoituksen pvm 17.08.2015 **Väitöspäivä** 04.12.2015

Julkaisuluvan myöntämispäivä 14.10.2015 **Kieli** Englanti

☐ **Monografia** ☒ **Yhdistelmäväitöskirja (yhteenveto-osa + erillisartikkelit)**

Tiivistelmä

Lämmönsiirto on eräs keskeisimmistä fuusioreaktoreiden haasteista. Seinämien kuormat eivät saa ylittää 10 MW/m^2 reaktoreiden tuottaessa useita gigawatteja fuusioenergiaa. Lisäksi seinämän eroosion sekä polttoaineen kertymisen reaktoriin täytyy olla riittävän hidasta, jotta toimintajakso huoltoseisokkien välissä on riittävän pitkä. Lupaavin ratkaisu näihin haasteisiin on käyttää volframia seinämämateriaalina ja suihkuttaa reaktoriin tehoa säteileviä epäpuhtauksia. Nykyisessä teknologisessa ja tieteellisessä ymmärryksessä on kuitenkin puutteita, eikä voida täysin luottaa siihen, että mallien avulla suunnitellut reaktorit suoriutuvat täysin tehtävistään. Ennusteet fuusioreaktoreille perustuvat laskentamallien validointiin ja fysiikan ilmiöiden tulkintaan olemassa olevilla fuusioreaktoreilla.

Tässä työssä tutkitaan sekä kokeellisesti että EDGE2D-EIRENE -koodipaketilla tehosäteilyä divertorilla JET-tokamakissa korkean koossapidon plasmoissa. Tutkimuksissa vertaillaan ennustettuja ja mitattuja diverttoriolosuhteita, tutkitaan seinämäkomponenttien materiaalien ja geometrian vaikutusta säteilevän diverttorin suorituskykyyn, sekä vertaillaan diverttorin suorituskykyä typpi- ja neonsuihkutuksella. Lisäksi volframin kulkeutumista on tutkittu ennustavilla Monte-Carlo simulaatioilla DIVIMP-koodia käyttäen.

Simulaatiot toistavat kokeellisesti havaitun diverttorisäteilyjakauman sekä teho- ja hiukkaskuorman vähenemisen matalan kentän puoleisella (LFS) diverttorilevyllä, mikäli kokeellisesti mitatut säteilytasot sovitetaan epäpuhtaussuihkutuksen avulla. Simulaatiot kuitenkin aliarvioivat deuteriumin aiheuttaman säteilyosuuden, kuten on havaittu aikaisemmissakin tutkimuksissa. Hiilen ja typen samankaltaisista säteilyominaisuuksista johtuen JET-tokamakin täyshiiliseinällä havaitut säteilyjakaumat voidaan toistaa typpisuihkutuksella JETin ITER-seinämä -kokeissa. Diverttoriplasman erkaantuminen saavutetaan samoilla säteilytasoilla molemmilla seinämämateriaaleilla. Vastoin odotuksia diverttorigeometrialla havaittiin olevan vain vähän vaikutusta LFS-diverttorilevyn lämpökuormituksen vähenemiseen säteilyn kasvaessa. Lisäksi samankaltaiset diverttorin lämpökuormituksen vähenemiset havaitaan sekä typpi- että neonsuihkutuksella. Toisin kuin typpisäteily, merkittävä osa neonsäteilystä kuitenkin tapahtuu koossapidetyn plasman puolella, minkä uskotaan heikentävän plasman suorituskykyä. Lisäksi korkean tehon ja matalan lämpötilan diverttoriolosuhteet on laskentamallien mukaan eduksi volframin pitämiseksi diverttorikammiossa. Reunamoodit (ELMs) dominoivat laskentamalleissa volframin eroosiota ja kulkeutumista ulos diverttorikammiosta JET-tokamakissa.

Avainsanat fuusio, tokamak, epäpuhtaudet, lämmönsiirto, diverttori, säteily

ISBN (painettu) 978-952-60-6475-8 **ISBN (pdf)** 978-952-60-6476-5

ISSN-L 1799-4934 **ISSN (painettu)** 1799-4934 **ISSN (pdf)** 1799-4942

Julkaisupaikka Helsinki **Painopaikka** Helsinki **Vuosi** 2015

Sivumäärä 248 **urn** http://urn.fi/URN:ISBN:978-952-60-6476-5

Preface

The research presented in this thesis has been carried out in the Fusion and Plasma Physics group at Aalto University, School of Science during 2011 – 2015. The work was begun under the supervision of Rainer Salomaa with Mathias Groth as the advisor. Around the time of beginning my doctoral studies in 2012, Mathias became the professor of the group and the supervisor of the work. I am grateful to both of them for allowing me to pursue a scientific career in the field of fusion energy research.

Regarding my growing up process as a scientists and, especially, as a scrape-off layer and divertor physicist, I am indebted to Mathias. Over these years, he has been a truly great instructor, mentor, and friend, who never let me get off the hook until the project was properly finished, as truly great supervisors always do. We used to call the late nights prior to project dead lines as 'pushing through the extra mile'. It was not always easy, but it was always worth it. Mathias, thank you for making me the scientist that I am today. I wish I can make you proud of being my first mentor in the scrape-off layer and divertor physics. I also wish that someday I can be as a great supervisor for young promising scientists as you have been to me.

I would like to thank all the great colleagues, senior scientists, and mentors that I have had pleasure to work with. Particular thanks goes to Geoff Maddison and Carine Giroud for the opportunity to work in the scientific team of the impurity seeded, high performance, high confinement mode plasmas in the JET tokamak. I thank Carine for letting me to work as her assistant scientific coordinator in the last series of experiments analyzed in this doctoral thesis. I would also like to show special gratitude to Sebastijan Brezinsek, Sven Wiesen, and Constanza Maggi, who always showed their interest into my research and gave me a lot of valuable guidance, mentoring, and comments on my research, both as task force

leaders at JET as well as colleagues, co-authors, and friends. I have also had pleasure to work with and to discuss about my projects with two of the distinctively established, great minds in fusion and divertor physics: Bruce Lipschultz and Guy Matthews. You two represent the paragon of fusion scientist to me. I wish I can someday reach the level of wisdom, physics understanding, and professionalism that you show on a daily basis. I am grateful to Gerard Corrigan, Derek Harting, and Paula Belo for always helping me with all the various issues and challenges that I faced with EDGE2D-EIRENE. I would also like to thank Marco Wischmeier and Felix Reimold for all the useful discussions we had on radiative divertor physics over the last couple of years. Finally, the conducted work would not have been possible with all the diagnostics experts: Marc Beurskens, Mathias Brix, Meike Clever, Stephane Devaux, Peter Drewelow, Thomas Eich, Christophe Guillemaut, Alexander Huber, Stefan Marsen, Andrew Meigs, Kerry Lawson, Bernhard Sieglin, and Mike Stamp. I would also like to thank all those contributors at Culham Centre for Fusion Energy and Max-Planck-Institut für Plasmaphysik who have not been mentioned in this preface.

Thanks to my parents, sister, and friends for all the support you gave me and for always believing in me, especially during the times when I did not. You truly helped me to push through the tough times with this thesis.

Espoo, October 19, 2015,

Aaro Järvinen

This work has been carried out within the framework of the EUROfusion Consortium and has received funding from the Euratom research and training programme 2014-2018 under grant agreement No 633053. The views and opinions expressed herein do not necessarily reflect those of the European Commission. The work was also partly funded by the Academy of Finland under the grant number 13253222.

Contents

List of Publications

This thesis consists of an overview and of the following publications which are referred to in the text by their Roman numerals.

I A.E. Jaervinen, S. Brezinsek, C. Giroud, M. Groth, C. Guillemaut, P. Belo, M. Brix, G. Corrigan, P. Drewelow, D. Harting, A. Huber, K. Lawson, B. Lipschultz, C.F. Maggi, G.F. Matthews, A.G. Meigs, D. Moulton, M.F. Stamp, S. Wiesen, and JET contributors. Impact of divertor geometry on radiative divertor performance in JET H-mode plasmas. *Plasma Physics and Controlled Fusion*, Submitted, August 2015.

II A.E. Jaervinen, C. Giroud, M. Groth, P. Belo, S. Brezinsek, M. Beurskens, G. Corrigan, S. Devaux, P. Drewelow, D. Harting, A. Huber, S. Jachmich, K. Lawson, B. Lipschultz, G. Maddison, C.F. Maggi, C. Marchetto, S. Marsen, G.F. Matthews, A.G. Meigs, D. Moulton, B. Sieglin, M.F. Stamp, S. Wiesen, and JET Contributors. Comparison of H-mode Plasmas in JET-ILW and JET-C with and without Nitrogen Seeding. *Nuclear Fusion*, Submitted, August 2015.

III A.E. Jaervinen, M. Groth, M. Airila, P. Belo, M. Beurskens, S. Brezinsek, M. Clever, G. Corrigan, S. Devaux, P. Drewelow, T. Eich, C. Giroud, D. Harting, A. Huber, S. Jachmich, K. Lawson, B. Lipschultz, G. Maddison, C.F. Maggi, T. Makkonen, C. Marchetto, S. Marsen, G.F. Matthews, A.G. Meigs, D. Moulton, M.F. Stamp, S. Wiesen, M. Wischmeier, and JET-EFDA collaborators. Interpretation of radiative divertor studies with impurity seeding in type-I ELMy H-mode plasmas in JET-ILW using EDGE2D-EIRENE. *Journal of Nuclear Materials*, **463**, 135 – 142,

2015.

IV A.E. Jaervinen, S. Brezinsek, C. Giroud, M. Groth, C. Guillemaut, P. Belo, M. Brix, G. Corrigan, P. Drewelow, D. Harting, A. Huber, K. Lawson, B. Lipschultz, C.F. Maggi, G.F. Matthews, A.G. Meigs, D. Moulton, M.F. Stamp, S. Wiesen, and JET contributors. Interpretation of partially detached divertor operation with and without impurity seeding in JET with EDGE2D-EIRENE. In *42nd EPS conference on Plasma Physics*, 22 – 26 June, 2015.

V A. Järvinen, M. Groth, D. Moulton, J.D. Strachan, S. Wiesen, P. Belo, M.N.A. Beurskens, G. Corrigan, T. Eich, C. Giroud, E. Havlickova, S. Jachmich, M. Lehnen, J. Lönnroth, D. Tskhakaya, and JET-EFDA contributors. Simulations of tungsten transport in the edge of JET ELMy H-mode plasmas. *Journal of Nuclear Materials*, **438**, S1005 – S1009, 2013.

VI A. Järvinen, C. Giroud, M. Groth, K. Krieger, D. Moulton, S. Wiesen, S. Brezinsek, and JET-EFDA contributors. DIVIMP simulations of W transport in the SOL of JET H-mode plasmas. *Physica Scripta*, **T145**, 014013, 2011.

Author's Contribution

Publication I: "Impact of divertor geometry on radiative divertor performance in JET H-mode plasmas"

The author participated in the design and completion of the experiments as a member of the scientific team as well as an assistant scientific coordinator in one of the experiments. Furthermore, the author conducted the EDGE2D-EIRENE simulations for the investigated discharges, post-processed the results, conducted the comparison to and interpretation of the experimental data, presented the results in a workshop, wrote the manuscript, and corresponded with the referees.

Publication II: "Comparison of H-mode Plasmas in JET-ILW and JET-C with and without Nitrogen Seeding"

The author carried out the EDGE2D-EIRENE simulations for the investigated discharges, post-processed the results, conducted the comparison to and interpretation of the experimental data, presented the results in a conference, wrote the manuscript, and corresponded with the referees.

Publication III: "Interpretation of radiative divertor studies with impurity seeding in type-I ELMy H-mode plasmas in JET-ILW using EDGE2D-EIRENE"

The author carried out the EDGE2D-EIRENE simulations for the investigated discharges, post-processed the results, conducted the comparison to and interpretation of the experimental data, presented the results in a conference, wrote the manuscript, and corresponded with the referees.

The work was presented as an invited talk in the 21st International Conference on Plasma Surface Interactions in Kanazawa, Japan, 26. – 30. May 2014.

Publication IV: "Interpretation of partially detached divertor operation with and without impurity seeding in JET with EDGE2D-EIRENE"

The author carried out the EDGE2D-EIRENE simulations for the investigated discharges, post-processed the results, conducted the comparison to and interpretation of the experimental data, presented the results at a conference, and wrote the conference proceeding. This conference proceeding paper is not peer reviewed. A fully peer reviewed journal paper on the work will be submitted after submission of this doctoral thesis.

Publication V: "Simulations of tungsten transport in the edge of JET ELMy H-mode plasmas"

The author carried out the EDGE2D-EIRENE and DIVIMP simulations for the investigated discharges, post-processed the results, conducted the comparison to experimental data, presented the results in a conference, wrote the manuscript, and corresponded with the referees.

Publication VI: "DIVIMP simulations of W transport in the SOL of JET H-mode plasmas"

The author carried out the DIVIMP simulations for the investigated discharges, post-processed the results, presented the results in a conference, wrote the manuscript, and corresponded with the referees.

1. Introduction

1.1 Nuclear fusion for energy production

The development of modern societies relies on an increasing production of energy. The global energy demand is foreseen to increase due to growing human population and improving quality of life on Earth, especially in rapidly developing countries, such as China and India [1]. While most of the global energy demand has been met by increasing usage of fossil fuels, such as coal and oil, their usage is being reconsidered due to their limited supply and accumulating evidence of the impact of greenhouse gas emissions on climate change [2]. Nuclear fission would provide a green-house gas free energy source for baseline energy production with adequate fuel resources. However, production of long-lived radioactive waste and proliferation of nuclear materials are a concern with fission based energy production. Thermonuclear fusion is the most promising alternative to fossil fuels for baseline electricity production without long-lived radioactive waste.

Nuclear fusion, the power source of stars, offers a virtually unlimited, green-house gas free energy source for mankind. The modern research on controlled nuclear fusion is focused around the fusion reaction between the heavy isotopes of hydrogen, deuterium (D, ^{2}H) and tritium (T, ^{3}H) given the reaction

$$\mathrm{D} + \mathrm{T} \rightarrow {}^4\mathrm{He}\ (3.5\ \mathrm{MeV}) + \mathrm{n}\ (14.1\ \mathrm{MeV}) \tag{1.1}$$

where 17.6 MeV of energy is released as the kinetic energy of the resulting alpha particle and the neutron. From the reaction products, the neutron escapes the fuel without interaction and can be used to heat external blankets to produce steam to drive turbines for electricity production. The electrically charged alpha particle is, on the other hand, confined in the

fusion fuel, and provides an intrinsic source of heat. Once the alpha particle has released its energy, it becomes *helium ash*, which dilutes the fuel, and must be exhausted to avoid unacceptable reduction of fusion power [3]. The DT fusion reaction provides the highest available fusion cross-section at feasible temperatures, peaking around 40 keV, with adequate availability of the reactants. Deuterium is abundantly available in sea water, and tritium can be bred from lithium with bombardment by neutrons produced by the DT fusion reaction. However, reaching sufficient breeding ratios for tritium self-sufficiency will be a challenge for any fusion reactor design based on the DT reaction.

For the fusion reaction to occur, the two positively charged nuclei must overcome their mutual electromagnetic repulsion for the attractive nuclear force to take over. To achieve this, the nuclei must approach each other with a high relative velocity, which can be obtained by heating the fuel to temperatures beyond 10 keV. Reactor relevant fusion rates are achieved at around 10 – 20 keV (100 – 200 million degrees of C). At these temperatures, the gas atoms are partially or fully ionized. Such a state of matter is called *plasma*.

Net energy production with fusion reactions requires sufficient confinement of the fusing plasma. The plasma can be confined by gravitational, magnetic, or inertial concepts. While stars are based on gravitational confinement, made possible by their large mass, the fusion reactor concepts on Earth are based on either inertial or magnetic confinement.

In the inertial confinement, the DT fuel is compressed to very high pressures, such that during the short time that the DT pellet disintegrates while fusing, the fusion power output exceeds the power needed for compressing and heating the fuel. In this concept, the plasma is confined by inertia only. The leading inertial confinement concept is based on usage of high power, carefully aligned laser beams [4].

The focus of this doctoral thesis is on *magnetic confinement fusion* (MCF). In MCF, the thermal energy of the fusion fuel is confined sufficiently long with carefully designed magnetic fields, such that the required heating power needed for control and sustainment of fusion reactor relevant temperatures is significantly lower than the fusion power generated by the reactor. If the intrinsic heating by the fusion reactions provides a considerable fraction of the total heating power in the plasma, the plasma is said to *burn*. If the plasma becomes thermally self-sustained, it is said to *ignite*.

Within a half a century of active research, the field of MCF has advanced to such a point that an experimental, burning-plasma device, the *International Thermonuclear Experimental Reactor* (ITER), is being built in Cadarache, France [5, 6]. The goal of ITER is to demonstrate the technological and scientific feasibility of controlled nuclear fusion for peaceful purposes. ITER will be the first experimental device providing access to reactor scale, burning fusion operation, where the plasma largely determines its own profiles. Overall the facility is foreseen to have a size, magnetic field strength, physics phenomenology, and technological basis sufficiently close to a thermonuclear power plant such that only little extrapolation is required to finalize the design of and construct a *demonstration power plant* (DEMO) [5 – 10]. The various national and international DEMO programs predict a similar timeframe, where fusion would begin to contribute to the global energy needs around the middle of this century [11]. Whether this is realistic or not is a matter of debate within the scientific community. ITER is based on the *tokamak* fusion reactor concept, which will be described in the next chapter [12]. This is also the reactor concept investigated in this doctoral thesis. Further information about the other fusion reactor concepts, which are not discussed here, can be found in [13].

1.2 Tokamak

1.2.1 Requirements for an MCF reactor

The requirement of very high fuel temperatures imposes great challenges for the MCF reactor design. The criterion of DT plasma to ignite yields the fusion *triple product* of plasma density, n, temperature, T, pressure, p, and energy confinement time, τ_E [12]:

$$nT\tau_E = p\tau_E > 5 \times 10^{21} \text{ m}^{-3}\text{keVs}. \tag{1.2}$$

In tokamak type reactors this is expected to be reached at values in the range of $n \sim 10^{20}$ m^{-3}, $T \sim 15$ keV, and $\tau_E \sim$ a few s. The highest achieved triple product so far is 1.5×10^{21} m^{-3}keVs in the JT-60U tokamak in Japan [14]. This is a factor of three smaller than required for ignition.

Generally speaking, any fusion reactor concept based on magnetic confinement of the plasma must fulfill, at least, the following four objectives. The two first are related to the plasma performance (Eq. 1.2), and the latter two are related to the fuel content control and exhaust of energy and helium ash from the system. Furthermore, additional technological requirements exist.

- **Energy confinement.** The energy must be confined long enough to maintain the required plasma temperatures with the fusion power exceeding the heating power. The energy confinement times, τ_E, of magnetic confinement fusion devices typically scale positively with the machine size and magnetic field strength, which is why progressively larger fusion devices have been built over the years in the development of the controlled nuclear fusion [5, 15].

- **Fuel pressure and density confinement** are directly related to the fusion power output and economical efficiency of a fusion reactor. The fusion power of a reactor scales roughly as Vp^2, where V is the fuel volume and p the thermal plasma pressure. The utilization efficiency of the magnetic volume is proportional to the confined pressure normalized by the magnetic field pressure

  $$\beta = \frac{p}{B^2/2\mu_0} \tag{1.3}$$

  where B is the strength of the magnetic field, and μ_0 the permeability of vacuum. Due to engineering and economical constraints limiting

the maximum machine size and magnetic field strength and, thus, the energy confinement time, the confined density and normalized pressure must exceed minimum values to maintain reactor relevant fusion power output. However, the maximum pressure and density in magnetic confinement devices are limited by plasma instabilities [16].

- **Fuel content control.** To maintain a quasi steady-state fusion power production, the fuel ions must be replaced at an equal rate to their consumption. At the same time, the reaction products must be exhausted from the system at an equal rate to their production. The impurity levels in the plasma must be kept sufficiently low to limit the reduction of the overall fusion power due to *fuel dilution* and the increase of the radiative power losses within an acceptable operational window. The fuel dilution level is typically described in terms of the *effective charge state* of the plasma

$$Z_{\text{eff}} = \frac{\sum_j n_j Z_j^2}{n_e} \tag{1.4}$$

  where the sum is over all the ion charge states, Z_j, and densities, n_j, in the plasma, and n_e is the electron density [12]. The particle content control in MCF devices is accomplished by gas and pellet injection, and pumping [6]. Part of the plasma fuelling is obtained also by *neutral beam injectors* (NBI), which are primarily used for heating the plasma. Reaching sufficiently high pumping and particle throughput rates is crucial for the operation to exhaust the reaction product, helium ash, from the system at a sufficiently high rate.

- **Power exhaust control.** To enable a quasi steady-state fusion power production, the reactor design must provide adequate control of power and particle exhaust to maintain the integrity of the *plasma-facing materials* (PFMs). Ensuring wall power loads within the engineering limits of the PFMs has become one of the most outstanding issues faced by the fusion community. This follows from the fact that in reactor scale fusion devices orders of magnitude larger exhausted power fluxes are predicted with only modestly larger exposed PFM areas when compared to existing devices [7, 17]. The power exhaust physics in conventional tokamaks is the main focus in this doctoral thesis.

Additional technological challenges are imposed by tritium self-sufficiency (in DT fusion) and degradation of materials properties in high neutron

flux environment, as is the case in economically interesting reactors actually producing fusion power [7, 12]. The tritium self-sufficiency is an issue since tritium is radioactive with a half-life of about 12.3 years and is, hence, not readily available in nature. It can be bred from lithium in-situ during the machine operation. Also neutron heating and shielding of the superconductive magnetic coils needs to be assessed in reactor design.

1.2.2 Operating principle

The overarching goal of a MCF scheme is to provide access to the desired fusion parameters (Eq. 1.2) in a quasi steady-state fashion without causing the wall components to melt or to be damaged excessively, such that the necessary PFMs can be replaced during a scheduled shut down. The leading fusion reactor concept is called *tokamak* (Fig. 1.1). A tokamak is a toroidal vacuum chamber, in which the plasma is confined by strong helical magnetic fields, B, generated by toroidal and poloidal field coils and currents flowing in the plasma. The toroidal field coils generate a toroidal magnetic field and a toroidal plasma current, I_p, generates the main poloidal magnetic field, which form together a helical field structure. In addition, poloidal field coils are used for shaping the plasma and controlling the position of the plasma in the vessel. Since the magnitude of the toroidal field decreases as a function of distance from the centre of the torus, $B_{\text{toroidal}} \sim \frac{1}{R}$, the inner side of the tokamak is called the *high field side* (HFS) and the outer side the *low field side* (LFS).

The helical magnetic field forms nested flux surfaces, which confine the plasma, such that the radially inward pointing magnetic force supports the outward pointing thermal plasma pressure gradient force

$$\mathbf{J} \times \mathbf{B} = \nabla p \tag{1.5}$$

where $\mathbf{J}$ represents the electrical current density. Tokamaks have demonstrated reactor relevant performance in terms of energy confinement and stability. The highest physics amplification factor, Q, which is the fraction of fusion power to the input power, achieved so far has been 0.64 in the *Joint European Torus* (JET) tokamak [18]. One of the principal aims of ITER, starting its operation in the 2020s, is to achieve amplification factor of 10, or higher [6].

Tokamak plasmas are heated with *ohmic resistivity*, *radiofrequency* (RF), and NBI heating. In addition to these, in burning plasma operation, a considerable fraction of the total heating power is provided by the fusion born

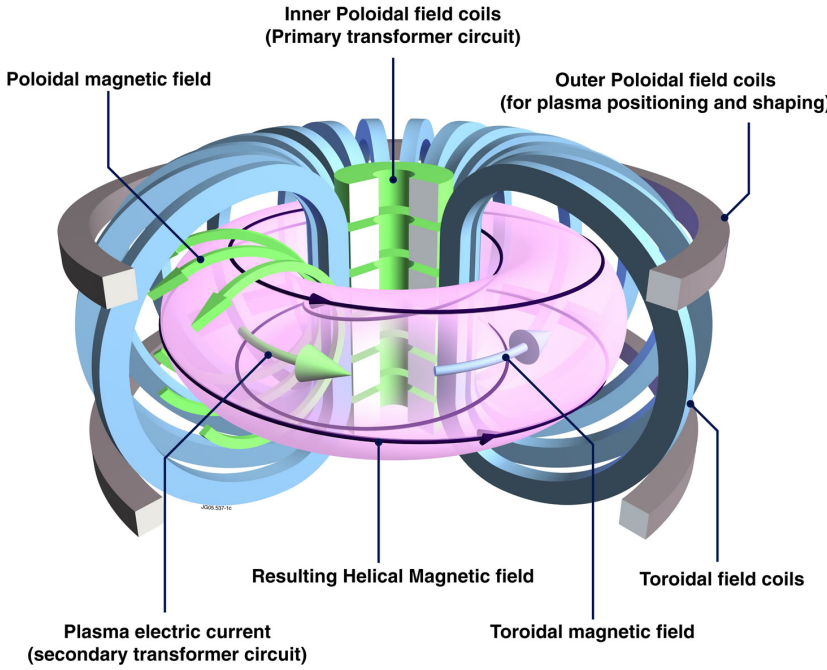

Figure 1.1. A schematic of a tokamak. The figure is courtesy of EUROfusion.

alpha particles. Ohmic heating is provided by the plasma current used to generate the poloidal magnetic field. In high performance plasmas in JET, which are the focus of this doctoral thesis, most of the heating is provided by the NBI and *ion cyclotron resonance RF-heating* (ICRH). Further details about the heating methods can be found in [12].

Plasma physics sets the lower limit to the size of an MCF fusion reactor. The main parameters determining the fusion performance are τ_E and β. The fuel density and β in tokamaks are limited by plasma instabilities [16, 19]. The most common empirical scaling for density limits in tokamaks is the *Greenwald density limit*

$$n_{\mathrm{GW}} = \frac{I_p}{\pi a^2} \tag{1.6}$$

where n_{GW} (10^{20} m^{-3}), I_p (MA), and a is the minor radius of the plasma (m) [20]. The foreseen plasma density and pressure values in ITER are about $n \sim 10^{20}\mathrm{m}^{-3}$ and $\beta_N \sim 1.5 - 3\%$ [6], where the β_N is the β normalized by the *Troyon* factor [19]

$$\beta_N(\%). = 100 \times \beta \times \left(\frac{I_p}{aB}\right)^{-1}. \tag{1.7}$$

τ_E in a tokamak is limited by transport losses of particles, momentum, and energy across the magnetic flux surfaces. This cross-field transport

greatly exceeds the level predicted by simple collisional transport estimates based on individual orbits of charged particles in the helical magnetic field in toroidal geometry [21]. This anomalously high cross-field transport is associated with nonlinear micro-turbulence of the plasma [21]. First principles models are not yet sufficiently mature to accurately predict this cross-field transport for reactor scale devices. Therefore, the confinement extrapolations to the next step devices, such as ITER, are based on scaling relations obtained on existing devices. Presently, the reference τ_E scaling for tokamak type fusion reactors is the IPB98(y,2)-scaling, given by [6]

$$\tau_E = 0.0562 I_p^{0.93} B^{0.15} P^{-0.69} n^{0.41} M^{0.19} R^{1.97} \epsilon^{0.58} \kappa^{0.78}, \tag{1.8}$$

where I_p represented the plasma current used to generate a part of the magnetic field, P the heating power, B the magnitude of the on-axis toroidal magnetic field of the torus, n the plasma density, M the average ion mass, R the major radius of the torus, ϵ the inverse aspect ratio of the torus, and κ the elongation. The measured confinement times are typically compared to reference confinement time scalings. The H_{98}-factor represents the measured confinement time relative to the IPB98(y,2)-scaling. In tokamaks, the confinement time is expected to scale roughly linearly proportional to I_p, and almost to the square of the linear size of the machine, R. Therefore, larger size machines and higher plasma currents are desired for high fusion performance. However, I_p is limited by *magneto-hydrodynamic* (MHD) instabilities, as well as current drive capabilities of the machine. On the other hand, the linear dimensions are limited by economical constraints, as well as performance constraints of the superconductive toroidal magnetic field coils.

The IPB98(y,2) confinement time scaling is based on the *high confinement mode* (H-mode) plasma regime with *edge localized MHD instability modes* (ELMs) [22, 23]. In H-mode, the energy confinement time of the plasma is typically about a factor of 2 higher than in conventional *low confinement mode* (L-mode) plasmas. H-mode operation is favored over L-mode operation in reactors, since the higher energy confinement allows more compact and economical reactor design. However, H-mode entails the extra complication of having to control ELMs to avoid excessive damage to the PFMs [24]. By combining the $\tau_{E,98(y,2)}$ confinement time scaling with DT reaction rates, plasma stability boundaries for n, β, and I_p, and neutron shielding requirements for the superconductive toroidal field coils, the spatial dimensions of a reactor scale tokamak can be estimated

as follows: major radius from the centre of the torus to the magnetic axis of the flux surfaces of about 7.8 m, horizontal minor radius from the magnetic axis of the flux surfaces to the outer wall of about 2.6 m [5]. The reference ITER values are 6.2 m and 2.0 m [6], and those of the JET tokamak are around 3 m and 1.2 m.

In the transition to H-mode confinement, the turbulence in the edge of the confined plasma is spontaneously suppressed when the power flux through the edge region exceeds a certain threshold value [22]. The suppression of the edge turbulence is associated with self-generated shear flows in the edge plasma, such that as the shearing rates exceed the turbulence growth rates, the radial turbulent fluxes are suppressed, and an *edge transport barrier* (ETB) region is formed. A region of strong density, temperature and plasma pressure gradients, the so-called *pedestal*, is formed in the edge of the confined plasma as a result of the formation of the ETB. Similarly to cross-field transport, presently, no first principles models exist to predict the conditions for the *L- to H-transition* (LH-transition) value and in particular of the heating power level required to access the H-mode. Accordingly, extrapolation to the next step devices are also obtained by regression analysis based scaling relations obtained on existing devices [21, 25]. In JET, the LH-transition is obtained typically with powers of 2 – 5 MW crossing the separatrix depending on the plasma operation parameters, while the value extrapolated for ITER is of about 46 – 160 MW [25]. The predicted LH-transition value for ITER is of similar magnitude to the total installed heating power capability of the device (73 MW [6]). As a result, entering H-mode confinement will be a challenge in ITER prior to DT operation or prior to the upgrade of the heating systems.

ELMs are a type of MHD plasma instabilities typical in the edge of H-mode plasmas [23]. The pressure and current gradients, which are formed in the edge plasma as a consequence of the pedestal formation, drive localized MHD instabilities, which relax the edge gradients and cause particles and energy to be expelled from the plasma. Many types of ELMs have been identified [23]. The most common are type-I and type-III ELMs. The type-I ELM regime is characterized by low frequency ($\sim$ 10 – 100 Hz) and high amplitude energy losses ($\sim$ 10 – 20 % of pedestal stored energy, W_{ped}) ELMs, associated with ideal peeling-ballooning MHD instabilities. The type-III ELM regime, on the other hand, is characterized by high frequency ($\sim$ 100 – 1000 Hz), and small amplitude energy losses ($\sim$ 1 – 4 % of

pedestal stored energy, W_{ped}) ELMs, which are associated with resistive MHD instabilities [23]. ELMs lead to strong intermittent particle and heat loads from the pedestal towards the wall components, and the ELMy behaviour of the H-mode plasmas pose a serious concern for the integrity of the wall components in the next step devices [6]. An unmitigated type-I ELM in ITER Q = 10 scenario is predicted to lead to parallel energy flux densities at the HFS divertor of the order of 17 MJ/m^2, which exceeds the surface melting threshold of tungsten PFMs (0.7 – 1.0 MJ/m^2) by a factor of more than 20 [26]. Hence, ELM mitigation mechanisms are an active subject of research within the tokamak community [23].

1.2.3 Plasma-surface interaction

The spatial dimensions and fusion power levels of an MCF device are determined by the need to satisfy the core plasma performance criterion (Eq. 1.2). Assuming that the desired performance can be reached with a device within these constraints, the remaining challenge is to prevent unacceptable PFM heat load leading to damage and melting of the wall components, and subsequent contamination and degradation of the plasma. Furthermore, one has to provide sufficient exhaust of helium ash to avoid dilution of the plasma to such a point that the performance criterion (Eq. 1.2) cannot be maintained [3]. Therefore, the plasma region between the burning core plasma, and the PFMs has to be able to meet the following requirements simultaneously [5, 6]:

- Exhaust the power fluxes flowing through the scrape-off layer (SOL) (Fig. 1.2) with loads less than 10 MW/m^2 at the wall components.

- Exhaust helium ash by sufficient pumping to limit the central plasma helium concentrations below 6 %.

- Control the plasma density and fusion power by sufficient pumping.

- Fuel the **divertor** plasma by recycling the wall recombined neutral particles back into the plasma.

- Ensure sufficiently low impurity levels in the main plasma, by screening and reduction of wall erosion, to avoid degradation of the plasma performance.

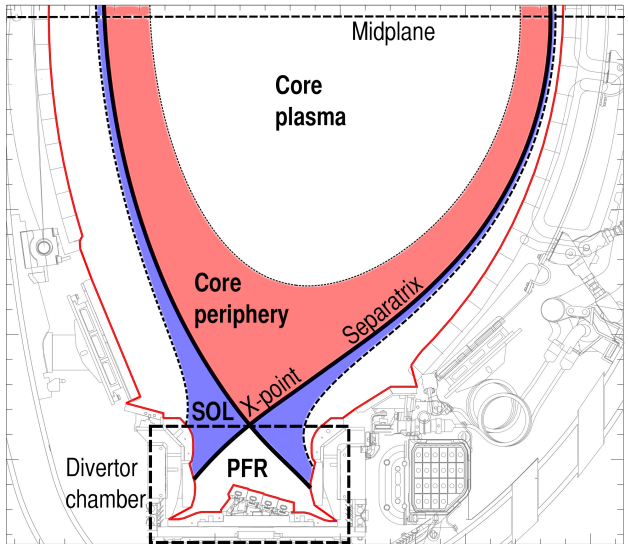

Figure 1.2. The 2011 divertor in the Joint European Torus in a vertical divertor plasma target configuration

Limiter and divertor configurations

The two standard arrangements for the *plasma-surface interaction* (PSI) in tokamaks are *limiter* and *divertor* configurations. In a limiter configuration, a solid material limiter intersects the nested magnetic flux surfaces, such that the tip of the limiter defines the *last closed flux surface* (LCFS). The region of the open magnetic flux surfaces connected to the wall components, along which the plasma scrapes-off radially due to the parallel sink action of the solid surfaces, is called the *scrape-off layer* (SOL). In a divertor configuration, the SOL plasma is diverted into a separate divertor chamber using additional divertor field coils. The principal PSI occurs at the specially designed divertor plates (Fig. 1.2). The separatrix is the field line separating the SOL from the *core periphery*, which is the outer region of the closed flux surfaces. The points or lines where the separatrix intersects the target surfaces are called the *strike points* or *lines*. The term *LFS mid-plane* (LFS-MP) refers to the mid-plane of the cross-section of the toroidal cylinder at larger major radius values than the magnetic axis. The LFS-MP region is often also called the *upstream* SOL plasma, whereas the divertor plasma is called the *downstream* SOL plasma. The *private flux region* (PFR) is the plasma below the *X-point* isolated by the separatrix. The divertor configuration with a single active magnetic X-point at the bottom of the cross-sections is called a *lower single null* configuration (Fig. 1.2). The plasma *triangularity* describes

the horizontal displacement of the highest (upper triangularity) or lowest (lower triangularity) point of the LCFS from the magnetic axis [12]. Positive triangularity stands for the magnetic axis being located at larger radial position than the highest or lowest point of the LCFS.

The limiter configuration provides a good utilization efficiency of the magnetic volume inside the toroidal field coils. However, since the confined plasma within the closed flux surfaces is in a direct contact with the solid material limiter, controlling screening and wall erosion is a significant challenge in this configuration. Furthermore, limiter configurations have difficulties providing sufficiently high neutral pressures in front of the pumps to allow sufficiently high pumping for helium ash and density control. However, *pumped limiter* concepts have been developed to alleviate this issue [27, 28]. For power flux control, a carefully optimized wall limiter could possibly reach sufficiently high *plasma wetted area*, which is the area of the wall in contact with the plasma, so that the wall power fluxes would be tolerable. However, this would require a high level of plasma position control and careful avoidance of leading edges at the PFMs, and is very challenging to realize technologically in a reactor scale device.

The divertor configuration is designed to provide adequate particle and power control in a tokamak. Although the divertor does occupie some of the valuable plasma volume, and, therefore, reduces the utilization efficiency of the magnetic volume, it also offers many operational advantages. Divertors were originally proposed to alleviate the impurity contamination problem in MCF devices by separatring the main source of impurities, PSI, from the confined plasma region [29]. Compressing the recycled neutrals into the divertor chamber facilitates pumping and enhances the control of fuel, impurity, and helium exhaust. In principle, focusing the exhausted plasma into a small divertor chamber increases the heat flux densities towards the PFMs relative to more uniform plasma contact to PFMs, which makes the power exhaust problem of a diverted tokamak more challenging. However, increasing the plasma volume between the confined region and the PFMs, as is the case in the divertor configuration, facilitates the volumetric power losses by radiation, charge exchange, and recombination, which are foreseen to compensate the drawback caused by the reduced wall area. Furthermore, injection of external impurities, such as nitrogen or neon, can be used to increase the radiative power losses in the confined and divertor plasma, therefore reducing peak heat fluxes in

the divertor. This is called the *radiative divertor* concept, and the injection of extrinsic impurites *impurity seeding*. Moreover, atomic processes and plasma transport in the divertor chamber provide plasma cooling in front of the divertor target plates. This reduces erosion of wall materials, may enhance divertor retention of impurities, and provides access to divertor *detachment*, where neutral friction and volume recombination of the plasma can become significant and the wall power fluxes are strongly reduced, due to the reduced plasma contact with the wall [30].

Plasma sheath

In front of a solid surface in contact with plasma, a thin region of net positive volume charge is formed. This is called the *sheath*. Due to the large inertia difference between electrons and ions, negative electric field forms in front of the solid surface to push away electrons and pull ions towards the surface to maintain ambipolar plasma flow to the plate [31]. The typical sheath thickness is about 5 *Debye lengths*, which is the characteristic scale length for spontaneous thermal charge separation in a plasma $\lambda_\mathrm{D} \sim \sqrt{\frac{\epsilon_0 T_e}{n_e e^2}}$, where ϵ_0 is the vacuum permittivity, and e the unit charge [12]. For typical tokamak divertor conditions ($T_e \sim 0.5$ – 40 eV, $n_e \sim 0.5 \times 10^{20} - 10 \times 10^{20}$ m^{-3}) $\lambda_\mathrm{D} \ll 1$ mm $\ll L_\mathrm{connection}$, where $L_\mathrm{connection}$ is one half of the length from the LFS divertor target to the HFS divertor target along the magnetic field line. The plasma potential drop within the sheath depends on, at least, the dominant plasma species, the electron temperature, and temperature difference between the main ions and electrons [31]. Assuming hydrogenic plasma ions with small temperature difference between the main ions and electrons, $V_\mathrm{sheath} \sim -3T_e/e$ is expected to give a good representation of the sheath potential drop and this value is used in this study [31]. A further consequence of the sheath is that the plasma flow accelerates to sonic or super-sonic velocities at the plasma-sheath interface [31 – 33]. This is called the *Bohm criterion*.

Plasma-facing materials (PFM)

Plasma-facing materials in burning DT plasma devices must meet several criteria simultaneously. These include resistance to damage by large steady-state heat loads, resilience to transient heating and MHD events, sufficiently long component lifetime against erosion by the plasma, and minimization of tritium retention in the vessel [6]. Tritium retention is a safety issue due to an administrative limit on the inventory of in-vessel radioactive material. Once these limits are reached, an active cleaning in-

tervention is required prior to further machine operation. Reaching this limit too frequently reduces the duty cycle of a power plant below economically attractive values.

Various PFM have been considered within the history of MCF devices [34]. The main materials considered in modern tokamaks are carbon, beryllium, tungsten, and molybdenum. For the past decades, carbon based materials have been the favored PFM solution in MCF devices [34]. This followed from the operational success of NBI heated discharges at *Princeton Large Torus* (PLT) tokamak reaching high performance after changing tungsten limiters to graphite [35]. Tungsten, as a high atomic number species, retains some of its orbital electrons even in the high temperatures of the central plasma, and, therefore, radiates intense line-radiation in the confined plasma. Carbon, on the other hand, becomes fully stripped in the confined plasma temperatures, and the associated impurity induced, radiative losses are reduced to the Bremsstrahlung level. On the other hand, carbon surfaces undergo sublimation instead of melting, when overheated [34]. Therefore, carbon is a very versatile PFM in tokamaks, avoiding surface irregularities in high PFM heat flux conditions as well as in off-normal events, such as strong ELMs or disruptions. Due to these reasons, carbon PFM based tokamaks have reached the world records in terms of fusion triple product (1.5×10^{21} m^{-3}keVs) at JT-60U [14], as well as total generated fusion power (16.1 MW) at JET [18]. The main drawbacks of carbon as PFM in reactor scale devices are strong retention of tritium in co-deposited layers with carbon, and high erosion rates even in cool plasma conditions due to chemical erosion [34, and references therein]. Due to these reasons, the focus of MCF research on PFMs has returned to metals as the solution for reactor scale devices. Nowadays, metallic PFMs are used in many fusion-relevant tokamak experiments worldwide. JET utilizes ITER-like combination of beryllium main chamber and tungsten divertor PFMs (Fig. 1.3) [5, 36] , the ASDEX-Upgrade (AUG) tokamak features full tungsten PFM coverage [37] , and the Alcator C-Mod tokamak uses molybdenum PFMs [38].

The currently leading candidate material for divertor PFMs is tungsten due to its low retention of fuel species and resistance against erosion in partially detached plasma conditions [39]. Tungsten erosion due to plasma and trace impurities can be very strongly suppressed if plasma electron temperatures below 5 – 10 eV are obtained in front of the PFM surfaces [40]. However, even in such low temperature conditions, in H-

mode plasmas, tungsten erosion still occurs during ELMs [40, 41]. In future reactors, the main chamber PFMs are likely to be made of tungsten to reach sufficiently long component lifetime [42]. The ITER main chamber material is beryllium to optimize the plasma performance by minimizing the radiation losses in the main plasma [5]. However, the lifetime of beryllium is too short, due to high physical sputtering yield and low melting temperature, to allow acceptable component duty cycle for practical power plant usage [34, 42].

Impurity radiation is a major issue with tungsten. As tungsten is a high atomic number element, the ionization potentials for the electrons at low level orbits are fairly high and, hence, tungsten retains some of its orbital electrons even in the plasma temperatures relevant for fusion reactors. Therefore, tungsten contamination leads to strong line radiation, which can be detrimental for the plasma performance. In fact, tungsten concentrations of a few 10^{-5} tungsten particles per plasma electron can prevent reactor relevant achievement of the performance criterion (Eq. 1.2) [43]. Accordingly, controlling tungsten sources and transport is one of the critical problem areas in fusion reactors in which tungsten PFMs are used. To address the plasma operation with tungsten divertor and beryllium main chamber PFMs, the *ITER-like wall* (ILW) was installed into the JET tokamak in 2011, with bulk tungsten outer target plate, tungsten coated *carbon fibre composite* (CFC) at the divertor baffles and beryllium limiters in the main chamber [36] (Fig. 1.3).

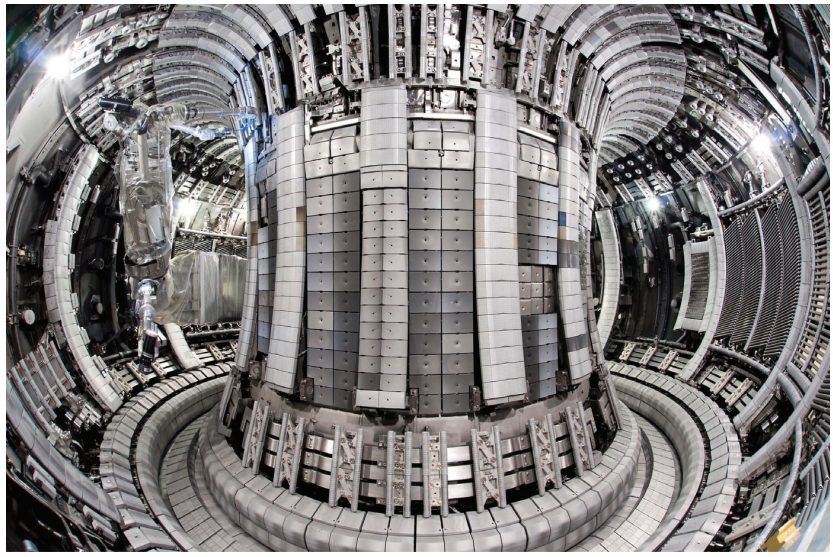

Figure 1.3. JET after the installation of ILW. The remote handling manipulator is conducting final adjustments. [36]

1.3 Scope of the thesis

This thesis focuses on numerical and experimental studies of divertor performance in JET H-mode plasmas with and without extrinsic impurity seeding. Interpretations of radiative divertor studies with impurity seeding using the EDGE2D-EIRENE multi-fluid code package will be presented, including validation of the simulations tool by comparison to experimental data, and identification of discrepancies between the experiment and the model [44 – 46]. The simulations encompass detailed comparison of predicted and measured divertor conditions and 2D power- and line-radiation distributions, investigations of the impact of wall material (full carbon and ITER-like wall) on the radiative divertor performance, investigations of the impact of divertor geometry on the radiative divertor performance, and comparison of radiative divertor performance with nitrogen and neon radiation. Furthermore, predictions for tungsten retention in the divertor chamber with Monte-Carlo code DIVIMP were conducted based on earlier EDGE2D-EIRENE calculations for H-mode plasmas in JET with the previous carbon wall [47].

The thesis is organized as follows. Chapter 2 presentes an overview of power exhaust physics in tokamaks. In chapter 3, tungsten concentration control in tokamaks is discussed. The main results of the Publications I – IV on radiative divertor studies are summarized in chapter 4, and the main results of the Publications V – VI on divertor retention of tungsten are given in chapter 5. Finally, chapter 6 concludes the work and presents an outlook for suitable avenues for further research.

2. Power exhaust in tokamaks

2.1 Power exhaust challenge

The divertor targets in reactor relevant operation must endure surface heat fluxes in the range of 5 – 10 MW/m^2, while operating at core plasma conditions satisfying the required performance criteria (Eq. 1.2) [6]. The severity of the heat load issue is often discussed in terms of P_{HEAT}/R or P_{SEP}/R-ratio of the device in question, where P_{HEAT} is the total heating power to the plasma, P_{SEP} is the power crossing the separatrix, and R is the major radius of the device [48 – 50]. This is based on the experimental finding that the SOL power e-folding length, λ_q, does not depend on the machine size [51], and that the parallel power flux in the SOL is approximately given by [30]

$$q_{\parallel,\mathrm{SOL}} \approx \frac{P_{\mathrm{SEP}} A q_{95}}{4\pi R \lambda_q} \propto \frac{P_{\mathrm{SEP}}}{R} \tag{2.1}$$

where A represents the tokamak aspect-ratio (major radius divided with minor radius), and q_{95} stands for the edge plasma safety factor, of a typical value of 3 – 6. A single poloidal divertor is assumed. The safety factor is the number of toroidal circuits that a magnetic field line completes during a full poloidal revolution, and represents the pitch angle of the magnetic field. A $\lambda_q \propto R$ -scaling has also being suggested in the literature [52, and references therein], and a full consensus about the λ_q-scaling does not yet exist. The $\lambda_q \propto R$ -scaling would consequently give P_{HEAT}/R^2-scaling for the target heat fluxes, which would be a more favorable scaling for reactor heat loads. Furthermore, attempts to extend the set of dimensionless plasma performance parameters (collisionality, $\nu*$, normalized gyro-radius, $\rho*$, and β) to divertor physics by inclusion of atomic physics effects require identity of the absolute reference plasmas temperature [50]. In the original approach of Lackner, this also lead to

P_{HEAT}/R-scaling for partial divertor physics similarity across devices (β not preserved) [50]. Later studies by Hutchinson et al., allowing geometrical flexibilities in the divertor plasmas, show that divertor similarity could be achieved at heating powers scaling sublinearly with R [53]. Nevertheless, the conventional P_{HEAT}/R-scaling is used as the figure of merit for the severity of the power exhaust problem in this study.

Table 2.1. Estimated P_{HEAT}/R-values, LFS mid-plane SOL power fluxes, $q_{\parallel,\,\mathrm{LFS\text{-}MP}}$, projected unmitigated surface heat fluxes, and surface heat fluxes assuming power fall-off length along the target, $\lambda_{\mathrm{int}} = 2.6$ mm, in AUG, JET, ITER, and DEMO as given in [54]. A power fall-off length λ_q of 1 mm at the LFS-mid plane is assumed.

	AUG	**JET**	**ITER**	**DEMO**
Major radius (m)	1.7	3.0	6.2	> 7
Heating power (MW)	23	∼38	∼100	∼600
P_{HEAT}/R	14	7 – 12	20	80 – 100
$q_{\parallel,\mathrm{LFS\text{-}MP}}$ (GW/m^2)	3.5	2	5	>30
Unmitigated $q_\perp$ (MW/m^2)	35	20	50	300
$q_\perp$ assuming $\lambda_{\mathrm{int}} = 2.6$ mm (MW/m^2)	13	8	20	115

A factor of 200 heat flux reduction between the main SOL and the divertor target is predicted necessary in JET, assuming maximum available heating power, to reach the level of 10 MW/m^2 (Table 2.1). In ITER, the factor is around 500, and in a fusion reactor type device about 3000. The two largest existing tokamaks, JET and JT-60U, have $P_{\mathrm{HEAT}}/R \sim 7 - 12$, ITER will have $P_{\mathrm{HEAT}}/R \sim$ about 20, and a DEMO sized tokamak will have P_{HEAT}/R about 80 – 100 [49] (Table 2.1). Assuming a λ_q of about 1 mm [51, 55], it was shown that the upstream power fluxes parallel to the magnetic field in JET can reach about 2 GW/m^2, in ITER about 5 GW/m^2 and in a DEMO sized reactor more than 30 GW/m^2. Including the impact of geometrical factors, ξ, such as flux expansion and field-line angle to the divertor plate, of which the latter is limited to values higher than 1 degree, and radiation fraction in the SOL, $f_{\mathrm{rad,\,SOL}}$, the target power flux, $q_\perp$, surface, is given approximately by

$$q_{\perp,\mathrm{surface}} \approx \xi(1 - f_{\mathrm{rad,SOL}})q_{\parallel,\mathrm{SOL}} \tag{2.2}$$

In conventional divertors, the heat flux projected on the divertor surface can be about a factor of 100 lower than the parallel heat flux on the surface (Table 2.1). When adding the expected power spreading in the divertor, this reduction becomes largely sufficient for existing devices [51, 54, 56,

57]. In ITER, however, a further factor of 2 – 5 reduction is needed, and a factor of 10 – 30 is required in reactors. This additional reduction must come from the radiative power exhaust. Accordingly, the goal radiative fraction for ITER is about 70 – 80%, while the values predicted necessary in reactors approach 100%.

2.2 Radiative power exhaust

The future fusion reactors are foreseen to operate with metallic plasma-facing materials to ensure low erosion rates, and low tritium retention. The conventional method to increase the radiative fraction of tokamak plasmas with metallic PFMs is to inject extrinsic radiating impurities into the plasma. This is called *impurity seeding*. Typical seeding gases are nitrogen, neon, argon, and krypton [58, 59]. Radiative power removal to reduce the divertor heat fluxes occurs in three stages (Fig. 2.1) [30, 58] :

- Radiative cooling inside the separatrix (core and mantle radiation).
- Radiative cooling in the SOL and divertor.
- Plasma power, pressure, and particle flux reduction in the divertor due to atomic and plasma transport processes relevant in low temperature ($T_e < 2$ eV), high density ($n_e \sim 10^{21}$ m^{-3}) hydrogenic plasmas, also known as *detachment*.

In the first stage, radiation in the main plasma, inside the separatrix, by bremsstrahlung and line-radiation in the core and core periphery (Fig. 2.1), is used to reduce the loss power, P_{LOSS}, or the power crossing the separatrix, P_{SOL}:

$$P_{\mathrm{LOSS}} = P_{\mathrm{HEAT}} - P_{\mathrm{RAD,\,CORE}} \tag{2.3}$$

$$P_{\mathrm{SOL}} = P_{\mathrm{HEAT}} - P_{\mathrm{RAD,\,CORE}} - \frac{dW}{dt} \tag{2.4}$$

where P_{HEAT} is the total heating power in the experiment, $P_{\mathrm{RAD,CORE}}$ the total radiated power inside the separatrix, and dW/dt the rate of change of the plasma stored energy. These definitions of P_{LOSS} and P_{SOL} are used throughout this doctoral thesis.

The radiative loss function scales roughly with the atomic charge Z^3 in core relevant conditions for coronal equilibrium (Fig. 2.2) [58]. There-

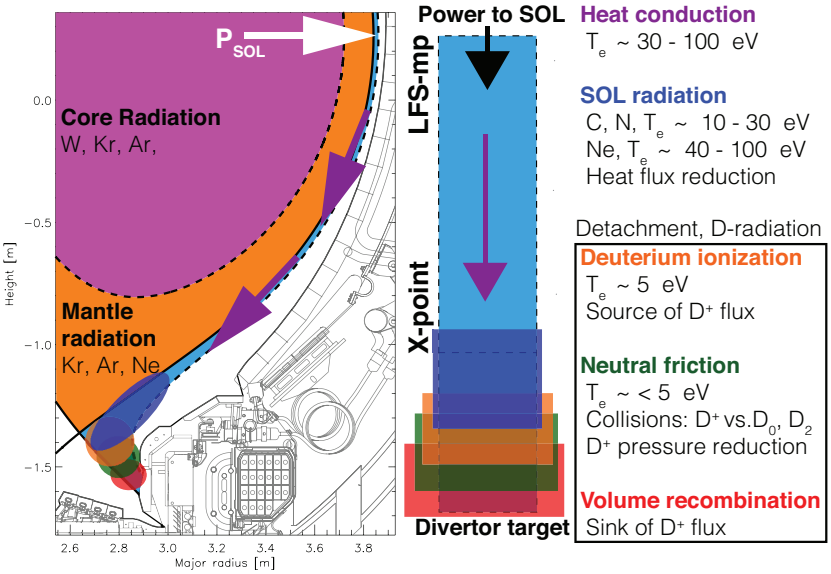

Figure 2.1. Schematic of the radiative power exhaust and radiative divertor concept in tokamak plasmas. The concept and schematic have been obtained from [31, 58, 60].

fore, higher atomic number species are more efficient radiators in the core and periphery plasma temperatures of 0.1 – 10 keV, and cause less fuel dilution (increase of Z_{eff}) for a given amount of radiated power than lower atomic number species. The maximum operational core radiation is generally limited by performance requirements in reactors. Firstly, robust high performance H-mode operation requires a minimum amount of power crossing the separatrix [22]. Secondly, fuel dilution by impurity contamination reduces the fusion power as Z_{eff}^{-2}, where Z_{eff} is the effective charge state of the plasma. Moreover, in reactor scale plasmas, the radiated power losses due electron deceleration radiation, *Bremsstrahlung*, which scale linearly with Z_{eff}, can radiate tens of percents of the alpha heating power [30, and references therein]. Therefore, strong core periphery radiators, such as argon and krypton, are used for the formation of the core periphery radiative mantle (Fig. 2.1) [5], since they allow higher P_{RAD} with less increase of Z_{eff} than less effective core radiators, such as nitrogen and neon.

The operational window for radiative cooling inside the separatrix in ITER is anticipated to be very limited, since ITER is predicted to operate only marginally above its LH-transition threshold in H-mode plasmas. In the ITER Q = 10 scenario, the total external and alpha heating power to

the plasma is estimated to be about 150 MW, whereas about 70 – 100 MW of power crossing the separatrix is expected to be required to maintain a high performance H-mode [22, 48]. However, in a DEMO-level tokamak operating with fusion powers of 2.5 – 5 GW, the core radiation contribution needs to be significantly higher to accommodate the limited radiative capability of the divertor plasma [17, 30, 48]. Furthermore, radiating most of the power in the divertor chamber at DEMO relevant power levels would yield photon power densities on the divertor components exceeding the engineering limits.

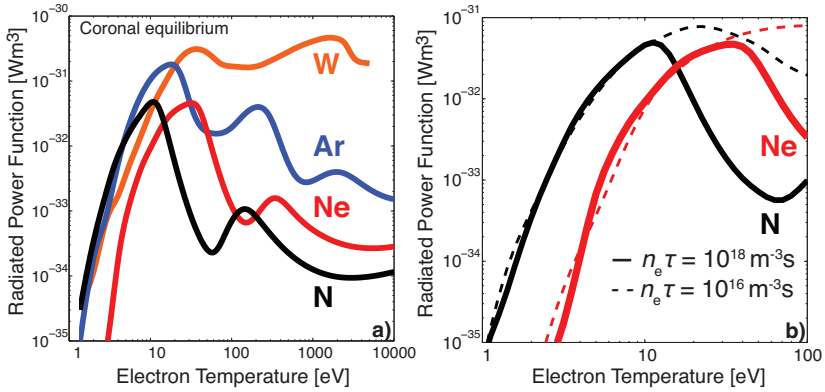

Figure 2.2. a) Radiative loss function L_z (Wm^3) in coronal equilibrium of N, Ne, Ar, and W, at an electron density of 10^{20} m^{-3}. b) Radiative loss function L_z (Wm^3) at an electron density of 10^{20} m^{-3} for impurity confinement times, τ, of 0.1 ms (dashed lines) and 10 ms (solid lines). The former represents typical JET divertor conditions, and the latter high density reactor divertor conditions [58]. The colors stand for nitrogen (black, N, Z = 7), neon (red, Ne, Z = 10), argon (blue, Ar, Z = 18), and tungsten (orange, W, Z = 74). The curves are calculated with reaction and radiation rates obtained from ADAS [61]

The second stage in the radiative power exhaust is the radiative power removal in the SOL and divertor plasma (Fig. 2.1). Once entered the SOL, the power is transported towards the divertor targets, dominantly via electron heat conduction, due to low electron inertia [31]. The power enters the SOL dominantly around the LFS-MP region. This is thought to be largely due to the following three factors:

- A tokamak plasma has a larger surface area over its LFS than HFS. Even if the power flow density across the separatrix would be uniform, the LFS SOL would receive more power than the HFS.

- The magnetic flux surfaces on the LFS are compressed with respect to the HFS due to the *Shafranov shift* of the equilibrium [12]. The flux

surfaces are more compressed at the LFS than at the HFS. If the cross-field heat flux is proportional to radial gradients, the LFS power flow is further enhanced relative to the LFS.

- The plasma curvature on the LFS is unfavorable relative to the thermal pressure gradient of the plasma [62]. Therefore, the LFS features stronger microturbulence than the HFS, increasing the cross-field transport levels. This is called *ballooning* transport [6, and references therein].

In the SOL, the total plasma pressure can be assumed approximately conserved, and the temperature reduction towards the divertor is associated with an increase in the plasma density. Deviations from an exact pressure balance along the field lines are caused by plasma momentum transport to adjacent flux tubes due to cross-field diffusion and viscosity. Near the X-point region, this can lead to pressure imbalances along the separatrix field. However, in this description of radiative divertor physics, the pressure is assumed conserved. Once the temperature downstream in the divertor is reduced to sufficiently low values, the low atomic number impurities can form a radiation zone in the divertor (Fig. 2.1). Low atomic number impurities, such as nitrogen, are strong radiators at electron temperatures of 5 – 30 eV (Fig. 2.2), while for the core and peripheral plasma temperatures they are fully stripped and their radiation is reduced to the residual Bremsstrahlung levels.

Since the impurity residence time ($\sim$ 0.1 – 1 ms) in the divertor plasma is usually significantly shorter than the collisional-radiative equilibration time (> 10 – 20 ms), the radiative losses cannot be calculated using the coronal equilibrium values (Fig. 2.2). As an impurity particle is externally injected or recycled into the divertor plasma, it emits line radiation while simultaneously ionizing to higher ionization states. The non-coronal effects can increase the effective radiative potential of the injected or recycled impurities by orders of magnitude (Fig. 2.2) [6]. Especially for nitrogen, a significant increase occurs due to the non-coronal radiation for temperatures above 10 eV. Accordingly, non-coronal effects are anticipated to have a strong impact on the nitrogen radiation in the divertor plasma. For neon, the increase takes place for temperatures above 40 eV, and the impact of non-coronal effects on the divertor radiation is anticipated to not be as significant as with nitrogen. Furthermore, neon radiation becomes significant only for electron temperatures above 10 eV.

Consequently, in JET, neon is not anticipated to be as strong a divertor radiator as nitrogen. In reactor scale devices, the stronger radiation of neon in temperatures above 15 eV may give advantage over nitrogen (Fig. 2.2).

The third step in reducing divertor heat loads to acceptable values is the achievement of plasma *detachment* at the strike point in the divertor. In divertor detachment, the plasma pressure in front of the target plate, as well as the plasma particle flux to the target plate, are strongly reduced. The most important pressure loss mechanisms in the vicinitiy of the strike points, where the particle and power fluxes are expected to peak, are charge exchange of hot plasma ions with cool recycled neutrals, collisions between deuterium ions and molecules, cross-field transport of momentum to adjacent flux tubes, and recombination due to 3-body, radiative, and molecular assisted processes [3, 58]. As a result of detachment, the power flux to the plate as well as the divertor erosion rates, which are determined by the plasma particle flux, the impurity concentration and the divertor temperature, are strongly reduced. The total energy flux incident on the divertor plate, Q_{TOT}, from electron and ions can be expressed as

$$Q_{\mathrm{TOT}} = \Gamma_{\mathrm{D}}(E_B + \gamma_e T_e + \gamma_i T_i) \tag{2.5}$$

where Γ_D is the incident particle flux, E_B the binding energy released in the surface recombination of electrons and hydrogenic ions to atoms (13.6 eV) and molecules (4.5 eV) [5, 31, 54]. The sheath heat transmission coefficients for electrons, $\gamma_e \sim 4.5$, and ions, $\gamma_i \sim 2.5$, are kinetic correction factors representing the amount of power deposited on the surface per a particle, in a given temperature, hitting the surface [31, and references therein]. The equation (2.5) shows that even if the plate temperatures are reduced to low values in the range of 1 eV, the binding energy terms is significant and further reduction of Q_{TOT} requires reduction of Γ_D, which is achieved in divertor detachment [5, 54].

2.3 Detachment

2.3.1 SOL collisionality

The divertor operation regimes are often discussed in order of increasing SOL collisionality

$$\nu = \frac{L_{\text{connection}}}{\lambda_{\text{mfp}}} = \frac{1}{K} \tag{2.6}$$

where λ_{mfp} is the Coulomb collision mean-free path, $L_{\text{connection}}$ one half of the length along the magnetic field line from LFS target to the HFS target, and K the Knudsen number for Coulomb collision [5, and references therein]. Each collisional process in the plasma has its own Knudsen number, which represents the ratio of the collisional mean-free path to the characteristics scale lengths in the system. If the Knudsen number is small for a given process (high ν), a diffusive or fluid description is valid. Otherwise, a kinetic description is required.

The thermal Coulomb collision mean free paths for self-collisions are approximately given by [31]

$$\lambda_{\text{ii}} \sim \lambda_{\text{ee}} \sim \frac{10^{16} T^2}{n_e} \tag{2.7}$$

where λ is in (m), T in (eV), and n_e in (m^{-3}). Near the divertor plate, $T \sim$ 0.1 – 20 eV, $n \sim 10^{20-21}$ m^{-3}, and $L \sim$ a few m, leading to $K \ll 1$. Therefore, fluid equations, as given in [63], are expected to give a valid description of the transport physics parallel to the magnetic field lines in this region, although non-local kinetic corrections may be required [64, and references therein]. Since electron heat conduction is dominated by the tail-end of the electron energy distribution with energies in the range of $E \sim (3-5)T_e$, and the λ_{ee} increases with E^2, kinetic corrections to the classical rates arise even for $K \sim 0.01$ [5, 64 – 66, and references therein].

If the fluid description is valid, the electron heat transport parallel to the magnetic field lines can be simulated as a fluid transport process characterized by thermal conductivity [63, 67]:

$$q_{\parallel,e} = -K_{\parallel,e} T_e = -\kappa_{0,e} T_e^{5/2} \nabla_\parallel T_e \tag{2.8}$$

The coefficient $\kappa_{0,e}$ is determined by Coulomb collisions and scales proportional to $m^{-1/2}$. Therefore, heat conduction through ion channel is a factor of $(m_e/m_i)^{1/2} \sim 60$ lower than that of electron. As a result, ion temperatures in the upstream SOL are often higher, by a factor of 1.2 – 2, than electron temperatures. Hence, whereas electron heat transport is

dominated by heat conduction, both convective transport and collisional energy transfer to electrons can be important for ions. In the divertor chamber, on the other hand, charge exchange cooling due to deuterium atom densities of 10^{20} m^{-3} can reduce local ion temperatures below those of electrons.

2.3.2 Neutral processes in the SOL and divertor

Plasma ions colliding with the PFMs in a fusion reactor recombine to form neutral atoms and molecules. In steady conditions, when the wall reservoir of these atoms, N_{WALL}, is changing slowly in time relative to the plasma flux to the wall, Φ_{D^+}, $dN_{\mathrm{WALL}}/dt \ll \Phi_{\mathrm{D}^+}$, the wall emits neutral atoms and molecules, $\Phi_{\mathrm{D}_{0,D_2}}$, approximately at equal rate to the plasma flux to the wall. This process is called *recycling*, and it provides the dominant fuel particle source in the divertor and SOL plasma. As a result of recycling, the neutral atom and molecular densities and pressures in the divertor and SOL are typically sufficiently high to have a considerable impact on the divertor plasma characteristics. Molecules and atoms originating at the PFMs travel through the plasma ions and neutrals into the plasma volume until they are ionized. Depending on the Knudsen number (collisionality) of the neutrals, this transport can be described either as a diffusive fluid or as a kinetic process. While traveling through the plasma, neutral atoms and molecules undergo excitation, de-excitation, ionization and recombination processes. The important processes for H, H^+, H^-, H_2, and H_2^+ are listed in the Tables 2.2 and 2.3 [68 – 84, and references therein].

Table 2.2. The set of atomic processes for deuterium considered most important for SOL and divertor plasmas in tokamaks.

#	Name of the process	Reaction
1.	Ionization [70, 73]	$\mathrm{D} + e \rightarrow \mathrm{D}^+ + 2e$
2.	Radiative recombination [70, 73]	$\mathrm{D}^+ + e \rightarrow \mathrm{D} + h\nu$
3.	3-body recombination [70, 73]	$\mathrm{D}^+ + 2e \rightarrow \mathrm{D} + e$
4.	Charge exchange (CX) [69, 72]	$\mathrm{D} + \mathrm{D}^+ \rightarrow \mathrm{D}^+ + \mathrm{D}$
5.	Elastic collision [71, 73]	$\mathrm{D} + \mathrm{D}^+ \rightarrow \mathrm{D} + \mathrm{D}^+$
6.	CX recombination [73, 80]	$\mathrm{D}^+ + \mathrm{D}^- \rightarrow 2\mathrm{D}$

For divertor plasmas with $n_e \sim 10^{20-21}$ m^{-3}, the times for electron excitation, de-excitation, and ionization are comparable to the radiative decay time for the excited states of hydrogen. Therefore, multistep processes

Table 2.3. The set of molecular processes for deuterium considered most important for SOL and divertor plasmas in tokamaks.

#	Name of the process	Reaction
7.	Dissociation [70, 73]	$D_2 + e \rightarrow 2D + e$
8.	Dissociative ionization [70, 73]	$D_2 + e \rightarrow D + D^+ + 2e$
9.	Non-dissociative ionization [70, 73]	$D_2 + e \rightarrow D_2^+ + 2e$
10.	Dissociative attachment [69, 72]	$D_2 + e \rightarrow D + D^-$
11.	Molecular elastic collision [71, 73]	$D_2 + D^+ \rightarrow D_2 + D^+$
12.	Ion conversion [73, 78]	$D_2 + D^+ \rightarrow D_2^+ + D$
13.	Dissociative recombination [73, 79]	$D_2^+ + e \rightarrow 2D$
14.	Dissociative excitation [69, 73]	$D_2^+ + e \rightarrow D + D^+ + e$
15.	Dissociative ionization [69, 73]	$D_2^+ + e \rightarrow 2D^+ + e$

can be important for the reaction rates. Furthermore, for electron temperatures below about 2 eV, 3-body recombination can become significant. For these reasons, a collisional-radiative treatment is necessary for hydrogenic species in MCF devices [84, 85]. Generally, the collisional-radiative treatment increases the ionization and recombination rates and reduces the radiative emission rates relative to models ignoring the multi-step, and 3-body processes, and collisional de-excitation.

In electron temperatures relevant for low to moderate electron collisionality SOL plasmas, 10 – 200 eV, the plasma conditions are strongly ionizing, and the dominant reactions for neutral atoms are ionization (reaction 1) and charge exchange (reaction 4) (Table 2.2). The charge exchange cross-section is roughly twice of that of ionization. In these conditions, charge exchange acceleration of neutral particles with hot plasma ions contributes to fuelling of the pedestal plasma. In the divertor, on the other hand, due to comparable and short ionization and charge exchange mean free paths, $\lambda_{\mathrm{CX}} \sim \lambda_{\mathrm{IZ}}$, the impact of charge exchange transport of ion momentum and energy is not expected to have a strong impact on the plasma conditions in these temperatures [5, 30, 86, 87]. The cross-sections for molecules depend on the roto-vibrational excitation levels [5]. For electron temperatures above 10 eV, the non-dissociative ionization (reaction 9) dominates over the other channels, producing D_2^+ from D_2 (Table 2.3). The resulting D_2^+ is then dissociated predominantly through the dissociative excitation channel (reaction 14), producing D^+ and D_0, which is ionized through the atomic reactions [73].

In highly collisional SOL conditions, at divertor plasma temperatures

less than 5 – 10 eV, the ionization cross-section for deuterium atoms is reduced strongly with decreasing electron temperature (Table 2.2, Fig. 2.3). As a result, the neutral atomic particles can experience multiple charge exchange (reaction 4) and elastic (reaction 5) collisions with the plasma ions before ionizing. At divertor T_e below about 1 eV, the electron-ion volume recombination due to 3-body and radiative processes (reactions 2 and 3) can become strong enough to provide a plasma particle sink comparable or greater to the surface recombination. Especially, the 3-body recombination increases strongly as a function of reducing electron temperatures below 1 eV and with increasing electron densities (Fig. 2.3).

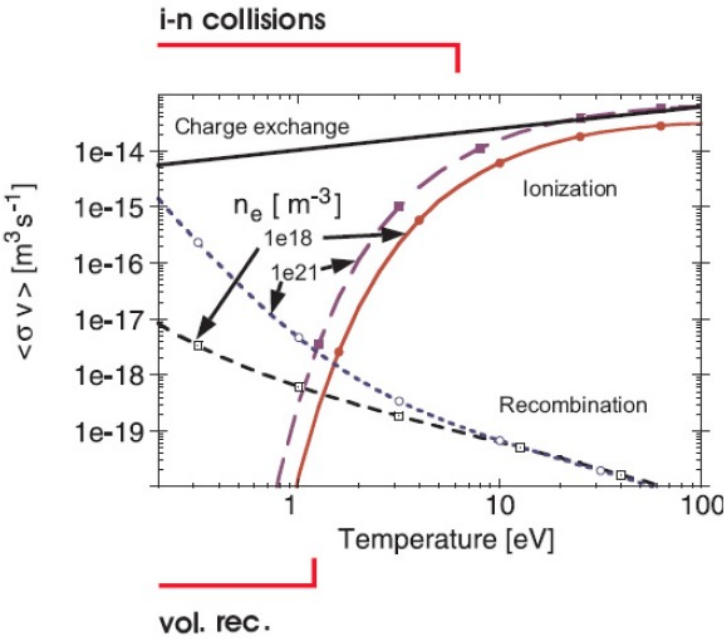

Figure 2.3. Charge exchange, recombination, and ionization rates for hydrogen as a function of background electron temperature [13, 85]

For molecules, in low temperature plasmas, $T_e < 10$ eV, dissociation of D_2 to fast, 2 – 3 eV, Franck-Condon atoms dominates over the other channels, for ground state excitation levels. Including the roto-vibrational excitations increases the reaction rates for the ion conversion (reaction 12) and dissociative attachment (reaction 10) channels, which together with dissociative recombination (reaction 13) and charge exchange recombination (reaction 6) provide molecular assisted volume recombination (MAR) [88, 89, and references therein]. In both channels, one electronically excited deuterium atom is produced. This can either decay to ground state or

be re-ionized. Only in the case of decay to ground state do these processes qualify as recombination channels [89]. Due to strong re-ionization of the produced excited deuterium atoms, the effective recombination enhancement is strongly reduced relative to expected values not taking multi-step processes into account. As a result of this effect and the fact that the vibrational distribution of the molecules does not depend on the electron density, MAR enhancement in addition to 3-body and radiative recombination channels is expected to be strongest at lowest densities [89]. Therefore, for high density, reactor scale divertor operation in ITER, volume recombination is predicted to be strongly dominated by 3-body and radiative processes ([90], and references therein). In multi-fluid modelling, the molecular elastic collision (reaction 11) is typically observed to provide a significant momentum loss channel for the divertor plasmas in low temperature conditions [68, 91 – 95].

Furthermore, at sufficiently high neutral deuterium densities, absorption of Lyman radiation becomes important in the divertor plasma. This reduces the effective recombination rates and increases the ionization rates accordingly [89, 90, and references therein]. Neutral-neutral collisions become important once the neutral collisional mean free path becomes comparable to the characteristic spatial dimension of the system [89, 90, and references therein]. Both of these effects are expected to be important for more realistic simulations of the next step devices, such as ITER, due to their larger size and higher deuterium atom densities and pressures, whereas they are expected to be of less importance in existing devices. However, Lyman radiation trapping can become significant in existing devices in high density, detached conditions, and, especially, in conditions of strongly localized radiation-condensation (MARFE-like [96, 97]) formation at the X-point.

2.3.3 SOL regimes

Increasing plasma collisionality, ν, coincides with increasing density at constant input power or increasing radiation loss at constant upstream density. For fixed input power, ν can be increased in the experiment either by increasing deuterium or impurity injection. The SOL divertor plasmas are conventionally divided into three different regimes in the order of increasing plasma collisionality: *sheath-limited*, *conduction limited*, and *detached* regime (Fig. 2.4). Figure 2.4 illustrates a representative set of experimentally measured divertor conditions with increasing plasma den-

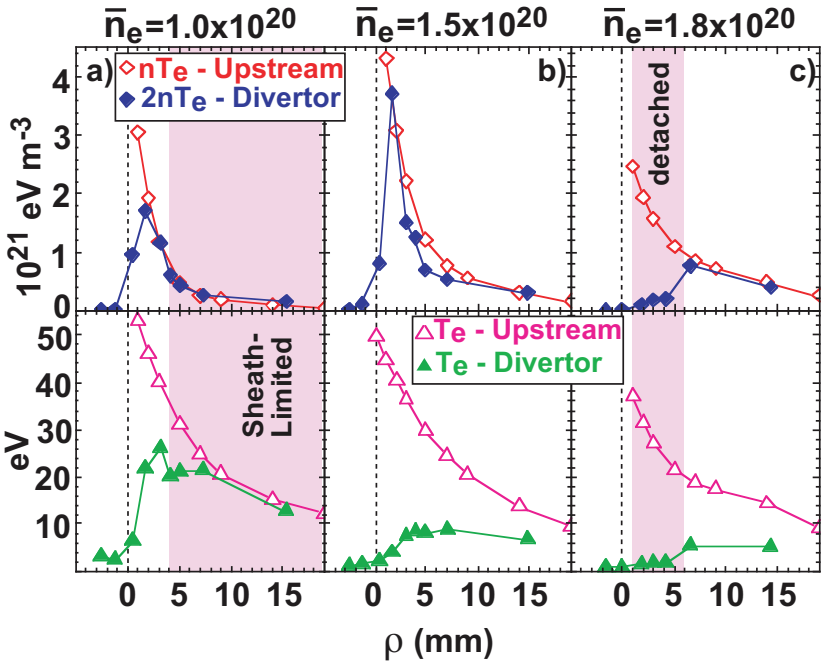

Figure 2.4. Upstream (SOL) and downstream (divertor) profiles of electron pressure and temperature for three difference SOL/divertor plasma regimes in Alcator C-mod: a) Sheath limited, b) Conduction limited / High recycling, and c) Detached. The figure is taken from [98, 99]. ρ is the flux surface coordinate mapped to the LFS-MP.

sity and collisionality in ohmically heated Alcator C-mod plasmas [98]. Different flux surfaces in the SOL as well as the HFS and LFS divertor targets do typically feature different SOL regimes simultaneously. The 3 divertor regimes can also be qualitatively observed in a collisionality (density) scan simulated with the multi-fluid package EDGE2D-EIRENE for JET H-mode conditions (Fig. 2.5). The illustrated simulations are those published in Publication I.

Sheath-limited regime

At low collisionality, $\nu \sim 2 - 10$, relevant for low density, high power, low radiation conditions, the heat conductivity is large, and little thermal variations are present in the SOL between the LFS-MP and the divertor plate ([5], and references therein) (Figs. 2.4 and 2.5). As is observed at $\rho > 5$ mm in Fig. 2.4a, both the electron pressure and temperature are conserved along the magnetic field lines between the LFS-MP and the LFS divertor target, indicating sheath limited divertor conditions (Fig. 2.4a). The heat transfer to the plate is limited by the electrostatic sheath potential forming in front of the plate [31], which is why this is called the

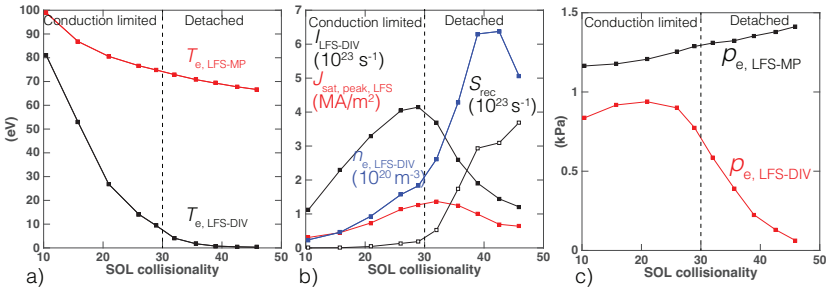

Figure 2.5. a) EDGE2D-EIRENE predictions of LFS-MP (red) and LFS-DIV electron temperatures, b) LFS-DIV total saturation current (black, solid), peak saturation current (red) and electron density (blue), total deuterium ion recombination rate in the LFS SOL below LFS-MP (black, hollow), and c) LFS-MP (black) and -DIV (red) electron pressures as a function of electron collisionality at the LFS-MP separatrix. The simulations contain deuterium as the main ions, and beryllium as an impurity species, and are published as the unseeded horizontal LFS divertor target cases in Publication I.

sheath limited divertor regime. Due to the large divertor temperatures and power fluxes, causing overheating and strong erosion of the divertor PFMs, sheath limited regimes are not considered an appropriate operational regime for MCF reactors or even for existing fusion devices with metallic PFMs.

Conduction limited regime (High recycling regime)

As collisionalities increase to values of $\nu_{\mathrm{SOL}} > 10$, the heat conductivity in the SOL is reduced, such that parallel temperature gradient is formed in the SOL. The heat transport in the SOL is predominantly limited by the ability of the plasma to conduct heat parallel to the magnetic field (Figs. 2.4 and 2.5). Hence, this SOL regime is called conduction limited. The plasma pressure is approximately conserved along the field lines in the SOL, and the temperature reduction towards the divertor is accompanied by an increase in the plasma density downstream (Fig. 2.4b, c, and 2.5). Cross-field spreading of momentum is expected to occur due to cross-field transport and viscosity, which is why exact pressure balance between LFS-MP and targets cannot be assumed, as is seen in the presented EDGE2D-EIRENE simulations as well (Fig. 2.5c). T_e at the sheath can be reduced in this regime, since the power flow through the sheath is maintained by elevated n_e at the sheath edge. In the ohmic C-Mod example, conduction limited divertor conditions are also observed near the strike point in the low n_e plasma (Fig. 2.4a) and in the far SOL, $\rho > 5$ mm, in the high n_e plasma (Fig. 2.4c).

The divertor quantities in conduction limited regime can be estimated by the *2-point model* (2PM) assuming pressure conservation in the SOL, for reasons discussed above, and that the heat is transported parallel to the magnetic field lines entirely via electron heat conduction without volumetric power losses. The latter assumption is approximately equal to assuming that the electron-ion heat transport is fast enough to ensure that the dominant ion cooling channels is heat transport to the electron channel, which eventually conducts the heat to the plate. With these assumptions, and assuming that the divertor temperature, T_t, is at least a factor of 2 lower than the upstream temperature, T_u, as well as neglecting the surface recombination heat flux (Eq. 2.5), one obtains relations for T_t, T_u, n_t, and Γ_D as a function of n_u:

$$\begin{aligned} T_u &\approx \left(\frac{7 q_u L}{2\kappa_0}\right)^{2/7} \\ T_t &\propto n_u^{-2} \\ n_d &\propto n_u^3 \\ \Gamma_D &\propto n_u^2 \end{aligned} \tag{2.9}$$

As is observed experimentally, T_t is reduced and Γ_D increased proportional to n_u^2. Due to the strong increase of Γ_D, the conduction limited regime is often called the high recycling regime. Furthermore, it is observed that T_u is not predicted to depend on any other machine parameters than on the upstream heat flux. These kinds of relations are qualitatively observed in the more complete EDGE2D-EIRENE model also, although the 2PM-like dependencies on n_u are not preserved exactly (Fig. 2.5). The peak and total ion saturation currents represent the plasma currents and fluxes to the divertor plate, and are used here to be directly comparable to experimental measurements. Experimentally, the saturation currents are measured with electrical probes called Langmuir probes, which measure the local I-V-characteristics of the plasma [31, 100]. The saturation value of the ion current with increasing negative voltage is directly proportional to the local plasma flux.

The reduction of T_t in the conduction limited regime reduces physical sputtering of the divertor plates, which reduces the main plasma contamination levels and damage to the divertor PFMs. This is a routine operational regime in existing tokamaks. However, in reactor scale devices, the increase of divertor particle fluxes would yield recombination heat fluxes (Eq. 2.5) exceeding the engineering limits, and reduction of divertor particle fluxes is required to reduce the heat fluxes within PFM limits.

Detached regime

The detached divertor regime occurs as an extension of the conduction limited regime to high SOL collisionalities. Plasma detachment is a state in which large pressure gradients are observed parallel to the magnetic field lines [86]. Experimentally, detachment is observed as a distinct reduction of divertor target pressures and saturation currents with increasing collisionality (Figs. 2.4 and 2.5). In density scans, one of the most typical characteristics of detachment is the *roll over* of the measured ion saturation currents at the divertor plate (Fig. 2.5b). As a result of the reduced plasma pressure and particle fluxes at the divertor plate, the plasma recombination power fluxes to the divertor PFMs are strongly reduced. Therefore, divertor detachment is expected to provide access to PFM heat loads within the material limits 5 – 10 MW/m^2 in reactor scale devices, while operating at upstream SOL plasma conditions consistent with the desired machine performance chacteristics (Eq. 1.2) [6, 17].

Early analysis of detachment processes concentrated on ion-neutral frictional processes as the explanation for the observed pressure and flux reduction in the divertor chamber [86, 87, 101, and references therein] . Later studies showed that although the ion-neutral friction processes can explain the observed pressure drop along the field, they cannot explain the reduction of the integral particle flux to the plate [102]. Inclusion of volume recombination processes were found necessary in both numerical and analytical models to reproduce the experimentally observed reduction of divertor particle fluxes with increasing n_e [103, 104]. Strongly recombining divertor plasmas in detached conditions were first experimentally observed in Alcator C-Mod [105], and later on also on other tokamaks: JET [106], DIII-D [107], and AUG [108].

As the divertor electron temperatures are reduced below 5 eV, the peak deuterium ionization front detaches from the divertor plate and moves upstream. As a result, a region of high deuterium atom and molecule density is formed between the ionization front and the divertor target (Fig. 2.1). The frictional processes between the deuterium ions, atoms, and molecules transfer momentum and energy from the plasma to the neutral particles. Hence, plasma pressure in the divertor leg is reduced relative to the upstream LFS-MP pressures (Figs. 2.4 and 2.5). Furthermore, if the divertor temperatures in front of the plate are reduced in the range of 0.1 – 2 eV, the electron recombination rates by 3-body, radiative and MAR processes can provide further reduction of the plasma particle,

momentum and energy fluxes (Fig. 2.5). 3-body recombination, indicative of electron temperatures well below 1 eV and electron densities above 10^{20} m^{-3}, is predicted to dominate over the other two recombination channels for typical divertor conditions in ITER [89, 109]. Experimentally, MAR has generally been found to be low in tokamaks [99]. Having stated that, in low density conditions, where the 3-body recombination rates are reduced, MAR can reach recombination rates similar to those of 3-body recombination [110]. Further plasma momentum loss in the vicinity of the divertor strike point can be provided by cross-field viscosity and transport of particles. In [111], improvement in agreement between simulated and measured divertor conditions in high-recycling and detached plasmas were obtained by rescaling the divertor cross-field transport by factors of 1 – 10 relative to the cross-field transport in the main SOL. These transport processes can be driven by, for example, high poloidal β instability-driven plasma convection in the region of low poloidal magnetic field near the X-point [112, and references therein].

Various levels of detachment can be defined. In *partially detached* conditions, a part of the plasma-wetted area is in a detached state, while the remaining SOL remains attached to the plate [113]. In these conditions, the ionization front has detached from the section of the plate considered detached, but attached to the rest of the plate. If ν_{SOL} is increased from a partially detached state, the plasma will evolve towards a *complete detachment*, where the plasma is detached throughout the radial extent of the divertor target, and the ionization front is completely detached from the divertor target. Partially detached divertor plasma is thought to be more controllable than a completely detached plasma. Furthermore, complete detachment is thought to be correlated with reduction of the main plasma performance. Due to these reasons, the target operation regime considered for ITER is partial divertor detachment [6].

Based on particle conservation arguments, the total particle sources and sinks must balance each other in plasmas in quasi steady-state conditions: $dN/dt \ll S$, where N is the total number of particles and S is the total source rate in the system. The source for plasma particles is provided by ionization of recycled and injected atoms and molecules, I_{IZ}, and the total sink is determined by the main chamber wall flux, I_{WALL}, divertor target flux, $I_{\mathrm{DIV,\,LFS\,+\,HFS}}$, and volume recombination, I_{REC}, of these particles:

$$I_{\mathrm{IZ}} \approx I_{\mathrm{WALL}} + I_{\mathrm{DIV,\,LFS\,+\,HFS}} + I_{\mathrm{REC}} \tag{2.10}$$

Therefore, the particle fluxes to the divertor plates, $I_{\mathrm{DIV,\,LFS\,+\,HFS}}$, can be reduced by any of the following mechanisms [5, 104, 114, 115] (also Publication III):

- Increase in the deuterium volume recombination rate, I_{REC}.
- Reduction in the deuterium ionization rate, I_{IZ}.
- Increase of main chamber wall recycling, I_{WALL}, relative to divertor recycling, $I_{\mathrm{DIV,\,LFS\,+\,HFS}}$.

Pioneering work on identifying the reduction of I_{IZ} as a significant contributor in the experimentally observed divertor particle flux reduction in detachment was conducted in Alcator C-Mod tokamak [115]. Similar to the work in this doctoral thesis (Publications II and III), the reduction of power flow into the ionizing zone in the divertor was inferred as the cause of reduced deuterium ionization in [115]. Detachment with very low volume recombination sinks was experimentally observed with nitrogen injection in [115]. Pioneering work on investigating experimentally the increase of main chamber recycling levels with increasing degree of divertor detachment was also conducted in Alcator C-Mod tokamak [114].

Any satisfactory explanation of detachment must obey particle, momentum, and energy conservation equations simultaneously. The total electron cooling rate by deuterium recycling is approximately linearly proportional to the total deuterium recycling rate with the electron cooling potential in the range of 20 – 30 eV for an ionization event ([31], and references therein). The electron cooling rate due to interaction with deuterium atoms and molecules is composed by photon production, ionization, and dissociation. The electron cooling rates increase non-linearly to high values for $T_e <$ a few eV. However, since neutrals tend to simply pass through the low T_e regions in tokamak divertors to be ionized and excited at higher T_e values, these high electron cooling rates at low T_e are not of much importance. Therefore, reduction of the divertor particle fluxes without any increase in the main chamber or volumetric recombination rates would yield reduction in the total deuterium recycling and electron cooling rates. However, even if the deuterium recycling and electron cooling rates are reduced, the measured radiated power from the plasma by deuterium can still increase. This can happen if the volume recombina-

tion increases simultaneously with reduction in the total volume and surface recombination. The measured radiated power from the plasma can increase due to the volume recombination contribution, which does not contribute to cooling electrons, since this is ionization potential energy radiated out of the plasma. Therefore, such lower deuterium recycling plasma state can only be achieved if the total power flow into the deuterium ionization zone in the divertor leg is reduced. Possible pathways for this reduction are changes in the power transport distribution between the main chamber wall and divertor legs, and radiative power exhaust in the plasma above the deuterium ionization front. Hence, detachment scenarios without extrinsic impurities are not expected to satisfy the particle and energy conservation equations simultaneously without an increase in either the main chamber recycling or volumetric recombination rates. In the EDGE2D-EIRENE simulations presented in the Fig. 2.5, the divertor particle flux reduction is obtained almost solely via increasing volume recombination rate with increasing ν_{SOL}. However, increase in the radial particle and power transport to the main chamber wall with increasing degree of divertor detachment and resistivity might as well play a role in the experimentally observed particle flux reduction, but not be appropriately captured by these EDGE2D-EIRENE simulations [114 – 119].

When using impurity seeding to increase the radiative power fraction in the plasma to raise ν_{SOL}, the deuterium ionization rate can, on the other hand, be reduced without violating the energy conservation equation (Publication III). In this situation, the impurity radiation provides the dominant power exhaust channel for the SOL plasma, and an increase in the deuterium ionization rate is not required to maintain the power dissipation in the divertor. With sufficient pressure reduction to limit the deuterium ion flow into the recombination region downstream in the divertor leg, the recombination rates can be reduced simultaneously with the ionization rate. Hence, the plasma can obtain a lower total deuterium recycling state, resulting into reduced divertor particle fluxes, as is observed experimentally [115] and (Publications II and III).

2.3.4 Impact of divertor geometry

Divertor development was one of the key drivers of design and upgrade of the existing tokamaks in the 1990s [120 – 130, and references therein]. These divertors have been designed and optimized with the aid of multi-fluid SOL plasma simulation tools, which are discussed in the section 2.4.

The aim in the design has been to optimize the benefits that can be expected from a successful divertor operation:

- A large operating range of SOL collisionality in partially detached plasma conditions with high radiative power losses, acceptable divertor surface heat fluxes below 10 MW/m^2, and low PFM erosion levels.

- Sufficient particle control by efficient pumping of impurities and main fuel ions, as well as by retention and enrichment of impurities in the divertor plasma.

- Helium exhaust capability to remove fusion ash in the next step devices.

Furthermore, divertors achieving these milestones are expected confine divertor recycling neutrals in the divertor chamber. This can contribute to reducing neutral pressures and ionization sources in the main SOL and peripheral plasma, and charges exchange sputtering of the main chamber wall. However, there is substantial experimental evidence of direct plasma recycling at the main chamber wall due to the formation of broad density shoulders in the SOL in high density, detached conditions [114, 117, and references therein]. The main chamber neutral source caused by direct plasma recycling at the main chamber wall is independent of the divertor geometry and can dominate the neutral pressures outside the divertor chamber. Furthermore, interaction of ELMs with the main chamber PFMs is expected to cause a main chamber neutral source that is also independent of divertor geometry. Due to these reason, divertor geometry is expected to have only a limited impact on the main chamber neutral pressures. In addition, following the better confinement of neutrals in the divertor chamber, the sub-divertor pressure is expected to increase relative to more open divertor configurations. This is expected to facilitate pumping efficiency, and control of fuel and impurity particle densities.

The effect of divertor geometry on the divertor plasma conditions is largely associated with the transport and distribution of neutrals, plasma, and impurities in the divertor. The motion of the neutral particles is not restricted by the magnetic field lines. Therefore, the divertor geometry, such as the angle of the magnetic field line to the surface normal, proximity of the divertor side baffles to the plasma, as well as proximity of the

divertor pumps to the plasma, can play a significant role in determining the neutral particle distribution in the divertor plasma (Fig. 2.6). As a result, the neutral interaction and ionization distribution in the plasma are changed as well, impacting the plasma conditions, flow velocities and profiles, impurity source profiles, and impurity densities in the divertor. The impact of divertor geometry on the divertor performance has been systematically studies in many tokamaks (Fig. 1 in [125]): Alcator C-Mod [99, and references therein], JET [120 – 122, and reference therein], AUG [123, 127, and reference therein], DIII-D [124, and references therein], and JT-60U [128, and references therein].

The conventional strike point angle configurations compared to each other are horizontal and vertical configuration (Fig. 2.6). Pioneering experimental work on identifying the benefits of vertical divertor when compared to horizontal divertor was conducted at Alcator C-Mod tokamak [99, and references therein]. These studies were followed by dedicated divertor geometry investigations on other tokamaks: JET [120 - 122, and references therein], AUG [123, and reference therein], and DIII-D [124, and references therein].

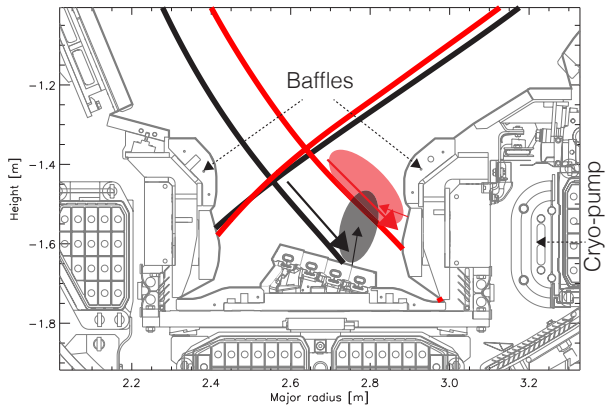

Figure 2.6. Vertical (red) and horizontal (black) LFS divertor configuration in JET high-triangularity configurations. The black and red arrows represent the direction of plasma flux to the wall and average direction of the recycling neutrals.

Strike point detachment is foreseen necessary in ITER to reduce the divertor peak heat loads below 10 MW/m^2, while producing 500 MW of fusion power [6]. Therefore, the divertor design have been optimized to maximize the volumetric losses near the separatrix. The vertical divertor geometry is predicted to facilitate neutral recycling towards the separatrix in the divertor, therefore, enhancing the ionisation near the separatrix and concomitantly the densities and volumetric power losses in

this region [99, 125, and references therein]. As a result, strike point detachment is expected at lower upstream densities and collisionalities, lower impurity concentration levels, and lower radiative power levels in the vertical than in the horizontal divertor configuration. Hence, the operational space between partially and fully detached conditions is expected to be wider in the vertical divertor configuration. This is typically observed in multi-fluid simulations (Fig. 2.7). In the illustrated series of EDGE2D-EIRENE simulations, the vertical LFS divertor strike point detaches at about 30% lower SOL collisionality than the horizontal LFS divertor strike point. The strike point detachment is interpreted to occur once the peak particle flux to the plate rolls over, illustrated with dashed lines in the figure. In these simulations, this occurs when the LFS strike point electron temperature is reduced below 1.5 – 4 eV. Furthermore, it is observed that in the vertical configuration, the total LFS divertor particle flux continues increasing with increasing collisionalities that are greater than the strike point detachment threshold. This indicates partially detached divertor conditions, where the strike point is detached, while the far SOL is still in high-recycling regime experiencing increasing particle fluxes with increasing plasma density and collisionality. On the other hand, in the horizontal configuration, the total divertor particle flux is reduced to one half of the peak value at SOL collisionality values exceeding the strike point detachment threshold only by 10%. Therefore, the operational window in partially detached divertor conditions in the simulations is significantly wider in the vertical than in the horizontal LFS divertor configuration.

Although the impact of divertor geometry on the detachment characteristics is experimentally observed in Alcator C-mod ([99], and references therein), ASDEX Upgrade ([126], and references therein), and JT-60U [128], the initial experimental results from JET-Mk I divertor showed only little difference in the approach to detachment between the two configurations [102, 129]. Consistently, more recent L-mode experiments in JET with the ITER-like wall configuration showed also only minor differences, of the order of 20%, in the approach to detachment between the two configurations [131]. In contrast, multi-fluid modelling with EDGE2D-EIRENE showed a clear impact of the configuration on the divertor conditions in JET-ILW [131]. It was hypothesized that gas re-circulation within the divertor structure, producing complicated ionisation patterns, as well as unaccounted plasma transport processes in the main SOL and divertor,

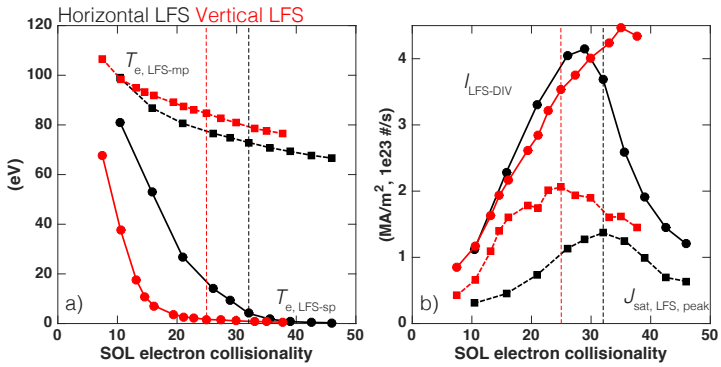

Figure 2.7. EDGE2D-EIRENE predictions of LFS mid-plane, $T_{e,\,\text{LFS-MP}}$, and divertor strike point, $T_{e,\,\text{LFS-sp}}$ electron temperatures (a) and total, $I_{\text{LFS-DIV}}$, and peak, $J_{sat,\,\text{LFS, peak}}$, LFS divertor particle current (b) as a function of SOL electron collisionality in unseeded H-mode plasmas in JET with the ITER-like wall. The collisionality levels corresponding to LFS strike point detachment are illustrated with dashed lines. The catalogs of the simulations illustrated in the figure can be found in the appendix 1c in Publication I.

masked some of the geometry effects in these studies.

Sub-divertor pressures are expected to increase with divertor closure, as has been previously observed [125, 131, 132]. Pedestal fuelling and sub-divertor neutral pressures are coupled to each other, as was indicated by recent work extending EDGE2D-EIRENE to model the sub-divertor structures in JET [132]. In JET L-mode simulations, in low density plasmas, the sub-divertor pressures were higher in vertical than in horizontal for a given LFS mid-plane separatrix electron density, $n_{e,\,\text{sep,\,LFS-MP}}$, due to reduced neutral leakage to pedestal plasma in the vertical configuration [132]. As a result, higher divertor recycling levels and sub-divertor neutral pressured were needed in the vertical configuration to reproduce the same $n_{e,\,\text{sep,\,LFS-MP}}$ as in the horizontal configuration. Furthermore, the simulations indicated that the vertical LFS divertor effect on the LFS divertor profiles was only observed in the simulations if the JET horizontal tile (located in the PFR in vertical configurations) was assumed reflective for neutrals in the model. Therefore, neutral leakage in the PFR would be expected to reduce the impact of divertor geometry on the divertor profiles. In this doctoral thesis, in Publication I, these studies were extended to investigate the effect of the divertor plasma configuration on the radiative divertor conditions in baseline H-mode plasmas in the JET ITER-like wall.

2.3.5 Divertor asymmetries

To maximize the plasma-wetted area and to minimize the peak PFM heat loads, the SOL power load should be distributed as evenly as possible over the exposed divertor targets. Furthermore, the operational window in SOL density, power, and impurity injection levels are typically determined by the need to remain within a certain SOL collisionality and divertor regime, such as partially detached divertor operation in ITER [6]. In other words, the LFS divertor must be partially detached in ITER to maintain the peak PFM heat loads below the design specification of the tungsten PFMs. If the SOL parameters required for partial LFS divertor detachment lead to complete detachment of the HFS divertor leg in ITER, the control of plasma fuelling, impurity levels, pumping, and ultimately performance might be impacted adversely. Therefore, any asymmetry in the divertor power deposition or density, temperature, or radiation levels is a concern for the design of operational scenarios in the next step devices.

Strong asymmetries in divertor conditions and deposited power levels are observed between the divertor targets in existing devices for low and high recycling SOL conditions [31, 133 – 148, and references therein]. These asymmetries are associated with the four following contributors [31, 133 – 136, and references therein]:

- LFS to HFS asymmetries in power crossing the separatrix (section 2.2).

- *Cross-field guiding centre drifts* ($\mathbf{E} \times \mathbf{B}$ and diamagnetic), driven by the combination of electric and magnetic fields, as well as by curvature and gradients of the magnetic field.

- *Currents* in the SOL.

- Toroidal momentum transport from the rotating core plasma.

The cross-field drift and some of the current driven components change direction with changing toroidal magnetic field B_Φ ([134] and references therein). The *normal* direction for B_Φ in JET, and in many other tokamaks, is negative in the right handed cylindrical coordinate system (r, Φ, z) with z pointing vertically upwards [140]. This means that the $\mathbf{B} \times \nabla B$-

drift for ions points downwards towards the active X-point. This is called the *forward* field configuration. The configuration with a positive B_Φ, with the $\mathbf{B} \times \nabla B$-drift pointing away from the active X-point, is called the *reversed* field configuration.

In lower single null divertor configuration, in the normal field direction, LFS to HFS-divertor asymmetries of the order of a factor of 2 are typically observed in low and high recycling SOL regimes ([6, 133, 134] and references therein). These asymmetries lead to

$$\begin{aligned} T_{\text{HFS, DIV}} &< T_{\text{LFS, DIV}} \\ n_{\text{HFS, DIV}} &> n_{\text{LFS, DIV}} \\ P^{\text{RAD}}_{\text{HFS, DIV}} &> P^{\text{RAD}}_{\text{LFS, DIV}} \\ P^{\text{DIV}}_{\text{HFS, DIV}} &< P^{\text{DIV}}_{\text{LFS, DIV}} \end{aligned} \tag{2.11}$$

where P^{RAD} is the radiated power in the divertor leg, and P^{DIV} the deposited power on the divertor plate. Therefore, as ν_{SOL} is increased, the HFS divertor tends to enter the conduction limited and detached regimes at lower ν_{SOL} than the LFS divertor. Related to LFS to HFS asymmetries, the operational window in the ITER simulation is limited below a certain ν_{SOL} and sub-divertor neutral pressures by the onset of complete HFS divertor detachment [90, 140, and references therein]. However, these simulations do not include cross-field drifts or currents. Therefore, there is concern that the operational window in ν_{SOL} and in subdivertor neutral pressures is smaller than predicted by the model. The work on extending these simulations to include drifts is presently ongoing. Nevertheless, since the impact of drifts is expected to scale proportional to the ratio of the ion poloidal *gyro radius* (the radius of the gyro-motion of the ion, given by the *Lorentz* force in a given magnetic field) to the characteristic width of the SOL [134], the impact of drifts might reduce as a function of the machine size and poloidal magnetic field and plasma currents levels.

Divertor asymmetries are typically reduced in reversed field configuration, indicating a strong role of field dependent cross-field drifts and currents in formation of the LFS to HFS asymmetries [133 – 140, and references therein]. The main guiding centre drifts are illustrated in the Fig. 2.8 for the normal field direction. The poloidal and radial $\mathbf{E} \times \mathbf{B}$-drifts are considered the most important drift contributors for the divertor LFS to HFS asymmetries [134, 135]. The poloidal $\mathbf{E} \times \mathbf{B}$-drift transports plasma from the HSF to LFS, and produces LFS to HFS power balance asymmetries consistent with experimental observations [134, 135]. However, the

poloidal $\mathbf{E} \times \mathbf{B}$-drift alone would increase the LFS densities relative to the HFS densities, in contrast with the experimental observations. The radial $\mathbf{E} \times \mathbf{B}$-drift, on the other hand, provides particle transport from the LFS SOL to the PFR, where the poloidal $\mathbf{E} \times \mathbf{B}$-drift leads to particle transport from the LFS divertor to the HFS divertor, and the radial $\mathbf{E} \times \mathbf{B}$-drift further into the common SOL in HFS divertor leg (Fig. 2.8) [134]. This particle transport channel from LFS divertor leg to the HFS divertor leg is conventionally thought to be a major contributor in the experimentally observed higher divertor densities, radiated power levels and lower temperatures in the HFS divertor leg relative to the LFS divertor leg. Since these drifts change direction with the reversal of the field direction, in reversed field plasmas, this mechanism would bring particles from the HFS divertor leg to the LFS divertor leg, therefore balancing the LFS to HFS asymmetries given by the field independent contributors. As a result, more balanced HFS and LFS divertor conditions are expected for reversed field plasmas, and observed experimentally [134 – 136, and references therein]. These radial $\mathbf{E} \times \mathbf{B}$-drifts are consistent with monotonically increasing electric potentials towards the LFS-MP in SOL. In DIII-D, electric potential hills are experimentally observed near the X-point in L- and type-III ELMy H-mode plasmas [137]. These hills are predicted to lead to convective $\mathbf{E} \times \mathbf{B}$-circulation around the X-point due to the change of the direction of the radial $\mathbf{E} \times \mathbf{B}$-drift flows passing through the confined region next to the X-point [137] (Fig. 2.8). However, these flows are suggested to be incompatible with H-mode plasmas by Schaffer et al. [137], and, therefore, the conventional radial $\mathbf{E} \times \mathbf{B}$-drift flows as described by the blue arrows in the Fig. 2.8 are more likely to be compatible with the H-mode plasmas in this doctoral thesis.

Currents in the SOL are also expected to provide power deposition and divertor condition asymmetries in tokamaks [134, 147, and references therein]. Thermoelectric currents flow between the divertor targets, due to the electric field caused by the sheath potential differences at opposite divertor targets [134, 147, 149, 150, and references therein]. Electron pressure asymmetry can also drive parallel current, and might be important if the divertor electron temperatures around the strike points at HFS and LFS targets are nearly equal [151]. The target with lower T_e and/or higher p_e receives positive current from the plasma [134]. Therefore, the thermoelectric current usually flows from the LFS to the HFS side in the normal field configuration and from the HFS to the LFS side

in the reversed field configuration. As a result, the thermoelectric current provides effective electron heat convection towards the LFS target in the normal field configuration, therefore amplifying the LFS to HFS asymmetries in T_e [134, 135, 147, and references therein].

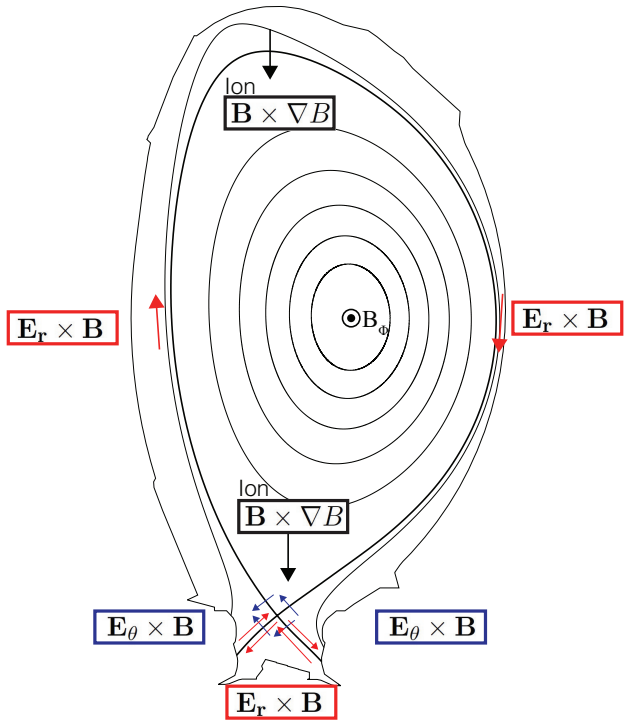

Figure 2.8. Schematic illustration of the main guiding center drifts for the case of normal field direction. The direction of all the drifts is reversed for the reversed field direction. The schematic is reproduced from [134, 147].

The volumetric power losses due to interaction of the plasma particles with deuterium atoms and molecules and impurities increase typically non-linearly with reducing T_e and increasing n_e for a given plasma pressure. Therefore, the LFS to HFS asymmetries are expected to be enhanced by volumetric processes in each divertor leg [134, 136]. As a result, relatively small asymmetries in the LFS to HFS power sharing could theoretically lead to substantial differences in the observed LFS to HFS divertor conditions, especially for suitable ν_{SOL} values close to divertor regime boundaries [134, 136].

2.4 Fluid simulation tools for divertor performance studies

At the time of writing this doctoral thesis, the ITER design is largely finalized, most of the components are being manufactured, and large international efforts and resources are being invested in the DEMO reactor designs [17]. Despite this, significant gaps do still exist in the technology and scientific understanding, needed to be closed to ensure that these devices will perform according to their design specifications [17]. Power and particle exhaust is one of the most critical issues to be properly assessed in the design as well as in preparation of the operation, since the components designed for exhausting the power fluxes from the plasma must be able to function properly in the operational window determined by the plasma performance criteria. The ITER power exhaust components have been designed by utilizing the fluid simulations code package SOLPS ([90] version 4.3). The verification and validation of this code package, its later versions, and similar code packages such as SOLPS5.x, SOLPS-ITER, EDGE2D-EIRENE, UEDGE, SONIC, and EMC3-EIRENE, for existing devices is, however, still a subject of extensive research [44 – 46, 152 – 156]. These numerical tools do not yet reproduce quantitatively the experimental observations in high density ($0.5 - 1.0\times10^{21}$ m^{-3}), low temperature (0.1 – 5 eV) regimes, which are favored in fusion reactors due to their beneficial properties for power exhaust control [54].

This thesis contributes to this area of research. The fluid simulations code package EDGE2D-EIRENE is used to interpret impurity injection experiments, as well as to validate the model predictions, of high-power fusion test reactor scenarios ([157], and references therein) in JET. The aim of the work is to gain understanding on the interplay of the physics processes in the heat load mitigation with impurity radiation, as well as to provide benchmark of the fluid simulation tools against experimental data to validate these models for reactor design and operation predictions.

2.4.1 EDGE2D-EIRENE

EDGE2D-EIRENE is a hybrid code consisting of a multi-fluid plasma solver, EDGE2D, coupled to a kinetic Monte Carlo neutral transport code EIRENE [44 – 46]. Plasma transport is a kinetic phenomenon, occurring in a six-dimensional phase space. However, most physical problems in realistic geometry are not tractable in a fully kinetic description. Therefore, the conventional approach is to reduce the complexity of the calculations

by using conservation equations given by fluid velocity moments of the kinetic equation. The first three moments yield the conservation equations for particles/density, momentum/velocity, and energy/temperature. Kinetic effects are introduced in the system by closing the n^{th} moment equation at the n +1 level. In plasma physics, this hierarchy with the assumptions of magnetization and short mean free paths lead to the Braginskii equations, which are solved for the fuel ions and electrons in the parallel to the magnetic field direction by EDGE2D [63]. As was discussed in section 2.3.1, this assumption is often only marginally justified in SOL plasmas. The equation system is closed by employing short collisional mean-free path approximation to obtain the Spitzer-Härm heat conductivities [67]. However, it is an issue in the multi-fluid codes that as the Knudsen number of the SOL plasma increases to values above 0.01, thus kinetic effects due to parallel gradients and non-zero collisional mean-free paths arise [64, and references therein]. In these conditions, the Spitzer-Härm heat conductivites would yield unphysically large conducted heat fluxes. To avoid unphysically large heat fluxes in multi-fluid codes, the maximum simulated heat-flux is often limited to some specified fraction ($\sim 0.05 - 3$) of the free-streaming Maxwellian flux [31, 64, 158, and references therein]. In this study, heat-flux limiters are not used in the simulations corresponding to Publications I – IV, and VI, whereas in Publication V constant values of 1.5 are assumed for both electrons and ions, as suggested in [64]. In the radial, or cross-field direction, anomalous turbulent transport is described by imposing radial transport coefficients for particle diffusion and convection, and electron and ion heat conduction as input parameters to EDGE2D-EIRENE. These are adjusted to reproduce measured density and temperature profiles at the edge of the main plasma and main SOL in a specified reference plasma in each individual study, as described in the publications. The computational grid in EDGE2D is constructed according to a magnetic equilibrium reconstruction (EFIT) [159 – 161]. The calculation grid does not extend radially to the main chamber or to the PFR wall.

For the impurities, the model calculates particle and momentum conservation equations, while assuming equal temperature with the main fuel ions. The parallel momentum equation for impurities is very similar to the impurity force equation described in the context of tungsten transport in the chapter 3. In the radial direction, cross-field diffusion with a user-specified diffusion coefficient is used. Assuming the same temperature

for impurities and main fuel ions reduces the number of equations to be solved. This is justified by the fact that the hydrogen ion-impurity collision time in the divertor is shorter than the impurity residence time [165]. Furthermore, the model determines the full non-coronal distribution of the impurity charge states based on ionization, recombination and radiation coefficients retrieved from the ADAS database [61]. The version of EDGE2D-EIRENE used in this doctoral thesis was able to handle 2 impurity species simultaneously. This was sufficient for carbon wall discharges to model both carbon and the seeded impurity species. For JET-ILW, only either beryllium or tungsten could be simulated in addition to the seeded impurity. Beryllium was chosen as the simulated impurity species, since it is anticipated to radiate predominantly in the SOL whereas tungsten is anticipated to radiated predominantly inside the separatrix. Therefore, taking into account the effect of beryllium was expected to be more relevant for the divertor physics studies than the effect of tungsten. Further discussion on the topic can be found in Publication II.

Cross-field drifts and currents are omitted in the simulations in this doctoral thesis, since converged EDGE2D-EIRENE simulations were not obtained with the drift terms turned on at the time of writing this report. This is anticipated to compromise the ability of the code to model the LFS to HFS divertor asymmetries (section 2.3.5). Another limitation of the simulations setup in terms of divertor asymmetries in this study, is that the ballooning dependence on the magnetic field structure was not used in the cross-field transport model (sections 2.1, and 2.3.5). Rather the diffusion in the simulations in this study depends on the transport coefficients and radial derivatives of densities and temperatures only. The transport coefficients are typically assumed to be poloidally symmetric, favoring enhanced transport in regions with high flux compression, i.e., both HFS and LFS mid-plane. Neglecting those two effects is likely to bias the HFS divertor plasma conditions towards hotter and less dense solutions in the simulations, while the plasma conditions at the LFS divertor are anticipated to be less dependent on these missing physics models. Due to these reasons, the focus in this doctoral thesis has been on the observations in the LFS divertor leg, which is the divertor leg receiving higher target heat flux. Recent studies in L-mode plasmas indicate that the strongest impact of drifts on the plasma solution are observed in attached low- and high-recycling conditions, where the radial $\mathbf{E} \times \mathbf{B}$-drive in the divertor plasma is still significant, whereas in low temperature, detached conditions, the

sheath-potential driven plasma potential gradients in the divertor are significantly reduced, lowering the $\mathbf{E} \times \mathbf{B}$-drive as well [135, 147, 148, and references therein].

Plasma density and temperature decay parameters are specified as boundary conditions to the code. The relevant parameters are described in the publications. Inside the separatrix, the simulation grid extends up to about 10 – 15 cm inside the separatrix at that LFS-MP. At the core boundary, the power entering the simulated region is specified and flux conservation is assumed for particles. At the divertor targets, plasma flow equal to or higher than the sound speed at the sheath boundary was assumed according to the Bohm-Chodura criterion [32, 33]. The transport power flow through the sheath was calculated using the values for the electron sheath heat transmission coefficient of 4.5 and the ion sheath heat transmission coefficient of 2.5 [31].

EIRENE is a kinetic Monte Carlo neutral transport code following neutral particles originating due to neutral gas injection, erosion, recombination, and recycling in the simulation. EIRENE provides as an output the neutral atom, molecule, and D_2^+ densities, temperatures, and velocity distributions in the plasma, which are rescaled at each EDGE2D time step to match the total neutral source flux (recycling, recombination, gas injection). In the recycling process, atoms and molecules are re-emitted to the plasma according to the surface reflection data obtained from the TRIM database [162]. The erosion rates for impurities are obtained using the Eckstein yields [163]. The atomic and molecular processes are calculated using the ADAS, AMJUEL and HYDHEL databases [61, 72, 73, 164]. To provide particle exhaust from the computational domain, balancing the gas injection rate, pumping surfaces are located in front of the divertor corners at the entrance to the sub-divertor region. These surfaces pump neutral particles out of the computational domain with an albedo of 0.94. The sub-divertor region is not simulated in this doctoral thesis, as the sub-divertor model was reintroduced at the time of completion of this doctoral thesis.

The set of neutral processes included in the simulations is the one presented by Kotov et al. in [68]. This includes all the reactions listed in the Tables 2.2 and 2.3, except the dissociative attachment (reaction 10) and charge exchange recombination (reaction 6). The older EDGE2D-NIMBUS-like neutral processes setup within EIRENE was used in the Publication V and Publication VI [46]. The NIMBUS-like model treats

the molecular processes without a collisional-radiative model, combines reactions 9 and 15 to an effective reaction skipping production of D_2^+, and neglects molecular elastic collisions (reaction 11), ion conversion (reaction 12), and dissociative recombination (reaction 13). In [68, 91 – 95], the molecular elastic collisions have been found essential for reducing the divertor electron temperatures to sufficiently low values to provide sufficient volume recombination rates for a significant divertor particle flux reduction in detachment.

2.5 Radiative divertor studies in tokamaks

2.5.1 Experiments

For ITER to operate at $Q_{\mathrm{DT}} = 10$, it is predicted that high radiative power fractions of up to 70 – 80% are required to reach partial detachment, while operating at $H_{98(y,2)} \sim 1$, $\beta_N \sim 1.8$, $f_{\mathrm{GW}} \sim 0.85$, and $Z_{\mathrm{eff}} \sim 1.6$. f_{GW} is the fraction of operation density to the Greenwald density limit (Eq. 1.6). Furthermore, DEMO sized reactors are predicted to require close of 100% radiative power exhaust [17]. Any solution to the PFM heat load issue must be compatible with these requirements. Due to these reasons, injection of extrinsic radiating impurities to increase the radiated power fraction to the levels considered necessary in ITER have been widely studied in tokamaks [59, 97, 113, 120, 146, 157, 165 – 193, and references therein]. Conventionally, radiating impurities in radiative divertor studies are nitrogen, neon, argon, and krypton [113, and references therein]. Carbon radiation is also considered in many radiative divertor studies due to the wide usage of carbon PFMs in tokamaks over the past few decades (section 1.2.3).

To achieve the plasma performance requirements, the impurity seeding cannot impact the plasma energy confinement too adversely or increase the plasma Z_{eff} above acceptable values. The effect of impurity seeding on energy confinement shows a very rich phenomenology [59, 173, 181, 190, 192, 194, and references therein]. Injection of extrinsic impurities has a long history in tokamak research [176, 177]. Originally, the main motivation was to study improved plasma confinement with low-Z impurity injection. Edge cooling due to increased radiation was also reported and suggested as a possible solution to the heat flux issue in reactor scale de-

vices [177, 178]. Confinement improvement with impurity injection was observed in AUG [195], DIII-D [196], and JT-60U [197]. This improved confinement regime was not fully reproduced in JET in low collisionality conditions [173, 174, 181, 198], and interest in confinement improvement with impurities subdued [58].

In both JET and AUG, the plasma energy confinement was affected by the presence of a metal wall and the requirement of increased gas fuelling to avoid tungsten contamination of the core plasma [194]. In JET with the ILW, the high triangularity baseline H-mode scenario was affected the most [182, 194]. The benefit of high shaping to give good confinement at high Greenwald fractions [199] was also lost in JET after the installation of ILW. In AUG with a full tungsten wall, confinement at $H_{98} \sim 1$ was achieved in high triangularity baseline plasmas at elevated normalized plasma pressure $\beta_N > 2$ [194]. The confinement lost relative to the carbon PFM devices was observed to be largely recovered by nitrogen seeding in both devices [182, 194, 200]. Furthermore, it was observed that the high triangularity shape, found beneficial for confinement at high densities in JET-C [199], was also essential in JET-ILW to obtain a strong pedestal performance increase with nitrogen seeding [157]. The confinement increase observed with nitrogen injection was not reproduced in similar experiments at JET with neon injection [193]. Interestingly, the original confinement improvement studies in 1984 – 1985 with impurity seeding were conducted with neon [176, 177]. However, the plasma scenarios in those early experiments were quite far from the more recent high performance plasma scenarios at JET, and the physics phenomenologies responsible for the confinement increase with different impurities and plasma scenarios might be different as well.

As expected, the characteristic electron temperature range of the radiating impurities increases with the atomic number of the species. As a result, carbon and nitrogen have been observed to be very good divertor radiators in present day devices as they radiate preferentially in $T_e \sim$ 10 – 30 eV [113, 168, 181, 188, and references therein] and also Publications I – IV. On the other hand, neon is measured to increase radiated power both in the divertor and in the plasma inside the separatrix [168, 183, 181, 192, 193, and references therein] and also Publication IV. Argon is foreseen as the leading candidate seeding gas for DEMO if simultaneous increase in divertor and main plasma radiation is required [113, and references therein]. Krypton radiates mainly inside the separatrix

and provides a good radiative efficiency in mantle with a modest impact on fuel dilution [113, and references therein].

In the early high radiative high performance scenarios in JET, AUG, and DIII-D with the carbon PFMs, the impurity content in the high radiative plasmas was significantly higher than the ITER reference values [120, 195, 201, and references therein]. However, as pointed out by Matthews et al. [202], without a suitable scaling law, direct comparison of Z_{eff} between current machines and ITER are meaningless. By noting that Z_{eff} and total radiated power P_{RAD} (MW) are connected, a multi machine scaling of experimental data and data from code simulations is conducted providing

$$P_{\text{RAD}} = \frac{1}{7}(Z_{\text{eff}} - 1)S\bar{n_e}^2 \tag{2.12}$$

where S (m^2) is the surface area of the plasma (m^2), and $\bar{n_e}$ (10^{20} m^{-3}) [202]. Using ITER parameters, this expression predicted Z_{eff} not too far above the required values in ITER [120]. The linear dependence on the plasma surface area suggests a size scaling as R^2. The explicit dependence of Z_{eff} on the heating power is not included in this scaling. Devynck et al. [203] showed that this scaling gives relatively good predictions in high density operation close to detachment and during impurity seeding in JET-ILW Ohmic, L-, and H-mode plasmas. The main experimental conditions for the multi-machine scaling to be close to the data was that the radiated power in the divertor chamber was significantly larger than the radiated power in the bulk, as is foreseen necessary in ITER. It was concluded that the slope of the original multi-machine scaling [202] characterizes mostly impurities radiating in the divertor at low temperatures [203]. However, deviations between the scaling and measured radiated power of the order of a factor of 2 have been observed in AUG, JET and Alcator C-Mod [204]. These deviations are associated with changing plasma impurity composition and balance between the divertor and main plasma radiation [203]. Recently, attempts to obtain a divertor radiation scaling in H-mode plasma operation in metal devices were published by Kallenbach et al. [204]. For H-mode plasmas in AUG, JET and Alcator C-Mod with nitrogen seeding, the divertor radiation was observed to scale as

$$P_{\text{RAD, DIV, N}} = 72 p_{0,\text{DIV}}^{0.6}(Z_{\text{eff}} - 1)^{0.43} R^{1.5} \lambda_q^{0.64} \text{ (MW), (Pa), (m), (m)} \tag{2.13}$$

where $p_{0,\text{DIV}}$ is the neutral pressure measured in the divertor PFM region. Estimates of the scaling of the divertor radiation are uncertain due to substantial deviations of the radiative potential from the coronal equilibrium

values as well as due to various atomic physics effects that contribute in high density, low temperature divertor operation. This divertor radiation scaling was compared to L-mode plasma simulations of low density, nitrogen seeded JET-ILW and AUG plasmas, and a good similarity to (Eq. 2.13) was obtained [205].

2.5.2 Simulations

To address the need to design divertor components and to predict divertor operational scenarios in next step devices, numerical and analytical radiative divertor simulations have been widely studies in both existing tokamaks and for next step tokamak reactors [90, 111, 205 – 214, and references therein] and also Publications I – IV. For recent studies, see for example Kukushkin and Pacher et al. for ITER [90, 208, 209, and references therein], Reimold and AhoMantila et al. for AUG [111, 205, and references therein], Porter et al. for DIII-D [210, and references therein], Asakura and Hoshino et al. for JT60-U [211, 212, and references therein], and Jaervinen and AhoMantila et al. for JET [205, and references therein] and Publications I – IV. The simulations generally reproduce the experimentally observed trend that the dominant radiating region of impurities shifts towards higher electron temperatures with increasing atomic number of the impurity species. With nitrogen seeding, at low nitrogen radiation levels in low to high recycling condition, the dominant nitrogen radiation region, $T_e \sim 10 - 30$ eV, is located in the divertor chamber close to the divertor targets [205, 102] and also Publication III. With detachment, the dominant radiation region with nitrogen shifts towards the X-point, as the divertor leg temperatures are reduced down to values ($T_e < 5$ eV) below the preferred radiation region for nitrogen, as is recently documented by Reimold and AhoMantila et al. for AUG, and Jaervinen et al. for JET [102, 111, 205] and Publications I – IV. In simulations that represent partially detached LFS divertor conditions in JET H-mode plasmas, stable nitrogen radiation zones are obtained at the LFS X-point in the common SOL (Publications I – IV). Increasing the nitrogen seeding further to reach complete LFS detachment, the nitrogen radiation zone is observed to shift inside the separatrix to form a strong X-point radiation condensation with MARFE-like [96] radiation-condensation features. These regimes are experimentally observed in both JET and AUG, and marginally stable plasma simulations with the SOLPS5.0 code package have been obtained in this regime [54, 97, 111,

and references therein]. In these strong X-point radiation regimes, reduction of the LFS-MP plasma pressure in the SOL is predicted, associated with reduction in P_{SOL} caused by strong radiation inside the separatrix [111]. As a result, a large part of the divertor pressure reduction in these completely detached plasma scenarios is associated with global reduction in the SOL plasma pressure, instead of local pressure gradient formation in the divertor [111]. On the other hand, in the slightly lower radiated power fraction plasmas in JET H-modes with nitrogen radiation in the common SOL, the dominant divertor target pressure reduction is associated with conventional neutral friction in the divertor leg and formation of plasma pressure gradient along the field lines in the divertor (Publications II – III). Therefore, multiple detachment regimes are likely to exist, and the hierarchy of physics processes responsible of pressure and particle flux detachment in these regimes are likely to differ from each other as well. With increasing atomic number of the seeded impurities, increase in the radiation inside the separatrix relative to the radiation in the divertor is observed in the simulations, similar to experimental observations [209] and Publication IV.

Despite the fact that the simulations can qualitatively capture the radiation distributions and divertor detachment characteristics in plasma scenarios with impurity seeding, significant discrepancies between the simulations and the experimental observations do exist [54, and references therein]. These include the underprediction of neutral pressures in the divertor, radiation due to the fuel species, LFS to HFS divertor asymmetries, and not being able to predict the measured plasma flows in the main SOL [54, 95, 111, 205, 215, 216] and Publications I – IV. Due to these reasons, these code packages do not yet offer a quantitative predictive capability for the next step devices [54]. The largest discrepancies are observed in high recycling and partially detached divertor conditions, which are the most interesting operational regimes for ITER divertor [54, and references therein]. The simulation codes usually can reach a fairly good agreement with experiments in low density, attached conditions [54, and references therein].

Predictions of radiative divertor operation for ITER and DEMO have been widely conducted [90, 209, 211, and references therein]. For ITER, the foreseen solution is to use neon injection to provide a radiating, low charge state impurity for the plasma with operation of full tungsten divertor PFMs [209]. Nitrogen injection is deemed an unfavorable solution

due to the technical difficulties related to chemical reactivity of nitrogen and ammonia formation with tritium [217, 218, and references therein]. However, the acceptability of nitrogen injection for ITER depends on the amount and type of nitrogen compounds formed and the technical implications associated to this, both of which remain still open topics of research and development. In the forthcoming DT-campaign in JET, nitrogen injection is deemed unacceptable due to formation of uranium-nitrides in the uranium beds used in the active gas handling system in JET [219, 220]. The formation of uranium-nitrides significantly reduces the hydrogen gas storage capability of the uranium beds. In [209, and references therein] ITER simulations with full tungsten divertor PFMs and beryllium main chamber PFMs in carbon-free environment with nitrogen and neon injection were conducted with the SOLPS code. Generally, it was found that the operational window with neon injection was smaller than the operation window with nitrogen, due to increase of radiation inside the separatrix with neon seeding and the proximity of ITER to its LH-transition threshold. These findings are qualitatively consistent with experimental observation and simulations conducted in H-mode plasmas in JET [193, and reference therein] and also Publication IV.

3. Tungsten concentration control in tokamaks

3.1 Experimental observations

Tungsten is a very strong radiator in the plasma temperatures relevant for the confined plasma in fusion reactors. Therefore, to avoid unacceptably high levels of radiative power losses in reactors operating with tungsten PFMs, the central concentration of tungsten must be kept at or below 10^{-5} [43]. Experiments at AUG with full tungsten PFM coverage as well as in JET-ILW have indeed demonstrated the need to control sources and transport of tungsten to obtain stationary high performance H-mode plasmas [39, 221, and references therein]. Without adequate control, for example, by increasing the ELM frequency with D_2-injection and/or using central heating to maintain the sawtooth activity in the core, tungsten accumulation leads to radiation peaking in the central plasma, disappearance of the sawtooth activity in the central plasma, hollow temperature profiles and disruption of the discharge [157, 222, and references therein]. The tungsten contamination levels can be controlled by the following methods or physics principles:

- Source of tungsten.
- Retention of eroded tungsten in the divertor chamber.
- Screening of tungsten by the SOL plasma.
- Transport of tungsten in the pedestal and edge plasma.
- Flushing of tungsten by ELMs.

- Core transport of tungsten.

Disregarding macroscopic loss of PFM (e.g., melting of the surface layers, evaporation, and arcing [223]), the source of tungsten is determined by physical sputtering, caused by elastic energy transfer from incident particles to the target atoms [39, 163]. The sputtering threshold energy for light projectiles on a substrate consisting of high atomic number species is determined by the momentum and energy conservation in an elastic collision and the surface binding energy of the substrate material [39, and references therein]. Due to the high surface binding energy of tungsten (8.8 eV) and projectile to substrate mass-ratio, the sputtering threshold energies of tungsten for H, D, and T bombardment are about 450 eV, 210 eV, and 140 eV, respectively [31, 163]. Therefore, the erosion of tungsten by the fuel ions can be practically eliminated, by operating in high recycling and partially detached plasmas conditions. The erosion occurs mainly due to intrinsic impurity ions due to their higher mass and electric charge. The electric charge of the sputtering species is critical due to the formation of the sheath-potential drop ($\sim -3T_e/e$ [31]) in front of the target surface, therefore, accelerating the projectile. Electrons deposit heat to the surface, but do not cause physical sputtering due to the very high mass difference between the PFM atoms and electrons and thereby reduced momentum transfer in the collision. Assuming a Maxwellian ion velocity distribution in front of the target, the ion impact energy towards the surface is approximately given by $2T_i + 3ZT_e$, where Z is the charge state of the impacting ion. The threshold for tungsten sputtering by light impurity species, such as carbon, beryllium, or nitrogen, is observed to be around electron temperatures of about a few eV [40, 224].

In L-mode operation, with nitrogen seeding, tungsten sputtering is first observed to increase in attached conditions [40] due to increased light impurity concentration as well as due to the transition to the high recycling regime with increasing divertor particle fluxes. Tungsten sputtering is observed to roll over when the divertor plasma is cooled below the sputtering threshold for light impurity impact, as well as due to the target particle fluxes being reduced in detachment [40]. However, in H-mode plasmas, in plasmas with detached conditions between ELMs, sputtering due to ELMs still occurs. The heat pulse in an ELM is expected to be sufficiently high to exceed the capability of the divertor plasma to buffer the associated temperature increase in the divertor. In other words, the diver-

tor plasma does not have sufficient heat capacity to prevent the temperature increase, and, as a result, the ELM penetrates through the divertor plasma to the target. This is called an ELM *burn through*. Due to ELMs burning through in ELMy H-mode plasmas, tungsten sputtering is caused even if detachment between ELMs is obtained [40, 182, 224, and references therein]. In these plasmas, ELMs dominate the tungsten source. Gross erosion of tungsten is typically observed both experimentally and in simulations to be about an order of magnitude higher than the net erosion due to strong prompt re-deposition of tungsten ions [40, 224, 225, 235, and references therein] and Publications V and VI. This is due to the large gyro-radius of high-Z impurities compared to their ionization mean-free path, which increases the probability for the ion to promptly redeposit during the first gyro orbit.

In JET and ITER, the dominating tungsten source is expected to be in the divertor, where the tungsten divertor PFMs are used. However, it cannot be ruled out that tungsten might be able to migrate from the divertor to the main chamber, such that the effective tungsten source distribution extends to the main chamber as well. Furthermore, there are tungsten coated neutral beam shine-through protection tiles in the JET main chamber, which can provide a tungsten source due to NBI shine-through. For the divertor retention and SOL screening analysis this is important, since tungsten neutrals originating from the main chamber are significantly more likely to penetrate the confined plasma. This is due to the close proximity of the main chamber sources to the confined plasma, whereas the divertor sources have to transport through the divertor plasma to reach the confined plasma region in the device. However, for simplicity, in the tungsten divertor retention analysis conducted within this thesis (Publications V and VI) tungsten is assumed to originate solely in the divertor. These studies can in future be extended to include the sensitivity of the results for a main chamber tungsten source component. Strachan et al. investigated the impact of NBI shine-through sputtering of tungsten on the JET radiation balance with EDGE2D-EIRENE simulations and concluded that the contamination levels were too low to cause a radiative collapse [236].

Once eroded and ionized, and neglecting prompt re-deposition, the retention of tungsten in the divertor chamber (assuming divertor source) is determined by the plasma transport processes. In the direction across the magnetic field lines, the transport of tungsten is anomalous and is often

treated with effective diffusion (or convection) coefficients in the simulation codes (Publications V and VI). In the direction along the magnetic field lines, tungsten particles are transported classically by collisions with background, tungsten, and other impurity ions, and by background electric fields [31]. The most significant force terms impacting tungsten transport in the divertor are [31, 228]:

- Tungsten pressure gradient.
- Collisional coupling to the background ion flow (friction).
- Force by the background electric field.
- Collisional transport caused by background electron temperature gradient (variation of the collisional mean-free path with T_e).
- The collisional transport caused by background ion temperature gradient.

In a simplified fluid approximation these can be written in this order as

$$F_Z = -\frac{1}{n_Z}\frac{dp_Z}{ds} + m_Z\frac{(v_i - v_Z)}{\tau_s} + ZeE + \alpha_e\frac{dkT_e}{ds} + \beta_i\frac{dkT_i}{ds} \tag{3.1}$$

where n_z is the tungsten density, p_z the tungsten pressure, s the distance parallel magnetic field, m_z the mass of tungsten, v_i the background flow velocity, v_Z the velocity of tungsten particles, τ_s the Spitzer stopping time [229], which represents the collisional coupling efficiency between the main and impurity ions, and α_e and β_i are coefficients for electron and ion temperature gradient forces, which are also determined by Coulomb collisions. Typically, the frictional coupling to the background flow and the ion temperature gradient force are the dominating forces determining the force balance along the magnetic field line and the retention of tungsten in the divertor. The frictional coupling typically points towards the target as the plasma gradually accelerates towards sound speed at the sheath entrance. The ion temperature gradient force, on the other hand, points away from the divertor chamber [230].

Tungsten flux at the separatrix is determined by the source distribution, divertor and SOL screening and retention properties. The tungsten concentration in the central plasma is then determined by the transport properties and ELM flushing in the pedestal and central plasma. In this

doctoral thesis, the source and SOL retention properties for tungsten are studied. Other mechanisms inside the separatrix are not studied either experimentally or numerically. Investigations on the tungsten transport properties and control inside the separatrix can be found in [157, 231, and references therein]. The main findings in the latter studies are

1. Inside the centre of the plasma ($r/a < 0.40.5$) tungsten transport is predicted to be governed by neoclassical transport.

2. Outside $r/a \sim 0.5$, turbulent transport dominates over the neo-classical contribution.

3. Density peaking in the central plasma increases the inward neo-classical pinch of tungsten.

4. By increasing the central heating by ICRH, the turbulent outward diffusion and sawtooth activity can be maintained and increased, such that the inward neo-classical pinch is balanced and stable discharges are possible.

Furthermore, frequent ELMs are observed to be beneficial in terms of flushing tungsten out from the pedestal region into the SOL [232].

3.2 DIVIMP

DIVIMP [47] is a trace-ion Monte Carlo code used mainly for assessing the divertor retention of impurities. DIVIMP computes trajectories of the impurity particles in a static plasma background (n_e, n_i, T_e, T_i, $v_{\parallel,i}$, $E_\parallel$). In the parallel magnetic field direction, DIVIMP solves the 1D fluid momentum equation for the impurity test particle, which contains the five force terms described in the previous section (see also [31] chapter 6.5.3, and [228]). DIVIMP also offers a possibility to use a more complete drift-kinetic treatment for the parallel momentum equation for impurities [233]. The latter provides more sophisticated treatment of ion temperature gradient and friction forces, especially in the case of large relative velocities between the fuel and impurity ions. However, in practice the two methods provide nearly identical results, at least in the work conducted in this doctoral thesis (Publications V and VI). In the radial direction, simi-

lar to EDGE2D, DIVIMP assumes cross-field diffusion with the diffusion coefficient given as an input to the simulation. The tungsten source distribution in the simulations in this doctoral thesis is given by sputtering calculated using Eckstein yields [163], and assuming 1% light impurity concentration in the plasma, represented by C^{4+} in the simulations. The ionization and recombination of the test particles as they travel through the simulation domain are calculated using the ADAS rates [61].

4. Radiative divertor studies in JET high confinement mode plasmas

4.1 Setup of the experiments

This doctoral thesis is based on a series of JET H-mode experiments with both the previous, full-carbon wall (JET-C) and with the ITER-like wall (JET-ILW) in various plasma configurations. A recent review of the principal experimental findings in this series of experiments can be found in [157]. Other published studies based on this series of experiments can be found in [157, 180 – 182, 191, 194, 249 – 251] as well as Publications I – IV.

The focus is on an overlapping series of deuterium-fuelled and nitrogen- and neon-seeded baseline ELMy H-mode plasmas obtained in JET-C and JET-ILW configurations with 15 – 25 MW of input power at plasma current of 2.5 MA and at toroidal magnetic field at the magnetic axis of 2.7 T [157, 193, and references therein]. The estimated power crossing the separatrix, P_{SOL}, in most of these plasmas, excluding the few high powered plasmas with $P_{\mathrm{HEAT}} \sim 25$ MW, were around 8 – 11 MW [181, 182, 157, 193, and reference therein]. In the simulations conducted in this thesis, the input power is set to 8 MW, representing the lower end of the estimated range of P_{SOL} as discussed in the Publication I. The plasmas investigated in this thesis were operated in a high-triangularity configuration with the low-field side (LFS) strike point either on the horizontal plate (JET tile number 5, horizontal configuration; high-δ/HT) or on the vertical plate (JET tile number 7, vertical configuration; high-δ/HT) (Fig. 4.1). The high triangularity configuration has been generally observed to enhance the confinement properties of H-mode tokamak plasmas, especially at high densities [199, 244, 245, and references therein]. These high-triangularity configurations were chosen for these plasma scenarios aiming to optimize

the plasma performance with integrated radiative divertor operation. The main diagnostics used to diagnose these plasmas are illustrated in Fig. 4.1. Deuterium was injected at the high-field side (HFS) divertor leg into the common SOL, and nitrogen and neon were injected into the LFS divertor leg into a location corresponding to the common SOL in the horizontal configuration and to PFR in the vertical configuration. In each configuration, wall material environment, and with each injected impurity species, consecutively increasing levels of impurity injection were imposed until partially detached to detached conditions were obtained in the LFS divertor leg. Various levels of deuterium fuelling were investigated.

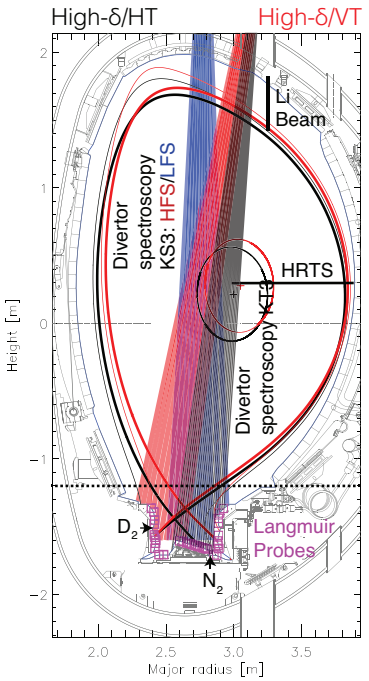

Figure 4.1. 2D poloidal magnetic equilibria of the JET plasmas investigated in this thesis: black (high-triangularity, horizontal target; high-δ / HT), red (high-triangularity, vertical target; high-δ / VT). The main diagnostics used in this study are highlighted: the high resolution Thomson scattering system (HRTS [237], black line at the LFS mid-plane), the Lithium beam system (Li-beam [238], black at the top), target Langmuir probes [239] (Magenta), and divertor visual spectroscopy systems [240, 241] (black, red, and blue). The total radiated power was measured with a multiple-chord bolometer and reconstructed tomographically [242]. A vertical viewing infrared thermography was used to estimate the low-field side power deposition [243]. Deuterium was injected into the chamber at the HFS target, while impurities were seeded at the LFS target. The horizontal dashed line at Z = -1.2 m, represent the spatial location used to separate approximately divertor and main chamber radiations.

4.2 Interpretation of radiative divertor studies in JET high confinement mode plasmas with EDGE2D-EIRENE

Publication III provides the most natural introduction to the radiative divertor studies conducted within this doctoral thesis. The work was presented as an invited talk in the 21st International Conference on Plasma Surface Interactions in May 2014 in Kanazawa in Japan. It concentrates on a nitrogen seeding scan conducted on a medium deuterium injection level of about 2.5 – 2.8e22 e/s in the high-triangularity, horizontal target configuration. Based on an unseeded reference plasma, three nitrogen seeding levels (1.5e22 e/s, 2.5e22 e/s, and 3.5e22 e/s) were investigated producing detached condition in the LFS divertor leg at the highest investigated seeding rate.

Nitrogen seeded JET-ILW H-mode plasmas were investigated with the 2D fluid edge code EDGE2D-EIRENE. The simulation setup and boundary conditions can be found in Publication III. When *imposing the radiation* with impurity seeding, the simulations reproduce the experimentally observed factor-of-10 reduction in the outer target power deposition. This occurs when the divertor radiation normalized by the estimated power crossing the separatrix increases from the unseeded levels of 15% up to the 50% levels required for detachment (Fig. 2 in the Publication III). Consistent with previous experimental measurements in JET-C, nitrogen is predicted to be the dominant radiator at radiation levels required for detachment [246]. At the radiation levels required for onset of detachment, nitrogen provides 85% of the total radiation, with deuterium providing 10% and beryllium the remaining 5% of radiation. Due to the low radiative potential of nitrogen at the electron temperatures above 100 eV, more than 80% of the radiation is predicted to occur in the scrape-off layer, making nitrogen a suitable divertor radiator for typical JET divertor conditions with electron temperatures around 30 eV.

The simulations reproduce the experimentally observed increase in the LFS divertor radiation with nitrogen seeding, and the peaking of the radiation at the LFS X-point with the transition to LFS divertor detachment (Fig. 4.2). However, for the unseeded plasmas the simulations underestimate the divertor radiation and the divertor D_α-emission by a factor of 2 indicating a shortfall in the radiation by fuel species. The peak nitrogen radiation in the simulations follows the 10 – 30 eV electron temperature contour in the divertor leg. Once the LFS divertor detaches, this contour shifts from the LFS divertor leg to next to the LFS X-point, and, as a re-

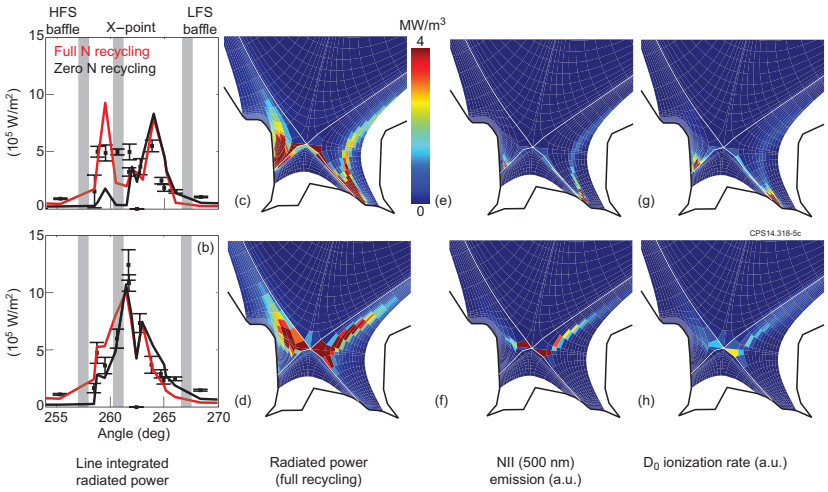

Figure 4.2. Comparison of the simulated divertor channels of the vertical bolometry for attached high recycling (a) and detached (b) conditions. Low-N2 (JET pulse number (JPN) 82554) and high-N2 (JPN 82811) are used for the experimental data. The red lines stand for EDGE2D–EIRENE simulations with full recycling assumption for nitrogen and the black lines for EDGE2D–EIRENE simulations with zero recycling assumption for nitrogen. Simulated 2D radiated power distribution (c and d), 2D NII (500 nm) emission distribution (e and f), and 2D deuterium ionization distribution (g and h) for attached and detached EDGE2D–EIRENE simulations with full recycling assumption. In the radiated power figures, the colorbar spans from 0 (blue) to 4 MW/m3 (red). Arbitrary units are used in the NII emission and D_0 ionization distribution figures.

sult, the peak radiation front shifts from the divertor leg to the X-point as is observed both in the experiment and in the model. In this divertor state, the LFS divertor leg is mainly at electron temperatures below 5 eV, reaching sub-eV temperatures in front of the strike point. As a result, the NII (500 nm) emission, indicative of electron temperatures of 5 – 15 eV in the EDGE2D-EIRENE simulations, shifts from the LFS strike point and divertor leg to the LFS X-point as is observed both in the model and in the experiment (Figs. 4.2 and 4.3). The simulations indicate that the location of the NII (500 nm) emission peak is a good proxy for the poloidal location of the deuterium ionization front (Figs. 4.2 and 4.3). Therefore, the NII emission distribution can be used to extract 2D information about the divertor electron temperatures.

When imposing the measured divertor radiation with impurity seeding, the simulations reproduce the experimentally observed particle flux reduction at the low-field side target without the need for strong recombination (Fig. 4.4). The simulations indicate that this observation is due to both reduced overall deuterium recycling rate, by a factor of 2–3, in

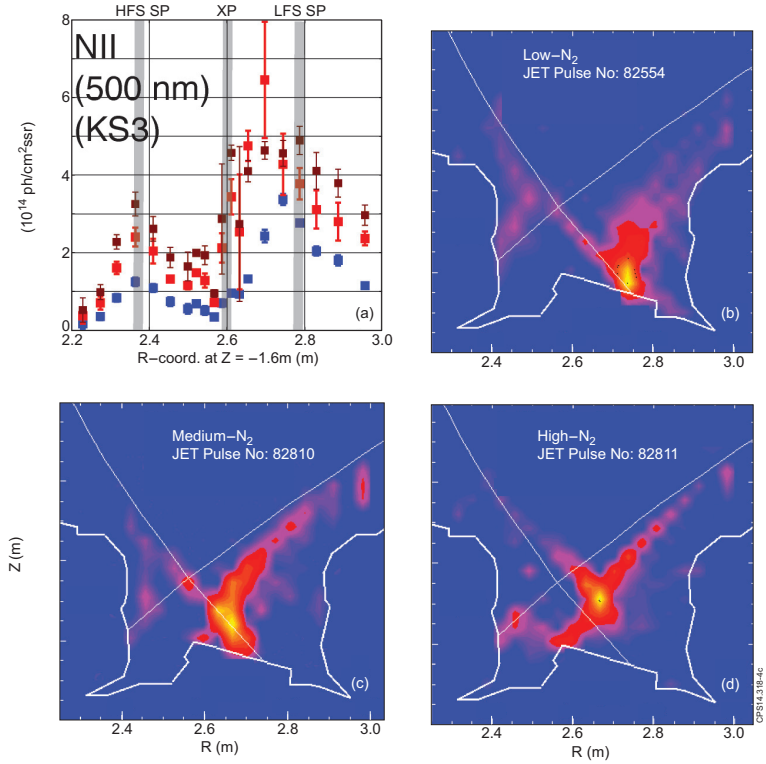

Figure 4.3. Nitrogen NII (500 nm) spectroscopic signals in the divertor. (a) Line-integrated NII emissivities in the divertor as measured by the vertical divertor spectrometer (JET diagnostics system KS3) [240]: blue (low-N_2 / JPN 82554), red (mid-N_2 / JPN 82810), brown (high-N_2 / JPN 82811). The radial locations of the HFS strike point (HFS SP), X-point (XP), and LFS strike point (LFS SP) are illustrated with grey shading. (b – d) 2D reconstructed NII emission in the divertor plasma, based on the divertor endoscope measurements (JET diagnostic system KL11) [247]

the LFS divertor, and due to volume recombination in front of the target. The reduction of the recycling rate can occur due to low power at the deuterium recycling front and is, therefore, strongly linked to the extrinsic impurity radiation. This mechanism is not expected to apply in deuterium fuelling to detachment, since without strong impurity radiation, the main power dissipation mechanisms, deuterium ionization and radiation, is coupled to the recycling process itself. Furthermore, this mechanism requires strong enough momentum losses in the divertor leg, such that the plasma particle flow into the recombination region, as well as the neutral deuterium flow into the ionization region are both slow, as needed for reduced overall recycling rate. As a result, detachment via reduced

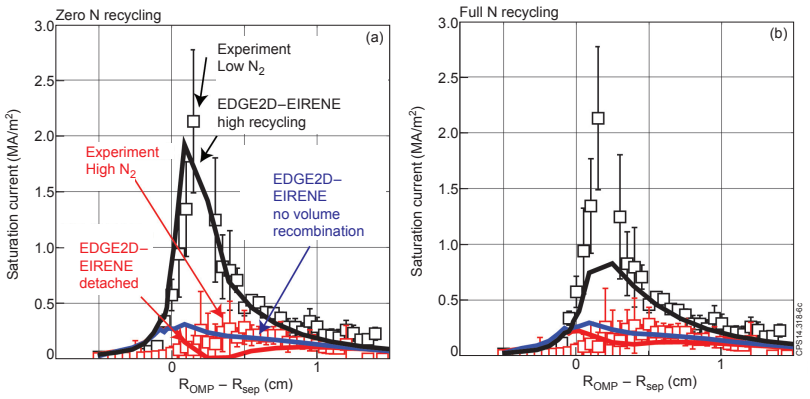

Figure 4.4. Simulated outer divertor ion saturation currents before and after nitrogen induced detachment with zero recycling assumption for nitrogen (a) and with full recycling assumption for nitrogen (b). Black symbols represents plasmas in high recycling conditions (JPN 82554) and the red symbols stands for plasmas in detached conditions (JPN 82811). Blue curves represent EDGE2D–EIRENE simulations without 3-body, and radiative volume recombination processes.

recycling is only possible in the model once there is a sufficient plasma volume or divertor connection length in electron temperatures below 5 eV to allow neutral friction to reduce the plasma pressure in the divertor leg. Therefore, the ionization front tends to be close to the X-point already once low plasma pressures are obtained at the target.

Since nitrogen is chemically active, forming ammonia and molecules with tungsten, the recycling properties of nitrogen are significantly more complicated than those of noble gases [217]. For a pristine ILW, one would expect the nitrogen recycling coefficient to be close to zero due to sticking of nitrogen atoms to the wall. However, since the divertor surface layers in nitrogen seeding operation are expected to reach near-to-equilibrium nitrogen concentration within a few discharges, the effective nitrogen recycling coefficient is predicted to approach unity, at least on the divertor PFMs [190]. To investigate the sensitivity of the model predictions to nitrogen recycling, simulations with recycling coefficients of 0 and 1 (except pumping in the divertor) were considered for nitrogen in Publication III. The reason to conduct the studies only for these two extremes was related to the fact that, only these two options were available in EDGE2D-EIRENE. Generally, the zero recycling assumption changes the nitrogen distribution to be very peaked around the injection valve, which leads to overestimated nitrogen emission levels close to the injection valve rela-

tive to HFS divertor. However, with zero recycling assumption, the simulations captured the increase of the divertor strike point saturation currents in the transition to high recycling conditions with nitrogen seeding. This was attributed to cooling of the plasma in front of the injection valve, which enabled recycling neutrals to pass this region and ionize closer to strike point increasing the recycling levels there.

Summary: *This work was the first series of JET H-mode EDGE2D-EIRENE simulations conducted with the ITER-like wall with impurity seeding. The studies show that by imposing the radiation with impurities, the simulations do reproduce the experimentally observed 2D distributions of total radiated power and NII (500 nm) radiation. Furthermore, by imposing radiation with impurities, the simulations reproduce the experimentally observed particle flux reduction in the LFS detachment. The author also conducted simulations with and without volume recombination to demonstrate that the role of volume recombination in impurity induced divertor detachment may not be as significant as it is in detachment imposed by deuterium fuelling only.*

The simulations did not include cross-field drifts or currents, which is why the focus has been on the LFS divertor. Furthermore, the simulations underestimate the radiation by fuel species by a factor of 2.

4.3 Comparison of H-mode plasmas in JET-ILW and JET-C with and without nitrogen injection

Publication II extended the studies published in Publication III to an overlapping nitrogen seeding scan conducted with the previous full carbon wall of JET.

Since carbon is a strong radiator at divertor electron temperatures of 30 eV in JET, changing from JET-C to JET-ILW was expected to reduce the divertor radiation in JET (Fig. 4.5). Experimentally, about a 30 – 50% reduction in the total and divertor radiated power was observed in both L- and H-mode plasmas [182, 95]. Since the radiative characteristics of nitrogen are very similar to those of carbon, nitrogen injection is expected to provide plasma radiative characteristics in JET-ILW close to those observed in the unseeded JET-C plasmas. This also observed experimentally as well as in EDGE2D-EIRENE simulations [182] and Publication II. Coincidentally, nitrogen seeding was also observed to partially recover the 30 – 40% reduction of H-mode plasma performance that followed the change

from JET-C to JET-ILW, especially in high-triangularity plasmas, indicating a role of low charge state impurities in the formation and performance of H-mode pedestal in JET [182, 194, 251, and references therein].

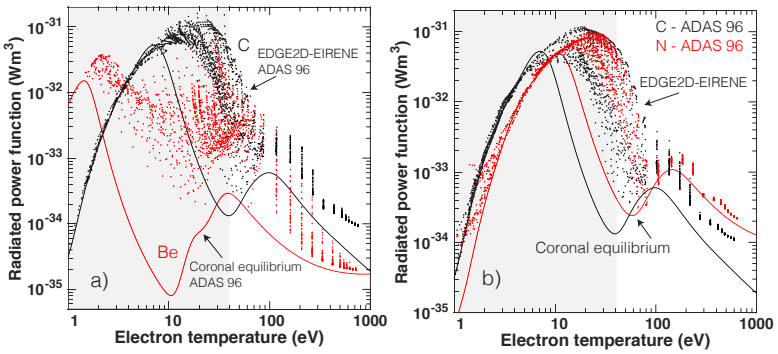

Figure 4.5. Radiated power function of beryllium (a, red), carbon (black), and nitrogen (b, red) as a function of the background electron temperature in coronal equilibrium (solid lines) and as calculated by EDGE2D-EIRENE (dots). The range of typical divertor temperatures ($T_e < 40$ eV) is highlighted with grey shading.

The impact of wall material on the divertor performance of JET H-mode plasma with carbon and ITER-like walls with and without nitrogen seeding was further investigated and simulated with EDGE2D-EIRENE in this doctoral thesis. The impact of wall materials on the divertor plasma characteristics were investigated in three steps with EDGE2D-EIRENE. In the first step, pure deuterium simulations without any impurity contamination were considered to isolate the impact of reduced molecular fraction in the divertor recycling fluxes in JET-ILW relative to JET-C on the divertor plasma characteristics. The reduced molecular fraction is caused by a higher fraction of fast, reflected atoms off the tungsten surface [252]. In the second step, unseeded plasmas were simulated, including beryllium and carbon impurities to investigate the impact of intrinsic impurities on the divertor plasma characteristics. Finally, in the third step, nitrogen seeding was introduced into the simulations to investigate the impact of wall materials on the performance of the divertor with seeded impurities. The same EDGE2D-EIRENE grid was used for all the simulations.

In the pure deuterium simulations, the EDGE2D-EIRENE simulations predict 20 – 100% higher molecular fractions in the divertor recycling fluxes for JET-C when compared to JET-ILW (Fig. 4.6a). This is consistent with previous publications [251 – 254, and references therein]. [253, 254, 255, 256, and references therein]. The simulations show a

log-linear relation between the molecular fraction and the strike point electron temperature at the LFS divertor plate, illustrated in Fig. 4.6a. Consistent with higher deuterium reflectivity and atomic fraction in the divertor recycling fluxes, the energy reflection fraction in the divertor recycling fluxes in JET-ILW is predicted to be about 60 +/- 5%, and in JET-C about 30 +/- 5% (Fig. 4.6b). The total energy reflection fraction shows only a weak dependence on the divertor plasma regime in the simulations. As a result of the higher molecular fraction in the divertor recycling fluxes, the molecular density relative to the total neutral deuterium density in the divertor chamber is predicted to be 20 – 100% higher in JET-C than in JET-ILW (Fig. 4.6c).

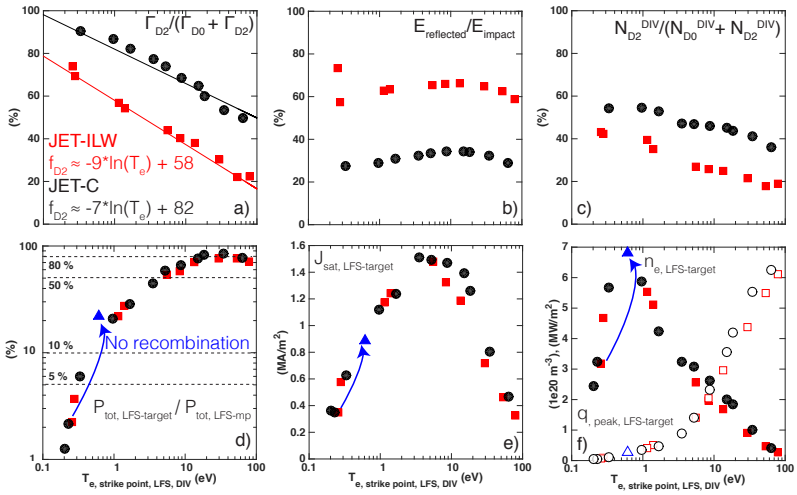

Figure 4.6. Ion fraction of the total divertor recycling flux re-emitted as molecules (a), the fraction of the impinging energy reflected on the divertor targets (b), the ratio of the total molecular neutral deuterium density to the total neutral deuterium density in the divertor (c), the simulated total hydrodynamic pressure-ratio between the LFS target and the LFS mid-plane (d), the simulated LFS divertor peak saturation current, $J_{\text{sat, LFS-target}}$, (e), and the simulated LFS strike point electron density, n_e, LFS-target, (solid symbols) and peak heat flux, $q_{\text{peak, LFS-target}}$, (open symbols) (f) as a function of the strike point electron temperature at the LFS target plate. The red squares represent pure deuterium simulations with the JET-ILW configuration and the black symbols simulations with the JET-C configuration. The blue triangles in figures d – f represent the JET-ILW simulations at the highest obtained separatrix density without 3-body and radiative volume recombination processes. A log-linear relation between the molecular fraction in the divertor recycling and the peak electron temperature at the LFS divertor plate is observed and illustrated with the corresponding equations and trend-lines in the figure (a). The dashed lines in the figure (d) illustrate the 80%, 50%, 10% and 5% pressure-ratio levels.

Since divertor detachment modelling indicates that elastic collisions between deuterium molecules and ions are typically observed to be one of

the dominant momentum loss mechanism [68, 91 – 95], it is expected that the reduced molecular fraction in the divertor plasma would adversely impact the formation of the neutral friction zone in JET-ILW relative to JET-C. However, the total pressure ratio between the LFS divertor target and the LFS mid-plane does not change for a given strike point electron temperature (Fig. 4.6d). Therefore, the simulations indicate that, as long as the peak electron temperature at the LFS plate is given, the pressure reduction between the LFS mid-plane and the LFS divertor plate does not change, even though the molecular density in the divertor plasma does. Hence, the impact of the wall material on the divertor pressure loss in the simulations is implicit via reduction of the peak target electron temperature for a given set of machine control parameters, such as plasma density, input power, or impurity seeding rate. The peak saturation current in the simulations rolls over at about $T_e \sim 4 - 6$ eV, when the peak divertor pressure is predicted to be reduced relative to the upstream pressure (Fig. 4.6e). The peak electron density, on the other hand, continues to increase with reducing divertor temperature until $T_e \sim 0.5$ eV is reached, at which point strong volume recombination in front of the strike point enables reduction of the plate electron density (Fig. 4.6f).

Consistent with the experimental observations, a factor of 2 – 3 reduction in the radiated power in the divertor chamber is predicted with the change from JET-C to JET-ILW (Fig. 4.7a). Deuterium radiation is predicted to increase by 10 – 20% for a given upstream density when changing from JET-C to JET-ILW, whereas radiation by intrinsic impurities is reduced by up to 90%. This is due to a factor of 3 – 6 lower effective, total, non-coronal radiative potential of beryllium when compared to carbon in the simulations (Fig. 4.5). As a result, in the unseeded JET-ILW plasmas, deuterium provides about 90% of the divertor radiation, while in the unseeded JET-C simulations, deuterium contributes 40% to the total divertor radiation with carbon providing the remaining 60% in the base case simulations with a factor of 2 enhancement of the chemical sputtering yield. If the chemical sputtering yield of carbon is enhanced by a factor of 30 to reproduce the experimentally observed divertor radiation values, more than 90% of the total radiation is provided by carbon (Figs. 4.7a and b). However, these simulations overestimate the experimentally measured LFS divertor CIII (465 nm) emissions by a factor of 2 – 3 indicating that the carbon content in the divertor plasma is overestimated, therefore, compensating a short fall of radiated power by deuterium in the

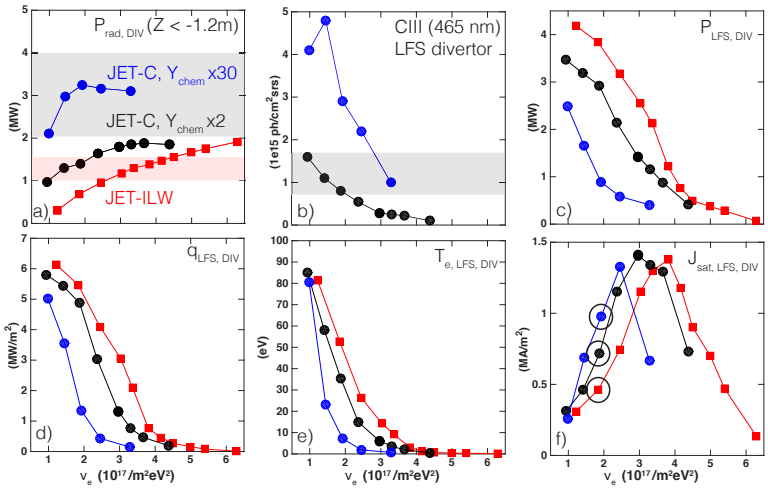

Figure 4.7. Simulated radiated power in the divertor chamber (Z < -1.2 m) (a), the simulated CIII (465 nm) emission in the LFS divertor leg (b), the simulated LFS plate power deposition (c), the simulated LFS plate peak power flux (d), the simulated LFS plate strike point electron temperature (e), and the simulated LFS plate peak saturation current (f), as a function of the LFS mid-plane electron collisionality ($n_e L/T_e^2$). The connection length is assumed to be 40 m. The grey and red shading in the figure (a) represent the range of the experimentally measured values. The grey shading in the figure (b) represents the experimentally measured values with the JET divertor spectrometer (KS3 [240]). The red symbols stand for JET-ILW simulations, the black symbols for the JET-C simulations with the chemical sputtering yield multiplied by a factor of 2 and the blue symbols for the JET-C simulations with the chemical sputtering yield multiplied by a factor of 30. The simulation cases further illustrated in figure 4.6 below are circled in figure f.

simulations (Fig. 4.7b). Similar findings were documented by Groth et al. for JET-C and AUG [257].

The electron cooling potential due to radiation in the simulations, including the transport induced enhancement over the coronal levels, indicate that, as expected, the peak beryllium radiation occurs at around electron temperatures about 2 – 3 eV, whereas the peak carbon radiation occurs at around 10 – 30 eV (Fig. 4.5). Furthermore, it is observed that carbon can reach a factor of 2 – 3 higher peak radiative losses than beryllium in the simulations. Comparison to coronal equilibrium values indicate that the transport induced non-coronal effects in EDGE2D-EIRENE increase the effective radiative losses of beryllium by 2 – 3 orders of magnitude in the electron temperatures of 5 – 30 eV. 1 – 2 orders of magnitude enhancement is observed for carbon in the electron temperature range of 20 – 50 eV.

Consistent with the previous studies in L-mode plasmas, due to the

reduced radiation levels in JET-ILW compared to JET-C, as well as due to the reduced power dissipation by molecular interaction, the predicted outer divertor peak power and total power deposition is increased by 25 – 50% for a given LFS mid-plane electron collisionality (Figs. 4.7c and d) [95]. When comparing to the JET-C simulations with the chemical sputtering enhanced by a factor of 30, the predicted divertor power deposition is higher in JET-ILW by a factor of 2 – 4. Consistently, the experimental measurements indicate 20 – 50% lower LFS power deposition values in JET-C than in JET-ILW. In JET-C, the experimental measurements indicate LFS divertor power deposition values about 1.5 – 3.5 MW, reducing with increasing deuterium fuelling [181]. As a result of the lower power deposition at the LFS divertor plate, up to a factor of 4 lower LFS divertor peak electron temperature is predicted for JET-C relative to JET-ILW for a given LFS mid-plane electron collisionality; this prediction is consistent with the experimental data (within its scatter) (Fig. 4.7e). Therefore, the LFS detachment threshold in electron collisionality is predicted to be only about 10 – 20% lower in JET-C than in JET-ILW, depending on the assumption on the carbon chemical sputtering rate (Fig. 4.7f).

Nitrogen is observed to reproduce the radiative properties close to those of carbon in the simulations (Fig. 4.5). As expected, the peak radiative losses of carbon and nitrogen occurs at 10 – 30 eV, when including the transport-induced enhancement over the coronal equilibrium values, as given by EDGE2D-EIRENE. The peak radiative potential of nitrogen with the ADAS 96 dataset is about 10% lower than that of carbon. Comparison to coronal equilibrium values indicate that the transport induced equilibrium effects in EDGE2D-EIRENE increase the effective radiative potential of nitrogen and carbon by 1 – 2 orders of magnitude in the electron temperatures of 20 – 50 eV. For electron temperatures about 40 – 100 eV, similar radiative potentials are predicted for carbon and nitrogen impurities in the simulations. For electron temperatures above 100 eV, corresponding to the computational domain inside the separatrix, the radiative potential for both impurities are at low levels, therefore yielding less than 20% of the total radiation to occur inside the simulations, as long as the simulations do not enter a radiation-condensation instability (MARFE-like formation) inside the X-point. Due to these reasons, both nitrogen and carbon are good divertor radiators for typical JET divertor conditions with electron temperatures in the range of 30 eV. With increasing nitrogen seeding, nitrogen radiation is predicted to increase in

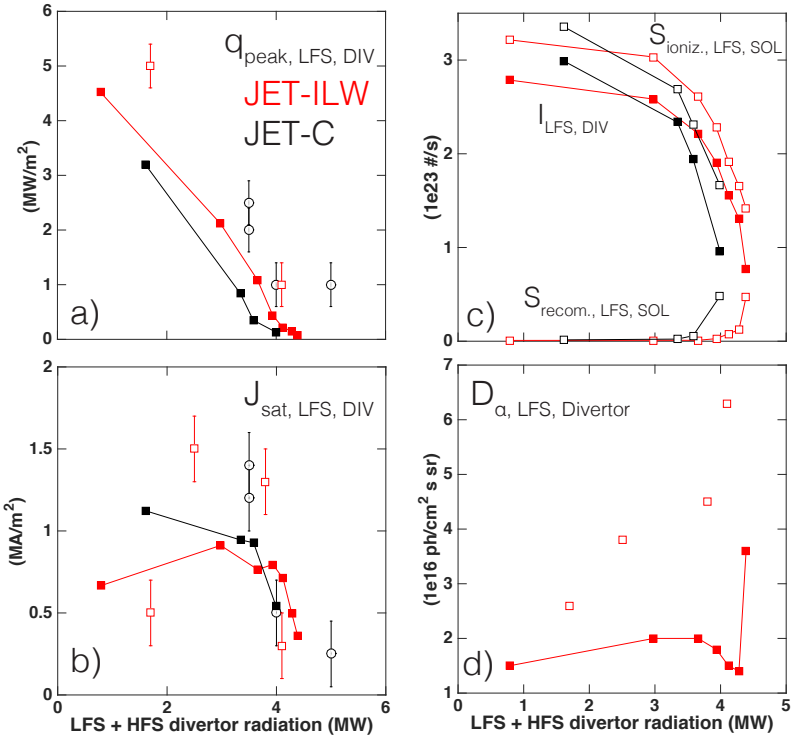

Figure 4.8. LFS divertor target peak heat flux, $q_{\text{peak, LFS}}$, (a) LFS divertor peak saturation current, $J_{\text{sat, peak, LFS}}$, (b) and LFS SOL total ionisation source, $S_{\text{ionization, LFS, SOL}}$ (upper hollow symbols), LFS divertor target particle flux, $I_{\text{DIV, LFS}}$ (solid symbols), and total LFS SOL recombination sink, $S_{\text{recombination, LFS, SOL}}$ (lower hollow symbols) in the seeded JET-ILW (red) and the JET-C (black) simulations, as a function of the total divertor radiated power below Z = -1.2 m. d) Measured and predicted LFS divertor D_α-emission. The hollow red squares and the hollow black circles in figures a and b represent experimental data points in the JET-ILW and JET-C environments, respectively. The red lines represent EDGE2D-EIRENE simulations with the JET-ILW material configuration and the black lines simulations with the JET-C material configuration.

both JET-C and JET-ILW, whereas the radiation due to deuterium and intrinsic impurities are predicted to be reduced. The reduction of deuterium radiation is caused by reduced overall deuterium recycling rate in the simulations with increasing nitrogen seeding, whereas the reduction of beryllium and carbon radiation occurs due to reduced sputtering rate of these impurities.

Similar to experimental observations, the predicted LFS divertor peak heat flux is reduced nearly linearly from the unseeded levels of 3 – 5 MW/m^2 down to levels below 0.5 MW/m^2 with increasing nitrogen seeding. This happens when the divertor radiation levels increase from the unseeded 1 – 2 MW ($\sim$ 15 – 25% of P_{SOL}) levels to the 4 MW ($\sim$ 50%

of P_{SOL}) levels corresponding to detached solutions (Fig. 4.8a). Similar to experimental observations, detachment induced by nitrogen occurs in both JET-C and JET-ILW simulations when the divertor radiated power reaches the levels of about 45 – 50% of the power crossing the separatrix corresponding to divertor radiated power about 3.5 – 4 MW. This is indicated by reduction of the peak and total integral saturation current at the LFS divertor plate (Figs. 4.8b, and c). The peak LFS divertor radiation front is shifted from the divertor leg to the LFS SOL X-point following the onset of strike point detachment in both JET-C and JET-ILW simulations, similar to experimental observations. In these divertor conditions, the LFS divertor leg electron temperatures drop below 5 eV, required for divertor detachment to occur. This also reduces radiative losses of nitrogen and carbon in the divertor leg (Fig. 4.5). As a result, the peak radiation front shifts to the LFS X-point, where the cross-field heat source from the confined region and the shallow magnetic pitch angle enable the SOL plasma to maintain the electron temperatures sufficiently high for impurity radiation. For both the JET-C and JET-ILW simulations, with increasing nitrogen seeding and impurity radiation, the integral LFS divertor particle fluxes roll over due to reduced overall deuterium recycling rate in the divertor leg similar to result published in Publication III (Fig. 4.8c). Therefore, unlike in the simulations without impurities, strong volume recombination is not required for target particle flux reduction. The reduced recycling rate is possible due to strong extrinsic impurity radiation reducing the power flow reaching the deuterium ionization front, thereby, reducing the total deuterium ionization rate. Together with sufficient momentum losses in the low field side divertor leg limiting the plasma flow into the recombining regions, the overall recycling rate is reduced in these simulations. The overall momentum losses in the LFS divertor leg due to neutral interaction in these simulations reach values comparable to the total hydrodynamic pressure of the SOL plasma above the X-point.

The LFS divertor D_α-emissions are underestimated by a factor of 2 in the unseeded JET-ILW plasmas (Fig. 4.8d). With increasing nitrogen seeding, the LFS divertor D_α-emissions is measured to increase reaching maximum values of roughly a factor of 2 – 3 higher than in the unseeded basecase. This is caused by reduction of divertor T_e and increase of the recombination emission of D_α. In contrast, with nitrogen seeding in the simulations, the D_α-emission in the LFS divertor leg increases by about 30%

with increasing nitrogen seeding into a high recycling plasma. In detachment, the D_α-emission is reduced with increasing degree of detachment until a strongly recombining solution is obtained (Fig. 4.8d). A possible explanation for the discrepancy in the detached solutions is underestimated volume recombination in the simulations, therefore, underestimating the recombination D_α-emission. In the strongly recombining solutions in JET-ILW, the predicted D_α-emission in the LFS divertor leg is about a factor of 2 lower than that measured experimentally at the highest nitrogen injection level. For this case, the predicted volume recombination in the LFS divertor leg is roughly equal to the surface recombination. If it is assumed that the recombination D_α-emission is linearly proportional to the recombination magnitude, which is a strong assumption due to the non-linear dependence of D_α-emission on the local densities and temperatures, the simulated recombination rate would be a factor of 2 lower than measured. Therefore, if the recombination rate in the EDGE2D-EIRENE predictions would be a factor of 2 higher, the solution would be dominantly volume recycled. However, even in such conditions, the dominant reduction of the LFS divertor particle flux, compared to the unseeded levels, is caused by reduced deuterium ionization and recycling rate. Therefore, the bulk reduction of the LFS divertor particle fluxes can be achieved even without volume recombination in the simulations, whereas volume recombination is needed in the simulations to reproduce the contribution of volume recombination to the total LFS recycling rate. The latter is presumably significant in the impurity induced detachment in the experiments.

Summary: *This work was the first series of JET H-mode EDGE2D-EIRENE simulations contrasting the operation with the full carbon (JET-C) and ITER-like wall (JET-ILW) materials with and without nitrogen seeding. The simulations included analyses of the impact of deuterium recycling properties on the PFMs, impact of intrinsic SOL radiators, carbon and beryllium, and impact of nitrogen seeding on the divertor performance characteristics in the two wall material configurations. The author conducted a systematic series of pure deuterium simulations without impurities included with the two wall material configurations to isolate and to investigate the impact of deuterium recycling properties on the PFMs on the divertor performance. These simulations indicates that due to the larger molecular contribution in the divertor recycling fluxes, the JET-C plasmas are predicted to have up to a factor of 2 lower peak electron temperature at the*

LFS divertor plate for a given SOL collisionality than the JET-ILW plasmas. The author conducted an overlapping series of unseeded simulations in the JET-C and JET-ILW with carbon and beryllium impurities included to investigate the impact of intrinsic radiators on the divertor performance. As expected, when including the intrinsic SOL radiators, carbon and beryllium, into the simulations, a factor of 2 – 3 reduction of radiated power in the divertor chamber is predicted when changing from JET-C to JET-ILW, consistent with experimental observations. The author conducted an overlapping series of nitrogen seeded simulations in the JET-C and JET-ILW, as well as contrasted the experimental observations of divertor performance in the two wall configurations with nitrogen seeding. It was observed that LFS divertor detachment was obtained at similar divertor radiated power values in the two configurations both in the experimental measurements as well as in the predictions. In the JET-ILW simulations, the missing carbon radiation was compensated by larger nitrogen radiation contribution, such that with nitrogen seeding the two configuration reached detached divertor conditions at similar radiated power values. The simulations did not include cross-field drifts or currents, which is why the focus has been on the LFS divertor. Furthermore, the simulations underestimate the radiation by fuel species and intrinsic impurities. Therefore, forthcoming studies should address whether the nitrogen radiation in these studies compensates over underestimated fuel and intrinsic impurity radiation.

4.4 Impact of divertor geometry on radiative divertor performance in JET H-mode plasmas

Publication I investigates the impact of divertor geometry on the radiative divertor performance in JET H-mode plasmas with nitrogen seeding. This study extends the studies in Publication III from horizontal LFS divertor plate to an overlapping series on vertical LFS divertor plate.

In the unseeded plasmas, the two divertor configurations reach the same main SOL and pedestal electron density and temperature (pedestal only) profiles, as well as peak electron temperature at the LFS divertor plate (about 30 eV) (Figs. 4.9a and b). A factor of 2 higher peak saturation current is measured at the LFS plate in the vertical configuration than in the horizontal configuration (Fig. 4.9c). Furthermore, EDGE2D-EIRENE simulations indicate that this occurs with a lower strike point electron temperature in the vertical configuration, although the divertor probe

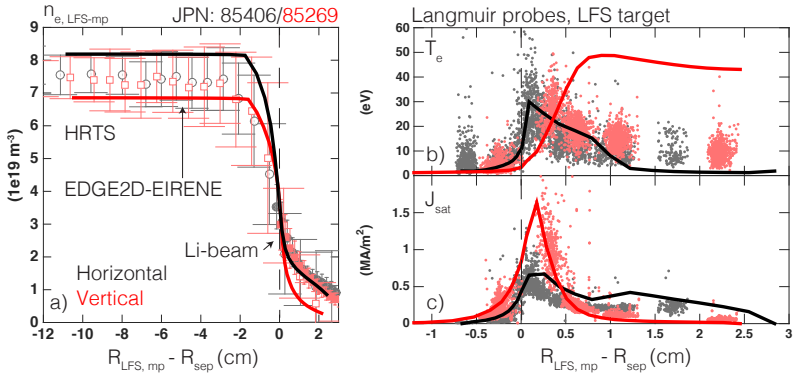

Figure 4.9. Measured and predicted LFS mid-plane electron density (a), LFS target electron temperature (b), and LFS target saturation current (c) profiles in the unseeded plasmas in horizontal (black) and vertical (red) divertor configurations. The measured HRTS profiles are shifted by +1.5 cm (horizontal) and +1 cm (vertical), such that the measured separatrix electron temperature is about 100 eV, which is consistent with assuming conduction-limited SOL in an H-mode plasma in a JET-sized tokamak. The measured Li-beam profiles are shifted by -0.8 cm (horizontal) and -0.5 cm (vertical) to align the separatrix n_e with the HRTS profile. Finally, the Langmuir probe profiles are shifted by +0.5 cm (horizontal) and +0.9 cm (vertical) such that the saturation current peaks in the common SOL.

profiles do not properly resolve the vicinity of the strike point in this plasma. These findings, yet marginally, are inline with the conventional idea that the vertical configuration facilitates recycling towards the separatrix and, therefore, enhances the densities and recycling levels at the strike points, and thus leads to lower temperatures locally. However, since the downstream divertor T_e and J_{sat} evolve proportional to n_e^2, a small change in $n_{e,\,\text{LFS-MP, sep}}$, which is well within the scatter of the experimental data, could produce the same effect.

With the base case boundary conditions and cross-field transport assumptions, assuming the same electron density at the LFS mid-plane separatrix, the EDGE2D-EIRENE simulations reproduce the measured saturation currents and profiles at the LFS divertor target in the two configurations (Fig. 4.9c). As measured experimentally, EDGE2D-EIRENE predicts a factor of 2 – 3 higher LFS strike point saturation currents in the vertical than in the horizontal divertor configuration. As a result, the strike point electron temperature is predicted to be about a factor of 3 lower in vertical than in the horizontal configuration (Fig. 4.9b). However, whereas in the horizontal divertor configuration the model reproduces the measured main SOL density profile, in the vertical configuration the density 0.5 cm away from the separatrix, and further radially away, is un-

derestimated by a factor of 2 (Fig. 4.9a). This is associated with a factor of 2 – 3 overestimated far SOL electron temperatures in the vertical configuration (Fig. 4.9c). The horizontal configuration is able to reach the factor of 2 higher far SOL density relative to the vertical configuration for the same set of transport coefficients due to stronger far SOL ionization source. Whereas in the vertical configuration, as expected, the divertor ionization distribution is strongly localized in front of the strike point, the horizontal configuration leads to recycling towards the far SOL producing significantly broader ionization distribution in front the target, thereby fuelling the far SOL. The concentration of recycling neutrals towards the separatrix in the vertical configuration tends to create flow reversal patterns in the near SOL and high mach flows towards the target in the far SOL, which further reduce the far SOL densities (Chapter 15 in [31] and references therein). The horizontal configuration creates an opposite effect. However, if cross-field drifts dominate the SOL flows, then the ionization driven flows may be less important. Therefore, an open question remains, whether the lack of drifts in the simulations explains the, experimentally not observed, strong differences in the density profiles between configurations. Otherwise, the vertical divertor simulations, as they stand, presumably underestimate either the neutral leakage or the plasma transport into the far SOL.

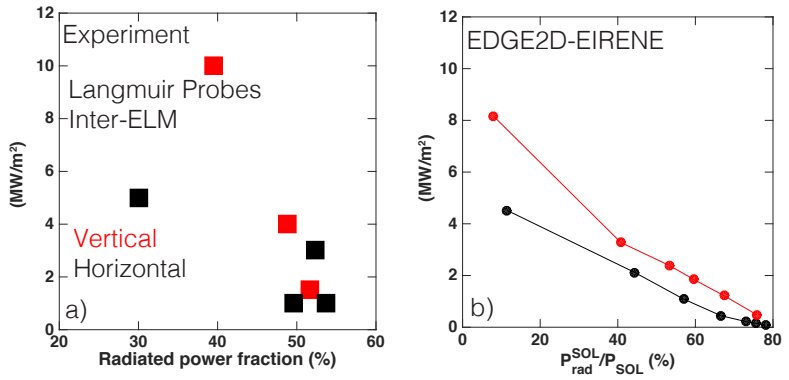

Figure 4.10. a) Measured reduction of the LFS divertor peak heat flux as a function of the radiated power fraction in the investigated plasma. b) Predicted reduction of the LFS divertor peak heat flux as a function of the fraction of power crossing separatrix, PSOL, radiated in the SOL. The EDGE2D-EIRENE catalog folders and JET pulse numbers can be found in the appendix in Publication I.

Within the uncertainty of the experimental data and the range of the simulated EDGE2D-EIRENE cases in this study, the vertical divertor is

not measured or predicted to offer any benefit in terms of minimizing the LFS divertor peak heat flux for a given radiation level imposed by nitrogen (Figs. 4.10a and b). As observed, both vertical and horizontal divertor configurations in this study require a radiative fraction of about 50% to reach LFS divertor heat fluxes less than 2 MW/m^2, which is of the order of the diagnostics resolution of the divertor probes (Fig. 4.10a). Furthermore, the simulations show no benefit in vertical configuration in minimizing the impurity contamination, fuel dilution, and Z_{eff} levels needed for a given radiated power level. Similarly, EDGE2D-EIRENE predicts that fairly similar SOL radiation fractions of 60 – 80% are needed in both configurations to reach LFS divertor peak heat fluxes less than 1 – 2 MW/m^2 (Fig. 4.10b). Whereas in the unseeded plasmas, the divertor radiation is underestimated by a factor 2 in the EDGE2D-EIRENE simulations, by imposing the radiation with nitrogen seeding, the measured radiated power levels and distribution in the divertor can be obtained in both configurations.

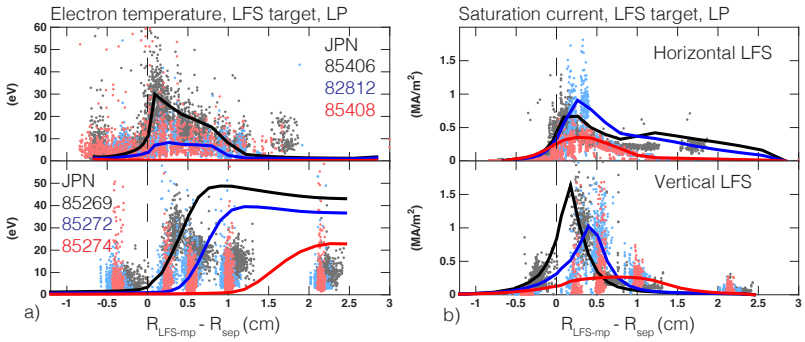

Figure 4.11. Measured (dots) and predicted (lines) LFS target electron temperature (a) and saturation current (b) distributions with increasing levels nitrogen seeding (unseeded/black, mid-N_2/blue, high-N_2/red) for the horizontal (upper row) and vertical (lower row) LFS divertor target configurations.

The measured reduction of the LFS target electron temperatures, heat and particle fluxes in the detachment assisted by nitrogen is captured by the EDGE2D-EIRENE simulations in both configuration when imposing the measured levels of divertor radiation with nitrogen seeding (Fig. 4.11). In the simulations of the horizontal configuration, detachment assisted by nitrogen leads to reduction of the LFS saturation current across the entire profile. On the other hand, in the vertical configuration, the plasma at the strike point detaches at lower impurity radiation levels than the rest of the SOL plasma, and the peak saturation current shifts towards far SOL with increasing degree of detachment (Fig. 4.11).

These observations are also consistent, yet marginally, with the LFS target Langmuir Probe measurements within the uncertainty in the data.

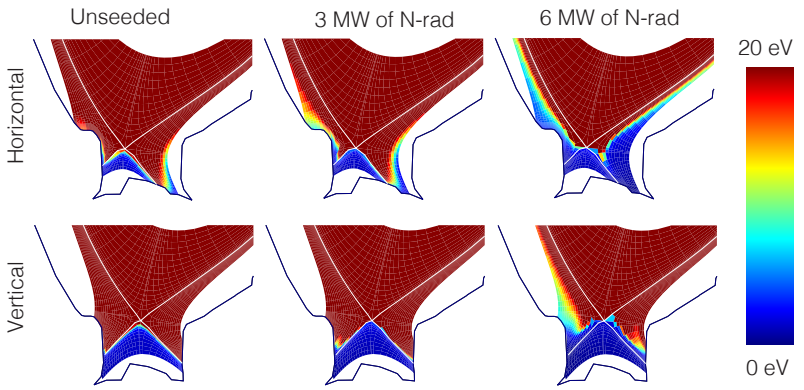

Figure 4.12. Predicted 2D deuterium ionization distribution in the divertor for the EDGE2D-EIRENE solutions compared to the measured bolometer signals in Fig. 4.11

In the simulations of the horizontal LFS divertor configuration, the LFS strike point recycling levels increase at moderate radiation levels and the far SOL recycling levels drop when increasing the nitrogen seeding from the unseeded levels to the medium seeding level (Fig. 4.11b). This is caused by cooling of the far SOL plasma, whereas the strike point temperatures remain still around 10 eV. As a result, the broad ionization distribution in front the horizontal target contracts from the far SOL towards the strike point, where the plasma conditions are still ionizing. This increases the ionization source at the strike point and reduces it in the far SOL resulting in the observed change in the saturation current profile. Increasing the nitrogen seeding further, also the strike point electron temperature collapses to low values below 1 eV, producing completely collapsed target electron temperature profiles. As a result, the ionization front detaches from the strike point and shifts towards the X-point producing a V-shaped 2D ionization profile in the divertor leg, which follows the 5 – 15 eV electron temperature contour (Fig. 4.12). As this occurs, the saturation current profile at the LFS target is reduced uniformly across the profile. In other words, a well-defined, partially detached state, as suggested by Kallenbach et al. [113], does not exist for the horizontal configuration in these simulations. Instead, a gradual, complete, divertor profile detachment follows the high-recycling divertor regime. The lack of partially detached LFS divertor regime in the horizontal configuration might be caused by the combination of outward tilted horizontal JET tile

number 5 and the close proximity of the vertical baffle JET tile number 7. The neutrals recycling from the horizontal tile, on which the strike point is, are preferentially reflected towards the vertical baffle tile, which reflects them back into the far SOL in the LFS divertor. As a result, the far SOL neutral densities and ionization sources are increased in the LFS divertor leg, facilitating detachment of the far SOL at lower main SOL densities, collisionalities and radiative power levels. The outwards tilted and side baffled horizontal divertor configuration was previously found to lead to similar effect in the JET Mark-IIA divertor [125]. However, partially detached horizontal divertor plasmas were achieved in the JET Mark-I divertor, operating without side baffles, with and without impurity seeding [129].

In the vertical configuration, neutral recycling occurs preferentially towards the separatrix and the private flux region. Therefore, the main neutral reservoir in the divertor plasma in the vertical configuration is in the private flux region. In the horizontal configuration both PFR and far SOL provide neutral reservoir for deuterium ionization. As a result, unlike in the horizontal configuration, the divertor ionization is strongly localized close to the separatrix in the vertical configuration in the model, producing strong peak saturation currents close to the strike point in attached conditions in the vertical geometry (Figs. 4.11 and 4.12). However, as documented by Moulton et al. [132], this effect is obtained in the LFS divertor only if the neutrals are reflected back from the PFR floor tiles (tile 5 in JET). If the neutrals are lost in the PFR, the impact of the divertor geometry on the LFS divertor characteristics are strongly reduced [132].

With moderate nitrogen injection, the divertor plasma cools down preferentially along the separatrix in the divertor leg, where the product of electron and nitrogen densities and radiative loss function (T_e) are most favorable for nitrogen radiation (Fig. 4.12). As this happens, the ionizing plasma contour ($T_e > 5$ eV) shifts towards the far SOL, and neutrals penetrate radially further into the divertor leg increasing the saturation current away from the strike point (Fig. 4.12), and producing divertor profiles conventionally associated with partial divertor detachment [113]. The divertor D_α-emission is underestimated by a factor 2 – 5 throughout the nitrogen injection scans, indicating a short-fall in radiation from the fuel species. Whereas in the unseeded cases one could argue that the omission of drifts can partially explain the discrepancy, at least in the HFS diver-

tor, the role of drifts is expected to be less significant for strongly seeded, detached plasmas. Therefore, the omission of drifts is likely not to fully explain the discrepancy. Instead, some D_α-emission channels, significant at low temperature (< 2 eV), high density ($10^{20} - 10^{21}$ m^{-3}) plasmas, might not be taken into account in the EDGE2D-EIRENE post processing routine. Furthermore, due to the strong radiation-temperature-coupling for deuterium at low temperatures, for which the relevant reaction rates become very non-linear, the radiation short-fall with deuterium, might be a consequence of the given fluid model not solving the physics details in the deuterium recycling region properly yet, leading to underestimated deuterium radiated power and D_α-emission.

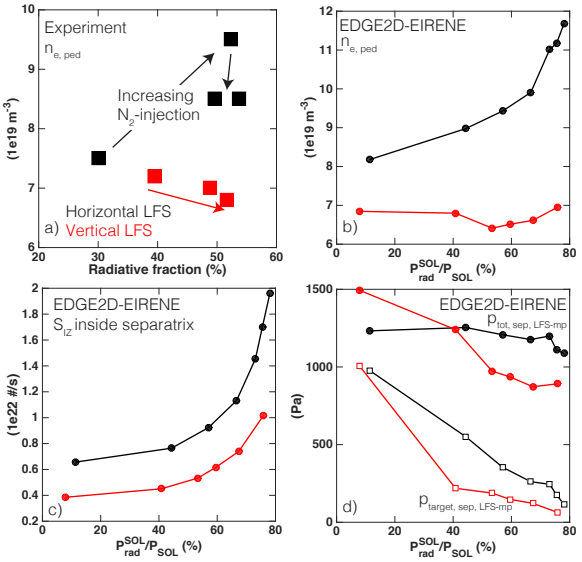

Figure 4.13. Measured (a) and predicted (b) evolution of the pedestal electron density, $n_{e,\,\mathrm{ped}}$, as a function of the radiative power fraction (a) and SOL radiation fraction (b), $P_{\mathrm{rad,SOL}}/P_{\mathrm{SOL}}$. c) Predicted deuterium ionization source inside the separatrix. d) Predicted total pressure at the LFS mid-plane separatrix and at the LFS strike point. Black color is used for the horizontal LFS target cases and red represents the vertical LFS target cases. The arrows within the experimental data points illustrate the trend of the data with increasing nitrogen injection. The radiated power fraction stands for the total measured radiated power in the experiment divided by the total heating power in the experiment. The rational to use different x-axises for the experimental data and for the simulations is related to the difficulties in obtaining accurate experimental estimations for the $P_{\mathrm{rad,\,SOL}}$ and P_{SOL}. For further details the reader is suggested to check the Publication I.

With increasing nitrogen injection rate in the horizontal configuration, a 25% increase of the pedestal electron density is experimentally observed at medium N_2-levels. At higher nitrogen injection levels required for LFS

detachment, about 10% reduction of the pedestal density is observed (Fig. 4.13a) (See also [157]). In contrast, in the vertical configuration, only a few % reduction of pedestal density is observed with increasing nitrogen seeding rate from the unseeded levels to partial LFS detachment. Interestingly, EDGE2D-EIRENE simulations reproduce this behavior qualitatively, such that increasing the nitrogen seeding rate only relative to the unseeded base case, without changing any cross-field transport assumptions, a monotonic 43% increase of pedestal electron density is obtained through the seeding scan in the horizontal configuration. On the other hand, in the vertical configuration, the pedestal electron density remains constant within 6% throughout the seeding scan (Fig. 4.13b). The reduction of the pedestal electron density in the horizontal configurations following the LFS divertor detachment is not observed in the simulations and may be related to increase in the pedestal cross-field transport with LFS detachment or increasing upstream collisionality, not addressed in these simulations.

With increasing nitrogen injection rate, an increase in the pedestal neutral fuelling is observed in both configurations with increasing SOL radiation (Fig. 4.13c). However, in the horizontal configuration this is associated with approximately steady total pressure and electron density at the LFS mid-plane separatrix, such that the pedestal density is increased with increasing pedestal fuelling (Fig. 4.13d). In the vertical configuration, on the other hand, the total pressure and electron density are reduced at the LFS mid-plane separatrix with increasing nitrogen injection such that, despite increasing pedestal fuelling, the pedestal density does not increase in the model. This is caused by detachment of the strike point region in the vertical target simulations at relatively low radiated power, as is illustrated by the strong reduction of total pressure at the strike point at 40% SOL radiation fraction (Fig. 4.13d). As the strike point region detaches, the total pressure in the separatrix field line is reduced in the simulations, even though the power crossing the separatrix remains practically the same. In principle, this mechanism should reproduce the reduction of pedestal density in LFS detachment in the horizontal configuration as well. However, in the simulations, such a strong reduction of LFS mid-plane pressure in LFS detachment, as is observed in the vertical configuration, is not observed in the horizontal configuration.

Unlike the original horizontal and vertical JET divertor geometry studies with the Mark-I divertor [129, and references therein], the divertor

geometries studied in this dissertation do not represent a pure horizontal to vertical divertor comparison. In this study, the HFS divertor strike point is on the vertical plate, JET tile number 3, in both configurations, due to the requirement to maintain a high triangularity plasma shape, which is important for H-mode performance in these discharges. Therefore, in the horizontal LFS divertor geometry, the vertical HFS divertor configuration is expected to have an impact on the pedestal neutral fueling from the HFS side, HFS divertor contribution on the LFS divertor neutral distribution and plasma profiles, as well as on the LFS to HFS divertor asymmetries, thermoelectric currents, drifts and flow patterns in the SOL. To unambiguously disentangle the impact of the HFS divertor configuration on the LFS divertor characteristics, experiments with low triangularity plasma shapes should be conducted with the HFS divertor strike point on both the vertical, JET tile number 3, and the horizontal, JET tile number 4, plates.

Overall, neither the horizontal configuration nor the vertical configuration are predicted to provide any substantial benefit in terms of minimizing divertor surface heat loads or plasma contamination levels for a given radiated power level. Therefore, as the vertical configuration has been observed to provide enhanced divertor performance when compared to horizontal configurations, it can be concluded a vertical configuration is more favorable in reactor studies. However, based on these studies, as well as studies published in [129, 131], the impact of the divertor geometry on the divertor performance is not always as strong in JET as predicted by the fluid simulation tools.

Summary: *This work was the first series of JET H-mode EDGE2D-EIRENE simulations contrasting the operation with the horizontal and vertical LFS divertor configuration in ITER-like wall materials with and without nitrogen seeding. It was experimentally observed that in the unseeded plasmas, the two divertor configurations reach the same main SOL and pedestal electron density and temperature (pedestal only) profiles, as well as peak electron temperature at the LFS divertor plate. With the base case boundary conditions and cross-field transport assumptions, assuming the same electron density at the LFS mid-plane separatrix, the EDGE2D-EIRENE simulations reproduce the measured saturation currents and profiles at the LFS divertor target in the two configurations. However, whereas in the horizontal divertor configuration the model reproduces the measured main SOL density profile, in the vertical configuration the density 0.5 cm*

away from the separatrix, and further radially away, is underestimated by a factor of 2. There is no substantial difference predicted or measured in the reduction of the peak LFS divertor power as a function of the radiated power in the divertor. With increasing degree of detachment with nitrogen radiation, the horizontal divertor is predicted to detach uniformly across the entire LFS profile. With the vertical target, on the other hand, the detachment front propagates from the strike point towards the far SOL with increasing degree of detachment. These findings are consistent within the target Langmuir probe measurements, within their scatter.

The simulations did not include cross-field drifts or currents, which is why the focus has been on the LFS divertor. The drifts and currents are also expected to impact the predicted divertor and SOL flow patterns. Furthermore, the relative importance and the spatial distribution of drift and transport driven components may depend on the divertor geometry and ionization source distributions. These will further impact the predicted density profiles and impurity transport, which impact the predicted radiation profiles. Therefore, forthcoming studies should emphasize extending these simulations to include cross-field drifts and currents.

4.5 Impact of nitrogen and neon radiation on partially detached divertor operation in JET H-mode plasmas

Publication IV extends the vertical divertor studies in Publication I to seeding with neon. This publication compares the measured and predicted impact of nitrogen and neon radiation on the partially detached divertor operation in JET H-mode plasma of high-triangularity.

The simulations show that changing only the radiating species while maintaining all the other input parameters unchanged, the LFS divertor peak heat flux, $q_{\mathrm{LFS,\,DIV}}$, is reduced in similar fashion with either N_2 or Ne injection (Fig. 4.14a). This result is qualitatively consistent with experimental observations and obtained in the simulations when adjusting the impurity injection rate to reproduce the experimentally measured levels of radiation. However, whereas the radiative loss function of nitrogen peaks around electron temperatures of 10 – 40 eV, reducing to low values at temperatures above this region, the peaking region for neon extends from 20 eV up to 100 eV (Fig. 4.14b). Furthermore, for electron temperatures inside the pedestal ($T_e > 500$ eV), the radiative potential of neon is about a factor of 5 – 10 higher than that of nitrogen. As a

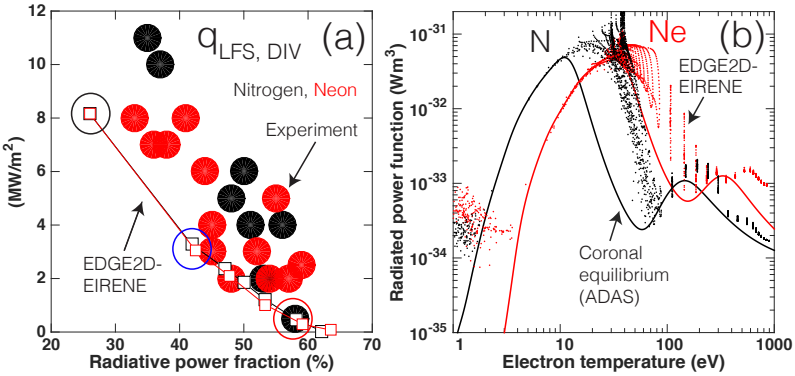

Figure 4.14. (a) Measured (solid circles) and predicted (connected hollow squares) LFS divertor peak heat flux as a function of radiated power fraction. The size of the symbols resembles the uncertainties in the measurements. Since the EDGE2D-EIRENE simulation grid includes only the pedestal and SOL regions, the radiated power fraction used as the x-axis for the simulations is calculated according to the formula $f_{\mathrm{rad}}^{\mathrm{EDGE2D\text{-}EIRENE}} = (P_{\mathrm{RAD}}^{\mathrm{EDGE2D\text{-}EIRENE}} + 4$ MW)/18MW, where 4 MW stands for the unaccounted core radiation contribution. The simulation cases representing the unseeded (black), medium-N_2/Ne (blue) and high-N_2/Ne (red) injection cases are circulated with color-coded circles b) The radiated power function for N (black), and Ne (red), as a function of electron temperature in coronal equilibrium (solid lines) and in EDGE2D-EIRENE simulations (dots) in the medium-N_2/Ne injection cases.

result, at impurity injection rates producing partially detached divertor conditions at the LFS divertor plate (the cases with the red circle in the Fig. 4.14a), more than 90% of nitrogen radiation in the computational domain is predicted to occur in the divertor chamber below the vertical height of Z = -1.2 m. The computational domain extends 12 cm inside the separatrix at the LFS-MP. Therefore, nitrogen seeding is predicted to enable partially detached divertor operation in JET with a very minor reduction of the power crossing the separatrix, P_{SOL}. On the other hand, in partially detached divertor conditions with neon injection, less than 50% of radiation is predicted to occur below the vertical height of Z = -1.2 m. As a result, at neon injection rates required for substantial reduction of $q_{\mathrm{LFS,\,DIV}}$, a substantial reduction of P_{SOL} is predicted. These findings are qualitatively consistent with experimental observations (Publication IV). Overall these findings are also consistent with ITER prediction, conducted with the SOLPS code package [209]. In this publication, the operational space with neon seeding is predicted to be more restricted than the operational space with nitrogen seeding, due to the proximity of P_{SOL} in ITER to the LH-transition threshold.

When adjusting the impurity injection rate to reproduce the measured

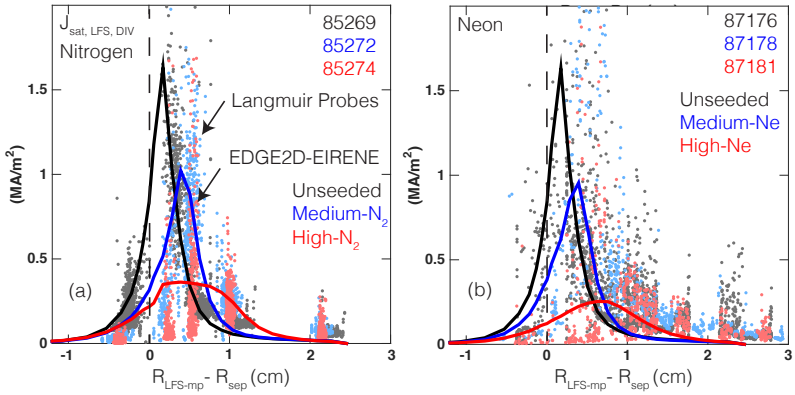

Figure 4.15. Measured (dots) and predicted (solid lines) LFS divertor saturation currents in the unseeded (black), medium seeding rate (blue), and high see-ding rate (red) plasmas with nitrogen (a) and neon (b) injection. The illustrated simulation cases are circled in the figure 1a.

radiated power, the simulations capture the experimentally observed particle and heat flux reduction at the LFS divertor plate (Figs. 4.15a and b). With both nitrogen and neon injection, the dominant particle flux reduction in the detachment assisted by impurities is caused by reduced deuterium ionization and recycling rate, which is possible due to reduced power reaching the deuterium ionization front. However, the divertor D_α-emission is underestimated by about a factor of 2 in the unseeded plasmas, and about a factor of 3 – 5 in the partially detached conditions, even though the LFS divertor particle fluxes are consistent with measured values. This indicates a shortfall in the deuterium radiation, similar to that observed throughout all simulations. Possible explanations for the radiation short fall are, at least, underestimation of the recombination and molecular contributions to D_α-emission. These underestimations can be caused by missing reactions, inaccurate rates, or inaccuracies in the background distributions of electron temperature and atomic and electron densities in the simulations. To solve the radiation short fall issue, one should re-assess the atomic and molecular emission channels for D_α, and further evaluate the possible pathways for missing radiation contribution in the simulations.

The impurity injection in these simulations was conducted with radiation feedback control, such that the simulation code injects as much impurities as is needed to produce a certain level of radiated power. For the medium and high impurity injection simulations in the Fig. 4.15, the impurity injection rates for nitrogen are 2e20 e/s and 1.7e21 e/s and for neon

they are 1.4e20 e/s and 1.2e21 e/s. Therefore, for these cases, roughly a factor of 2 higher nitrogen injection rate is needed to reproduce a similar radiated power level as with neon injection. However, these simulations do not take into account the surface chemistry and partial sticking of nitrogen, which is the dominant reason explaining that the simulated injection magnitudes are about an order of magnitude lower than the experimental levels. For neon, the predicted injection rate is about a factor of 2 lower than the experimentally used rate. These differences can be explained by uncertainties in the experimentally estimated injection rate as well as by uncertainties in the implementation of the pumping surfaces and albedos in EDGE2D-EIRENE.

Summary: *This work was the first series of JET H-mode EDGE2D-EIRENE simulations contrasting the operation with nitrogen and neon injection in ITER-like wall materials. Nitrogen and neon radiation were predicted and measured to provide a similar reduction of the inter-ELM LFS divertor heat loads for a given radiated power value. However, whereas nitrogen was measured and predicted to radiate dominantly in the divertor chamber, 50% of neon radiation was predicted and measured to occur inside the separatrix. Therefore, neon radiation is expected to reduce power crossing the separatrix in JET. The particle flux reduction in the LFS detachment is achieved in the simulations when imposing the radiated power with either nitrogen or neon.*

The simulations did not include cross-field drifts or currents, which is why the focus has been on the LFS divertor. The simulations consistently underestimate the radiation by fuel species. Therefore, forthcoming studies on the should concentrate on including the cross-field drifts and currents as well as addressing the shortfall of radiation by fuel species.

5. Predictions of tungsten divertor retention in JET high confinement mode plasmas with and without ELMs

Publications V and VI provide predictions for tungsten retention in the JET divertor assuming H-mode plasma conditions consistent with divertor measurements in the previous JET-C. In publication VI, the divertor retention was investigated assuming a steady-state, inter-ELM plasma, and in publication V these studies were extended by including an ELM-like heat pulse event into the EDGE2D-EIRENE simulations, and investigating the impact of this event on the divertor retention of tungsten.

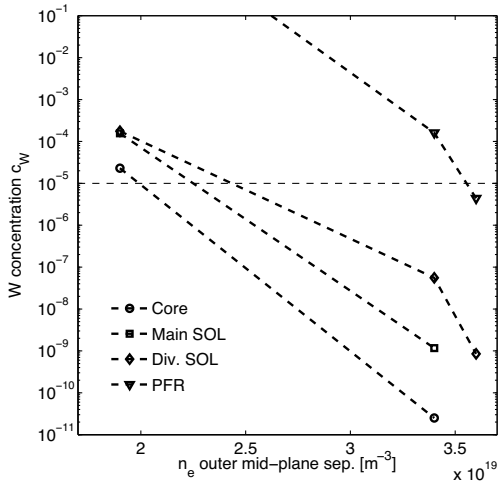

Figure 5.1. Tungsten concentration in the core, main SOL, divertor SOL and private flux region for the three upstream densities: $n_{e,\,\mathrm{sep\,OMP}} = 1.9 \times 10^{19}$ m^{-3} (low), 3.4×10^{19} m^{-3} (medium) and 3.6×10^{19} m^{-3} (high).

Publication VI provides predictions of tungsten contamination extrapolated from an inter-ELM phase of a high-triangularity, H-mode, JET-ILW reference plasma without impurity seeding in JET-C. Tungsten concentrations for equivalent ILW plasmas are predicted for low, medium and high upstream densities, utilizing the Monte Carlo trace-impurity code DIVIMP on background plasmas calculated with the 2D multi-fluid code

EDGE2D- EIRENE. It is observed that operation at the low-upstream-density plasma, $n_{e,\,\text{LFS-MP, sep}} = 1.8 \times 10^{19}$ m^{-3}, with a sheath-limited scrape-off layer leads to a core tungsten concentration of the order of 10^{-5} (Fig. 5.1). Increasing the density leads to a high-recycling scrape-off layer, $n_{e,\,\text{LFS-MP, sep}} = 3.4 \times 10^{19}$ m^{-3}, with sufficient divertor retention to ensure an acceptable core tungsten concentration that is less than 10^{-5}. Sufficient divertor retention is achievable if the peak target electron temperature, T_e , is below 10 eV. Achieving a significant reduction in tungsten sputtering by multiple charged impurity species (e.g. Be^{2+} and C^{4+}) requires a peak target T_e below 5 eV, which requires strong divertor radiation, achieved by impurity seeding in the ILW configuration.

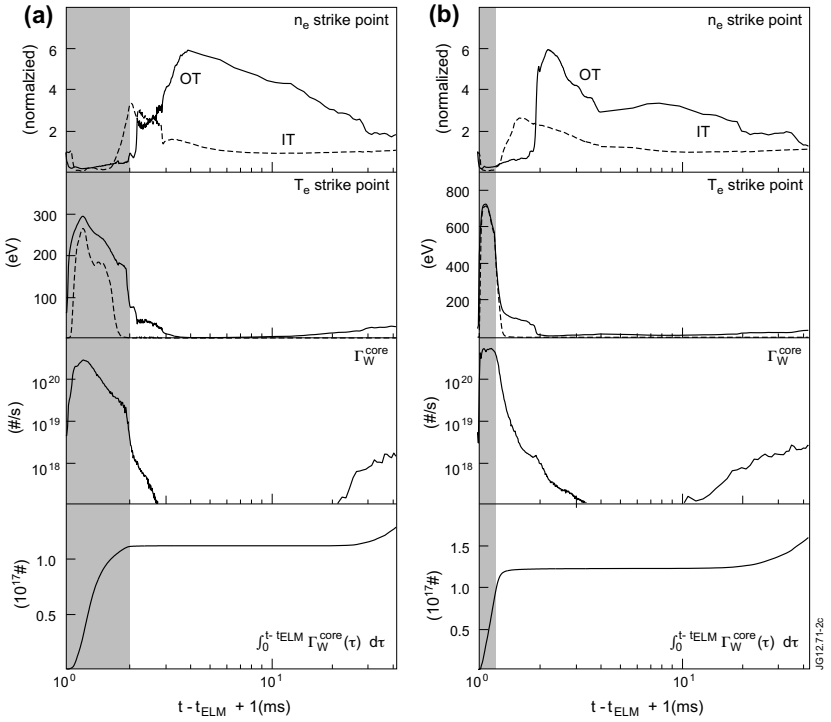

Figure 5.2. ELM evolution of strike point electron density, n_e, and temperature, T_e, core tungsten contamination rate, c_W,core, and integrated core tungsten contamination over the ELM cycle for 1 ms (a) and 0.2 ms (b) ELMs. The electron densities are normalized to their pre-ELM values. The inner target (IT) strike point values are plotted with dashed lines, and the outer target (OT) strike point values with solid lines. The shadowed area marker the assumed intra-ELM phase (of enhanced outer mid-plane cross-field diffusion). The reader should note the logarithmic time axis.

These studies were continued in Publication V by dynamically evolving the steady-state EDGE2D-EIRENE base case over an ELM-like pedestal crash, and simulating tungsten erosion and transport with the Monte-

Carlo code DIVIMP. Two ELM durations were considered: 1 ms and 0.2 ms (Fig. 5.2). This approach was first used in the simulations conducted for the JET ELMy H-mode study published by Wiesen et al. in [258]. The simulated ELMs lead to a cycle of sheath-limited plasma conditions with target temperatures exceeding a few 100 eV during the first few 100 μs after the ELM onset, followed by high-recycling conditions with target temperatures of about 1 – 25 eV approximately 500 – 1500 μs after the ELM onset. The SOL density remains elevated several milliseconds after the ELM onset. This dynamics leads to significantly increased tungsten sputtering and core contamination during the sheath-limited, intra-ELM phase, via increased sputtered velocity and suppressed background ion friction. The high recycling conditions during the ELM recovery phase lead to suppression of tungsten sputtering and core leakage, via lowered target temperatures and increased divertor collisionalities. Therefore, according to the simulations in this study, the tungsten core contamination of ELMy H-mode plasmas is strongly determined by the divertor plasma characteristics during an ELM. On the other hand, ELMs are also considered as one of the dominant process reducing the core tungsten contamination by flushing tungsten out from the pedestal plasma and, hence, core-edge integrated simulations are necessary to describe the combined effect. The simulations show approximately 50% of the core tungsten contamination originating from sputtering due to deuterium, when self-sputtering is neglected. Accordingly, increasing the concentration of light impurities in the divertor plasma is not predicted to increase the tungsten impurity source significantly, while the core tungsten contamination is anticipated to be decreased due to lowered divertor temperatures and increased collisionalities.

Summary: *This work was the first series of DIVIMP predictions of divertor retention of tungsten in JET H-mode plasmas in the ITER-like wall. The simulations show that high density, low temperature divertor operation is beneficial for minimizing tungsten contamination of the confined plasmas. Furthermore, ELMs are predicted to dominate the erosion and leakage tungsten out of the divertor chamber.*

These simulations were fully predictive. These studies should be continued with already established plasmas. The EDGE2D-EIRENE simulations conducted in the radiative divertor simulations section in this thesis can be used as base cases for those DIVIMP studies.

6. Conclusions and future prospects

Fusion reactors must maintain sufficiently low surface heat loads, < 5 – 10 MW/m^2, at the PFM surfaces, while producing several gigawatts of fusion power. To address these issues, radiative divertor studies with and without nitrogen and neon injection were investigated experimentally and interpreted with the multi-fluid code package EDGE2D-EIRENE for sets of dedicated high-confinement mode plasmas in JET. The studies include comparison of predicted and measured divertor conditions, investigations of the impact of the PFMs and divertor geometry on the radiative divertor performance, and comparison of radiative divertor performance with nitrogen and neon injection. Furthermore, predictions for tungsten retention in the divertor chamber with the Monte-Carlo code DIVIMP were conducted.

The studies show that when imposing the measured radiated power in the divertor by impurity injection in the simulations, the simulations capture the experimentally observed radiated power levels, distributions of radiated power, and reduction of the low-field side (LFS) divertor target power and particle deposition. However, consistent with earlier studies, the simulations underestimate the radiated power by deuterium, indicating a shortfall in the radiation from fuel species. Since nitrogen radiates preferentially in low electron temperatures of 10 – 30 eV, more than 90% is predicted to occur outside the separatrix. Therefore, nitrogen is a very good divertor radiator for H-mode plasmas in JET sized tokamaks. The simulations reproduce the experimentally observed spatial shift of the NII (500 nm) line-emission zone from the divertor leg to next to the X-point, and show that this emission zone is a suitable proxy for the deuterium ionization front. The divertor particle flux reduction is predicted to occur predominantly due to reduced deuterium ionization and recycling rate, which is possible due to extrinsic impurity radiation and reduced power

flow reaching the deuterium ionization front.

The studies show that due to the similar radiative characteristics of nitrogen and carbon, the carbon-like divertor radiation levels and distributions can be obtained in JET with nitrogen seeding, also after changing from full carbon PFMs to the tungsten and beryllium PFMs. Furthermore, detachment is obtained at similar divertor radiation levels ($\sim 50\%$ of P_{SOL}) in both PFM configurations.

EDGE2D-EIRENE simulations show that the divertor heat fluxes at the low field side (LFS) can be reduced with N_2-injection in similar fashion in both horizontal and vertical LFS divertor configurations, qualitatively consistent with experimental observations. However, the simulations show no substantial difference between the two configurations in terms of reduction of the peak heat flux at the LFS divertor plate as a function of the divertor radiation, nitrogen concentration, or pedestal Z_{eff}. The predictions are consistent with experiments showing similar divertor radiation and nitrogen injection levels for similar LFS peak heat flux reduction for both configurations.

Similar levels of LFS heat load reduction can be obtained at JET with either nitrogen or neon injection. This is observed both in the simulations and in the experiments. The simulations reproduce the experimentally observed LFS heat and particle flux reduction with both N_2 and Ne radiation, when adjusting the impurity injection rate to reproduce the measurements of radiated power in the divertor. However, the simulations consistently underestimate the divertor D_α-intensity by a factor of 3 – 5, indicating a shortfall in the radiation by fuel species. Whereas nitrogen radiation is concentrated in the divertor chamber in JET, neon radiation is predicted and measured to occur partially in the confined plasma. Therefore, neon injection is predicted to reduce the power crossing the separatrix in JET in partially detached divertor conditions.

The predictions for tungsten retentions indicate that, as expected, high-density, low-temperature divertor operation is predicted to be beneficial for improving tungsten retention in the divertor of JET. This is due to higher collisional coupling of the tungsten impurities to the background deuterium flow. Furthermore, edge-localized modes (ELMs) are predicted to dominate tungsten erosion and leakage out of the divertor chamber in JET.

Although the amount of experimental and numerical investigations conducted within this doctoral thesis can be considered rather comprehen-

sive, it should be observed that many research questions were left unexamined. Since these H-mode plasmas exhibited ELMs, an obvious question to raise is whether the steady-state inter-ELM model can provide a realistic description of the power exhaust physics in these plasmas. Although the ELM frequency in these plasmas is sufficiently low, less than 100 Hz, compared to parallel SOL transport time scales $\sim$ 1 ms, outgassing of the PFM and refilling physics [259] may evolve on longer time scales, comparable to the inter-ELM time. Furthermore, the impact of ELMs and ELM burn-through on the impurity density and charge state distribution, as well as on the stability and dynamics of the radiation and detachment fronts, were not addressed in this doctoral thesis. Numerically, investigations of these physics features could be conducted by imposing ELM-like heat pulses by enhancing the pedestal cross-field transport in EDGE2D-EIRENE for a short time period based on the existing base cases published in this doctoral thesis. For more sophisticated approach, full core edge coupled simulations with the JINTRAC/COCONUT code package should be conducted [260]. The EDGE2D-EIRENE simulations in this doctoral thesis provide the necessary reference base for those core-edge coupled simulations.

Since deuterium emission is underestimated throughout the impurity injection scans in this study, thorough investigations of the deuterium radiation and emission channels should be conducted. This is best done in unseeded, well-characterized L-mode plasmas first, since the physics mechanisms responsible for the underestimation are not foreseen to differ between operation modes. Such studies are being conducted [131, 148, 95, 261, and references therein].

Since all the simulations discussed in this doctoral thesis have been conducted without cross-field drift terms and currents in the SOL, the impact of drifts on the radiative divertor performance is a natural way to continue the work conducted in this thesis. Based on the L-mode studies published in [147, 148, and references therein], the expected outcome is that the drifts will have a considerable impact on the LFS to HFS divertor asymmetries in the unseeded reference plasmas in high recycling divertor conditions. Once the plasma enter cooler divertor conditions with partial of complete detachment, the impact of drifts on the asymmetries is expected to be reduced. Since stronger poloidal and radial SOL gradients are expected in H-mode plasmas than in the L-mode plasmas, the impact of drifts is expected to be stronger in H-mode plasmas as well.

The tungsten transport predictions in this doctoral thesis were conducted only for the EDGE2D-EIRENE simulations corresponding to the JET-C plasmas. These studies were not yet extended to the JET-ILW simulations with and without impurity injection. Therefore, the predictions in this doctoral thesis should be continued in dedicated studies of tungsten transport with EDGE2D-EIRENE and DIVIMP in the obtained JET-ILW reference simulations. These could be compared to experiments as well for model validation. Furthermore, the impact of ELMs with impurity injection on the erosion and transport of tungsten could be conducted, once the ELM simulations reach a sufficiently mature state.

In the divertor geometry studies, the far SOL densities were strongly underestimated with vertical LFS divertor targets. The impact of cross-field transport assumptions on the density profile predictions in horizontal and vertical divertors could be conducted as a continuation of this project.

Main chamber interaction has not been discussed in this doctoral thesis. Impact of the main chamber recycling on the SOL characteristics and pedestal fuelling in high and low triangularity plasmas with various divertor configurations would provide a useful research topic as well. However, satisfactory work in this area would presumably require improvements in the main chamber interaction in the simulations code, such as extension of the calculation grid to the main chamber wall.

To prioritize the various avenues in this outlook, assessment of the deuterium radiation short fall is considered as the highest priority task. However, as was discussed already, this assessment is best to be done in L-mode plasmas, which are considered easier to measure, simulate and analyze than H-mode plasmas. As a continuation of the radiative divertor work conducted in this study, inclusion of drifts and currents and assessment of the predicted and measured HFS to LFS divertor asymmetries is considered as a very high priority project. Following the drifts and currents, assessment of the impact of ELMs on the radiative divertor performance is the next project in the priority list. The final items on the prioritized list are assessment of the impact of cross-field transport assumptions and main chamber interactions on the divertor and SOL characteristics. Investigations of tungsten transport can be conducted as a separate project parallel to the tasks listed above.

Bibliography

[1] World Energy Council, *World Energy Scenarios: Compising energy futures to 2050*. World Energy Council, 2013

[2] Intergovernmental Panel on Climate change. *Climate Change 2013: The Physical Science Basis. Contribution of Working Group I to the Fifth Assessment Report of the Intergovernemental Panel on Climate Change*. Cambridge University Press, 2013. ISBN: 978-1-107-66182-0

[3] D. Reiter, *et al., Nucl. Fusion* **30** (1990) 2141

[4] M. Ghoranneviss and A. Salar Elahi, *Science and Technology of Nuclear Installations* (2014) 802054

[5] ITER Physics Basis editors, *Nucl. Fusion* **39** (1999) 12

[6] Progress in the ITER Physics Basis editors, *Nucl. Fusion* **47** (2007) S1 – S17

[7] F. Romanelli *et al., A roadmap to the realisa-tion of fusion energy*, ISBN 978-3-00-040720-8, 2012

[8] U.S. Department of Energy, Fusion Energy Sciences Advisory Committee, Report on Strategic Planning, 2012

[9] Y. Tao Song, *et al., IEEE Trans. Plasma Sci.* **42** (2014) 3

[10] N. Nakajima, *et al., Proceedings of the 24th IAEA FEC*, San Diego, USA 8 – 13 October 2012

[11] G.H. Neilson, *et al., Nucl. Fusion* **52** (2012) 047001

[12] J. Wesson, *Tokamaks*, 4th Edition, Oxford University Press, 2011, ISBN 978-0-19-959223-4

[13] M. Kikuchku, K. Lackner, M. Quang Tran, *et al., Fusion Physics*, IAEA Publishing 2012, ISBN 978-92-0-130410-0

[14] Y. Kamada, *et al., Fus. Sci. Tech.* **42** (2002) 185 – 254

[15] A. Weller, *et al., Nucl. Fusion* **49** (2009) 065016

[16] M. Greenwald, *et al., Plasma Phys. Control. Fusion* **44** (2002) R27 – R80

[17] H. Zohm, *et al., Nucl. Fusion* **53** (2013) 073019

[18] M. Keilhacker, *et al., Nucl. Fusion* **39** (1999) 2

[19] F. Troyon, *et al., Plasma Phys. Control. Fusion* **30** (1988) 1597

[20] M. Greenwald, *et al., Nucl. Fusion* **28** (1988) 2199 – 2207

[21] E. J. Doyle, *et al., Nucl. Fusion* **47** (2007) S18 – S127

[22] F. Wagner, *et al., Plasma Phys. Control. Fusion* **49**, (2007), B1 – B33

[23] K. Kamiya, *et al., Plasma Phys. Control. Fusion* **49**, (2007), S43 – S62

[24] P.T. Lang, *et al., Nucl. Fusion* **53** (2013) 043004

[25] Y. R. Martin, *et al., J. Phys. Conf. Ser.* **123** (2008) 012033

[26] R.A. Pitts, *et al., J. Nucl. Mater.* **415** (2011) S957– S964

[27] W.J. Corbett, *et al., Nucl. Fusion* **31** (1991) 1067

[28] T. Loarer, *et al., Nucl. Fusion* **36** (1996) 225

[29] L. Spitzer, *Rep. NYO-993 (PM-S-1)*, US Atomic Energy Commission

[30] D. Post, *et al., Phys. Plasmas* **2** (1995) 2328

[31] P.C. Stangeby, *The Plasma Boundary of Magnetic Fusion Devices*, IoP Publishing, (2000), ISBN 0 7503 0559 2

[32] D. Bohm, *The Characteristics of Electrical Discharges in Magnetic Fields*, New York: McGraw-Hill, 1949

[33] R. Chodura, *Physics of Plasma-Wall Interactions in Controlled Fusion*, New York: Plenum Press, 1986

[34] G. Federici, *et al., Nucl. Fusion* **41** (2001) 1967

[35] E.B. Meservey, *et al., J. Nucl. Mater.* **93 – 94** (1980) S267– S271

[36] G.F. Matthews, *et al., Phys. Scr.* **T145** (2011) 014001

[37] R. Neu, *et al., Plasma Phys. Control. Fusion* **49** (2007) B59 – B70

[38] B. Lipschultz, *et al., Nucl. Fusion* **41** (2001) 5

[39] R. Neu, *et al., Plasma Phys. Control. Fusion* **53** (2011) 124040

[40] G. J. van Rooij, *et al., J. Nucl. Mater.* **438** (2013) S42 – S47

[41] R. Dux, *et al., J. Nucl. Mater.* **390 – 391** (2009) 858 – 863

[42] D. Maisonnier, *et al., Nucl. Fusion* **47** (2007) 1524 – 1532

[43] T. Pütterich, *et al., Nucl. Fusion* **50** (2010) 025012

[44] R. Simonini, *et al., Contrib. Plasma Phys.* **34** (1994) 368 – 373

[45] D. Reiter, *et al., J. Nucl. Mater.* **196 – 198** (1992) 80 – 89

[46] S. Wiesen, *EDGE2D/EIRENE code interface report*, JET ITC-Report, http://www.eirene.de/e2deir_report_30jun06.pdf

[47] P.C. Stangeby and J.D. Elder, *J. Nucl. Mater.* **220** (1995) 612

[48] A. Kallenbach, *et al., Nucl. Fusion* **52** (2012) 122003

[49] M. Kotschenreuther, *et al., Nucl. Fusion* **50** (2010) 035003

[50] K. Lackner, *Comments Plasma. Phys. Control. Fusion* **15** (1994) 359 – 365

[51] T. Eich, *et al., Phys. Rev. Lett.* **107** (2011) 215001

[52] B. Lipschultz, *et al., Nucl. Fusion* **47**, (2007), 1189 – 1205

[53] I.H. Hutchinson, G.C. Vlases, *Nucl. Fusion* **36** (1996) 783 – 794

[54] M. Wischmeier, *et a. J. Nucl. Mater.* **463** (2015) 22 – 29

[55] M.A. Makowski, *et al., Phys. Plasmas* **19** (2012) 056122

[56] T. Eich, *et al., Nucl. Fusion* **53** (2013) 093031

[57] A. Scarabosio, *et al., J. Nucl. Mater.* **436** (2015) 49 – 54

[58] A. Kallenbach, *et al., J. Nucl. Mater.* **415** (2011) S19 – S26

[59] A. Kallenbach, *et al., Plasma Phys. Control. Fusion* **55** (2013) 124041

[60] M.E. Fenstermacher, *et al., Plasma Phys. Control. Fusion* **41** (1999) A345

[61] H.P. Summers, *Atomic data and analysis structure users manual*, JET-IR 06, JET Joint undertaking, (1994). http://open.adas.ac.uk/

[62] V.A. Vershkov, and A.V. Chankin, *Sov. J. Plasma Phys.* **15** (1989) 371

[63] S.I. Braginskii, *Reviews in Plasma Physics vol 1*, (1965), New York, p. 205

[64] W. Fundamenski, *Plasma Phys. Control. Fusion* **47** (2005) R163 – R208

[65] R. Chodura, *Contrib. Plasma Phys.* **32** (1992) 219 – 230

[66] O.V. Batishchev, *et al., Phys. Plasmas* **3** (1996) 3386

[67] L. Spitzer, R. Härm, *Phys. Rev. Let.* **89** (1952) 5

[68] V. Kotov, *et al., Plasma Phys. Control. Fusion* **50** (2008) 105012

[69] R.K. Janev, *et al., Elementary Processes in Hydrogen-Helium Plasmas*, (1987), Berlin: Springer

[70] K. Sawada, T. Fujimoto, *J. Appl. Phys.* **78** (1995) 2913

[71] P. Bachmann, D. Reiter, *Contrib. Plasma Phys.* **35** (1995) 1

[72] D. Reiter, *The data file HYDHEL: Atomic and Molecular Data for EIRENE* based upon: Janev, Langer, Evans, Post, *Elementary Processes in Hydrogen-Helium Plasmas*, Springer 1987, and http://www.eirene.de/manuals/hydhel.pdf

[73] D. Reiter, *The data file AMJUEL: Additional Atomic and Molecular Data For EIRENE*, version: June 26 (2015), and http://www.eirene.de/html/amjuel.html

[74] G.J. Schulz, R.K. Asundi, *Phys. Rev. A* **158** (1967) 1

[75] J.M. Wadehra, J.N. Bardsley, *Phys. Rev. Lett.* **41** (1978) 1795

[76] D.A. Skinner, *et al., Phys. Rev. E* **48** (1993) 2122.

[77] P. Berlemont, D.A. Skinner, M. Bacal, *Rev. Sci. Instrum.* **64** (1993) 10

[78] M.G. Holliday, J.T. Muckerman, L. Friedman, *Chem. Phys.* **54** (1971) 3

[79] C. Derkits, *et al., J. Phys. B: At. Mol. Phys.* **12** (1979) L529

[80] B. Peart, D.A. Hayton, *J. Phys. B: At. Mol. Opt. Phys.* **25** (1992) 5109 – 5119

[81] D. Fussen, C. Kubach, *J. Phys. B: At. Mol. Phys.* **19** (1986) L31 – L34

[82] R.K. Janev, A.R. Tancic, *J. Phys. B: At. Mol. Phys.* **5** (1972) L250 – L252

[83] B. Peart, R. Grey, K.T. Dolder, *J. Phys. B: At. Mol. Phys.* **9** (1976) L369

[84] D.R. Bates, A.E. Kingston, R.W.P. McWhirter, *Proc. Roy. Soc. London Ser. A* **267** (1962) 297 – 312

[85] D.E. Post, *J. Nucl. Mater.* **220 – 222** (1995) 143 – 157

[86] G.F. Matthews, *et al., J. Nucl. Mater.* **220 – 222** (1995) 104 – 116

[87] P.C. Stangeby, *et al., Nucl. Fusion* **33** (1993) 11.

[88] S.I. Krasheninnikov, *et al., Phys. Lett. A* **214** (1996) 285 – 291.

[89] D. Reiter, *et al., J. Nucl. Mater.* **241 – 243** (1997) 342 – 348

[90] A.S. Kukushkin, *et al., Fus. Eng. Design* **86** (2011) 2865 – 2873

[91] C. Guillemaut, *et al., Nucl. Fusion* **54** (2014) 093012

[92] V. Kotov, D. Reiter and A. S. Kukushkin, *Report J§l-4257*, www.eirene.de/kotov_solps42_report.pdf, 2007

[93] A.S. Kukushkin, *et al., Nucl. Fusion* **45** (2005) 608

[94] M. Wischmeier, *et al., Proc. of the 24th IAEA FEC Conference*, San Diego, California, USA, 2012

[95] M. Groth, *et al., Nucl. Fusion* **53** (2013) 093016

[96] B. Lipschultz, *et al., Nucl. Fusion* **24** (1984) 8

[97] F. Reimold, *et a. Nucl. Fusion* **55** (2015) 033004

[98] B. LaBombard, *et al., Phys. Plasmas* **2** (1995) 2242

[99] B. Lipschultz, *et al., Fus. Sci. Tech.* **51** (2007) 369 – 389

[100] J.D. Swift, M.J.R. Schwar, *Electrical probes for plasma diagnostics*, (1969), London, Elsevier

[101] B. Lipschultz, *et al., J. Nucl. Mater.* **220 – 222** (1995) 50 – 61

[102] A. Loarte, *et al., J. Nucl. Mater.* **241 – 243** (1997) 118 – 134

[103] K. Borras, *et al., J. Nucl. Mater.* **241 – 243** (1997) 250 – 254

[104] S.I. Krashenninikov, *et al., Phys. Plasmas* **4** (1997) 1638

[105] D. Lumma, *et al., Phys. Plasmas* **4** (1997) 7

[106] G.M. McCracken, *et al., Nucl. Fusion* **38** (1998) 4

[107] R.C. Isler, *et al., Phys. Plasmas* **4** (1997) 2989

[108] U. Wenzel, *et al., Nucl. Fusion* **39** (1999) 7

[109] A. S. Kukushkin, *et al., Proc. 20th Int. Conf. on Fusion Energy* 2004 (Vilamoura, Portugal, 2004)

[110] J.L. Terry, *et al., Phys. Plasmas* **5** (1998) 1759

[111] F. Reimold, *et al., J. Nucl. Mater.* **463** (2015) 128 – 134

[112] D.D. Ryutov, *et a. Phys. Scr.* **89** (2014) 088002

[113] A. Kallenbach, *et al., Nucl. Fusion* **55** (2015) 053026

[114] B. LaBombard, *et al., Nucl. Fusion* **40** (2000) 12

[115] B. Lipschultz, *et al., Phys. Plasmas* **6** (1999) 5

[116] S. Wiesen, *et al., J. Nucl. Mater.* **415** (2011) S535 – S539

[117] D. Carralero, *et al., Nucl. Fusion* **54** (2014) 123005

[118] S.I. Krasheninnikov, *et al., J. Plasma Phys.* **74** (2008) 679717

[119] H.W. Müller, *et al., J. Nucl. Mater.* **463** (2015) S739 – S743

[120] G.F. Matthews, *et al., Nucl. Fusion* **39** (1999) 19

[121] L.D. Horton, *et al., Nucl. Fusion* **39** (1999) 1

[122] G.D. McCracken, *et al., Nucl. Fusion* **39** (1999) 41

[123] O. Gruber, *et al., Nucl. Fusion* **39** (1999) 1321

[124] S.L. Allen, *et al., Nucl. Fusion* **39** (1999) 2015

[125] A. Loarte, *et al., Plasma Phys. Control. Fusion* **43** (2001) R183 – R224

[126] R. Schneider, *et al., J. Nucl. Mater.* **266 – 269** (1999) 175 – 181

[127] A. Kallenbach, *et al., Nucl. Fusion* **39** (1999) 7

[128] N. Asakura, *et al., Nucl. Fusion* **39** (1999) 1983

[129] A. Loarte, *et al., Nucl. Fusion* **38** (1998) 3

[130] M.A. Mahdavi, *et al., Fus. Sci. Tech.* **48** (2005) 1072 – 1082

[131] M. Groth, *et al., J. Nucl. Mater.* **463** (2015) 471 – 476

[132] D. Moulton, *et al., Proc. of the 42nd EPS conference on Plasma Physics*, Lisbon, Portugal, 22 – 26 of June, 2015

[133] C.S. Pitcher, P.C. Stangeby, *Plasma Phys. Control. Fusion* **39** (1997) 779 – 930

[134] A.V. Chankin, *J. Nucl. Mater.* **241 – 243** (1997) 199 – 213

[135] A.V. Chankin, *et al., Plasma Phys. Control. Fusion* **57** (2015) 095002

[136] G.M. Staebler, *Nucl. Fusion* **36** (1996) 11

[137] M.J. Schaffer, *et al., Phys. Plasmas* **8** (2001) 2118

[138] A.V. Chankin, *et al., Plasma Phys. Control. Fusion* **36** (1994) 1853 – 1864

[139] B. LaBombard, *et al., J. Nucl. Mater.* **241 – 243** (1997) 149 – 166

[140] R.A. Pitts, *et al., J. Nucl. Mater.* **337 – 339** (2005) 146 – 153

[141] N. Asakura, *et al., Nucl. Fusion* **36** (1996) 6

[142] A.W. Leonard, *et al., J. Nucl. Mater.* **220 – 222** (1995) 325 – 329

[143] I.H. Hutchinson, *et al., Plasma Phys. Control. Fusion* **38** (1996) A301 – A309

[144] I.H. Hutchinson, *et al., Plasma Phys. Control. Fusion* **37** (1995) 1389 – 1406

[145] D.N. Hill, *et al., Nucl. Fusion* **28** (1988) 5

[146] S.L. Allen, *et al., Plasma Phys. Control. Fusion* **37** (1995) A191 – A202

[147] L. Aho-Mantila, *et al., Proceedings of the 25th IAEA FEC*, 13 – 18 October 2014, Russia

[148] M. Groth, *et al., Proceedings of the 25th IAEA FEC*, 13 – 18 October 2014, Russia

[149] P.J. Harbour, *Contrib. Plasma Phys.* **28** (1988) 417 – 419

[150] P.J. Harbour, *et al., J. Nucl. Mater.* **162 – 164** (1989) 236 – 244

[151] G.M. Steabler, F.L. Hinton, *Nucl. Fusion* **29** (1989) 1820

[152] T.D. Rognlien, *et al., J. Nucl. Mater.* **266 – 269** (1992) 654

[153] R. Schneider, *et al., Contrib. Plasma Phys.* **46** (2006) 3

[154] H. Kawashima, *et al., Plasma Fusion Res.: Regular Art* **1** (2006) 31

[155] S. Wiesen, *et al., J. Nucl. Mater.* **463** (2015) 480 – 484

[156] Y. Feng, *et al., Contrib. Plasma Phys.* **44** (2004) 57 – 69

[157] C. Giroud, *et al., Plasma Phys. Control. Fusion* **57** (2015) 035004

[158] D. Tskhakaya, *et al., Contrib. Plasma Phys.* **48** (2008) 1 – 3

[159] L.L. Lao, *et al., Nucl. Fusion* **25** (1985) 1421

[160] D.P. O'Brien, *et al., Nucl. Fusion* **32** (1992) 1351

[161] W. Zwingmann, *et al., Proc. 7th European Fusion Theory Conference*, Jülich (1997)

[162] D. Reiter, *et al., Database for recycling and penetration of neutral helium atoms in the boundary of a fusion plasma*, KFA-Jülich report, Jül-2605 Forschunszentrum Jülich, Germany (April 1992)

[163] W. Eckstein, *et al., Sputtering by particle Bombardment*, Springer Publishing, (2007), ISBN 978-3-540-44502-9

[164] D. Reiter, *electronic file*, FZ-Jülich, www.eirene.de

[165] M. Keilhacker, *et al., Nucl. Fusion* **31** (1991) 3

[166] K. Itami, *et al., Plasma Phys. Control. Fusion* **37** (1995) A255 – A265

[167] B. Lipschultz, *et al., J. Nucl. Mater.* **241 – 243** (1997) 771 – 776

[168] G.F. Matthews, *et al., Plasma Phys. Control. Fusion* **37** (1995) A227 – A239

[169] J. Neuhauser, *et al., Plasma Phys. Control. Fusion* **37** (1995) A37 – A51

[170] U. Samm, *et al., Plasma Phys. Control. Fusion* **35** (1993) B167 – B175

[171] O. Gruber, *et al., Phys. Rev. Lett.* **74** (1995) 4217

[172] A. Kallenbach, *et al., Nucl. Fusion* **35** (1995) 1231

[173] P. Dumortier, *et al., Plasma Phys. Control. Fusion* **44** (2002) 1845

[174] J. Ongena, *et al., Nucl. Fusion* **44** (2004) 124

[175] P. Monier-Garbet, *et al., Nucl. Fusion* **45** (2005) 1404

[176] E.A. Lazarus, *et al., J. Nucl. Mater.* **121** (1984) 61

[177] E.A. Lazarus, *et al., Nucl. Fusion* **25** (1985) 2

[178] A.M. Messiaen, *et al., Nucl. Fusion* **34** (1994) 6

[179] G. Maddison, *et al., J. Nucl. Mater.* **415** (2010) S313 – S317

[180] G. Maddison, *et al., Nucl. Fusion* **51** (2011) 042001

[181] C. Giroud, *et al., Nucl. Fusion* **52** (2012) 063022

[182] C. Giroud, *et al., Nucl. Fusion* **53** (2013) 113025

[183] N. Asakura, *et al., Nucl. Fusion* **49** (2009) 115010

[184] J. Ongena, *et al., Plasma Phys. Control. Fusion* **41** (1999) A379 – A399

[185] J. Rapp, *et al., Nucl. Fusion* **44** (2004) 312 – 319

[186] T.W. Petrie, *et al., Nucl. Fusion* **48** (2008) 045010

[187] T.W. Petrie, *et al., Nucl. Fusion* **49** (2009) 065013

[188] T.W. Petrie, *et al., Nucl. Fusion* **37** (1997) 3

[189] J. Rapp, *et al., Nucl. Fusion* **49** (2009) 095012

[190] A. Kallenbach, *et al., Plasma Phys. Control. Fusion* **52** (2010) 055002

[191] G. Maddison, *et al., Nucl. Fusion* **54** (2014) 073016

[192] M. Reinke, *et al., J. Nucl. Mater.* **415** (2011) S340 – S344

[193] C. Giroud, *et al., Proceedings of the 25th IAEA FEC*, 13 – 18 October 2014, Russia

[194] M.N.A. Beurskens, *et al., Plasma Phys. Control. Fusion* **55** (2013) 124043

[195] A. Kallenbach, *et al., Plasma Phys. Control. Fusion* **38** (1996) 2097

[196] G.L. Jackson, *et al., Nucl. Fusion* **42** (2002) 28 – 41

[197] H. Kubo, *et al., Nucl. Fusion* **41** (2001) 2

[198] J.D. Strachan, *et al., Plasma Phys. Control. Fusion* **42** (2000) A81 – A88

[199] G. Saibene, *et al., Plasma Phys. Control. Fusion* **44** (2002) 1769 – 1799

[200] J. Schweinzer, *et al., Nucl. Fusion* **51** (2011) 113003

[201] S.L. Allen, *et al., J. Nucl. Mater.* **220 – 222** (1995) 336 – 341

[202] G.F. Matthews, *et al., J. Nucl. Mater.* **241 – 243** (1997) 450 – 455

[203] P. Devynck, *et al., Proceedings of the 39th EPS Conference on Plasma physics*, Stockholm, Sweden 2 – 6 July 2012

[204] A. Kallenbach, *et al., Proceedings of the 24th IAEA FEC*, 8 – 13 October 2012, San Diego, USA

[205] L. Aho-Mantila, *et al., J. Nucl. Mater.* **463** (2015) 546 – 550

[206] B.J. Braams, *et al., Contrib. Plasma Phys.* **36** (1996) 2/3

[207] Y. Chen, *et al., Phys. Plasmas* **20** (2013) 022311

[208] A.S. Kukushkin, *et al., J. Nucl. Mater.* **463** (2015) 586 – 590

[209] H.D. Pacher, *et al., J. Nucl. Mater.* **463** (2015) 591 – 595

[210] G.D. Porter, *et al., Phys. Plasmas* **17** (2010) 112501

[211] N. Asakura, *et al., Nucl. Fusion* **53** (2013) 123013

[212] K. Hoshino, *et al., J. Plasma Fusion Res. SERIES* **9** (2010) 592 – 597

[213] H. Kawashima, *et al., Fusion Eng. Design* **83** (2008) 1643 – 1647

[214] R. Schneider, *et al., Contrib. Plasma Phys.* **46** (2006) 3 – 191

[215] M. Wischmeier, *et al., J. Nucl. Mater.* **415** (2011) S523 – S529

[216] A.V. Chankin, *et al., Nucl. Fusion* **49** (2009) 015004

[217] M. Oberkofler, *et al., J. Nucl. Mater.* **438** (2013) S258 – S261

[218] F.L. Tabarés, *Plasma Sources Sci. Technol.* **22** (2013) 033001

[219] R. Lässer, *et al. Fus. Eng. Design* **47** (1999) 173 – 203

[220] H. Weisen, *et al. AIP Conf. Proc.* **1612** (2014) 77

[221] F. Romanelli, *et al., Nucl. Fusion* **53** (2013) 104002

[222] P. de Vries, *et al., Plasma Phys. Control. Fusion* **54** (2012) 124032

[223] G.M. McCracken, *et al., J. Nucl. Mater.* **93 – 94** (1980) 3

[224] R. Dux, *et al., J. Nucl. Mater.* **363 – 365** (2007) 112 – 6

[225] A. Thoma, *et al., Plasma Phys. Control. Fusion* **39** (1997) 1487 – 99

[226] A. Järvinen, *et al., Phys. Scr.* **T145** (2011) 014013

[227] A. Järvinen, *et al., J. Nucl. Mater.* **438** (2013) S1005 – S1009

[228] J. Neuhauser, *et al., Nucl. Fusion* **24** (1984) 39

[229] L. Spitzer, *Physics of Fully Ionized Gases* **2nd edition** (1962) New York: Wiley ISBN: 9780486151588

[230] D. Tskhakaya, *et al., J. Nucl. Mater.* **463** (2015) S624 – S628

[231] P. Mantica, *et al., Proceedings of the 42nd EPS Conference on Plasma physics*, Lisbon, Portugal 22 – 26 June 2015

[232] R. Dux, *et al., Nucl. Fusion* **51** (2011) 053002

[233] D. Reiser, D. Reiter, M.Z. Tokar, *Nucl. Fusion* **38** (1998) 2

[234] J.P. Gunn, *et al., J. Nucl. Mater.* **363 – 365** (2007) 484 – 490

[235] D. Tskhakaya, *et al., J. Nucl. Mater.* **438** (2013) S522 – S525

[236] J.D. Strachan, *et al., Proceedings of the 38th EPS Conference on Plasma physics*, Strasbourg, France 27 June – 1 July 2011

[237] M.N.A. Beurskens, *et al., Nucl. Fusion* **48** (2008) 095004

[238] M. Brix, *et al., Rev. Sci. Instrum.* **83** (2012) 10D533

[239] R.D. Monk, *et al., J. Nucl. Mater.* **241 – 243** (1997) 396

[240] P.D. Morgan, *et al., Rev. Sci. Instrum.* **56** (1985) 862

[241] B. A. Lomanowski, *et al., Rev. Sci. Instrum.* **85** (2014) 11E432

[242] A. Huber, *et al., Fusion Eng. Des.* **82** (2007) 1327

[243] T. Eich, *et al., J. Nucl. Mater.* **415** (2011) S856

[244] T.H. Osborne, *et al., Plasma Phys. Control. Fusion* **42** (2000) A175 – A184

[245] J. Stober, *et al., Plasma Phys. Control. Fusion* **42** (2000) A211 – A216

[246] C.F. Maggi, *et al., J. Nucl. Mater.* **241 – 243** (1997) 414

[247] A. Huber, *et al., Rev. Sci. Instrum.* **83** (2012) 10D511

[248] A. E. Jaervinen, *et al., J. Nucl. Mater.* **463** (2015) 135 – 142

[249] D. Moulton, *et al., J. Nucl. Mater.* **415** (2011) S500 – S512

[250] M.J. Leyland, *et al., Nucl. Fusion* **53** (2013) 083028

[251] M.J. Leyland, *et al., Nucl. Fusion* **55** (2015) 013019

[252] W. Eckstein, *Suppl. Nucl. Fusion* **1** (1991) 17

[253] E. M. Hollmann, *et al., Plasma Phys. Control. Fusion* **48** (2006) 1165 – 1180

[254] S. Brezinsek, *et al., Contrib. Plasma Phys.* **42** (2002) 6 – 7, 668 – 674

[255] G. Sergienko, *et al., J. Nucl. Mater.* **438** (2013) S1100 – S1103

[256] A. Järvinen, *et al., Proceedings of the 38th EPS Conference on Plasma Physics*, 27 June to 1 July 2011, Strasbourg, France

[257] M. Groth, *et al., J. Nucl. Mater.* (2011) **415** (2011) S530 – S534

[258] S. Wiesen, *et al. Plasma Phys. Control. Fusion* **53** (2011) 124039

[259] S. Brezinsek, *et al., J. Nucl. Mater.* **463** (2015) S11 – S21

[260] S. Wiesen, *et al., JINTRAC-JET modelling suite JET ITC-Report* (2008), http://www.eirene.de/JINTRAC_Report_2008.pdf

[261] K.D. Lawson, *et al., J. Nucl. Mater.* **463** (2015) S582 – S585

Nuclear fusion holds one of the biggest promises of a virtually unlimited energy source. As a result of half a century of dedicated research, reactor scale fusion devices are becoming reality within the following decades. A key challenge for these gigawatt scale devices is to achieve controlled power exhaust to avoid overheating of the wall components. The *radiative divertor* concept is developed to address this need.

This thesis presents experimental and numerical studies of radiative divertor operation in high confinement mode plasmas in the *Joint European Torus* (JET) test reactor. The impact of extrinsic impurity gases, such as nitrogen, on the reactor performance is investigated. The peak heat loads are reduced by an order of magnitude with extrinsic impurities. Furthermore, the simulations capture the measured heat load reduction and radiated power with impurity injection. However, the model underestimates the radiation by the fuel species.

ISBN 978-952-60-6475-8 (printed)
ISBN 978-952-60-6476-5 (pdf)
ISSN-L 1799-4934
ISSN 1799-4934 (printed)
ISSN 1799-4942 (pdf)

Aalto University
School of Science
Department of Applied Physics
www.aalto.fi

BUSINESS + ECONOMY

ART + DESIGN + ARCHITECTURE

SCIENCE + TECHNOLOGY

CROSSOVER

DOCTORAL DISSERTATIONS

Aalto-DD 156/2015